Technical Report

TR-09-15

Stress evolution and fault stability during the Weichselian glacial cycle

Björn Lund, Peter Schmidt, Christoph Hieronymus
Department of Earth Sciences
Uppsala University

January 2009

Svensk Kärnbränslehantering AB
Swedish Nuclear Fuel
and Waste Management Co

Box 250, SE-101 24 Stockholm
Phone +46 8 459 84 00

Stress evolution and fault stability during the Weichselian glacial cycle

Björn Lund, Peter Schmidt, Christoph Hieronymus
Department of Earth Sciences
Uppsala University

January 2009

Preface

This document contains information on the stress evolution and fault stability under glacial conditions, to be used in the safety assessment SR-Site.

Stockholm, October 2009

Jens-Ove Näslund

Person in charge of the SKB climate programme.

Summary

In this report we examine how the waxing and waning of an ice sheet during a glacial cycle affects the state of stress in the Earth, and how those changes in stress influence the stability of faults. We focus on the stresses at repository depth in Forsmark and Oskarshamn, and on the stability field at seismogenic depth at the proposed repository sites and at the Pärvie endglacial fault in northern Sweden. This study is a modelling study, where we use three-dimensional ice and earth models to calculate the glacial isostatic adjustment (GIA), i.e. the response of the Earth to an ice load, examining both displacements and stresses. We use a flat-earth finite element approach, based on /Wu 2004/ with some modifications. The result presented here is a continuation of previous studies in two dimensions /Lund 2005a, 2006b, Lund and Näslund 2009/ and complement those studies in assessing how the three-dimensionality of the problem affects the conclusions. We use the Fennoscandian ice model of /Näslund 2006/, which is a dynamic ice sheet model based on climate reconstructions with constraints from geological observations. The ice model spans the entire Weichselian glaciation but we only use the last 68 kyr, which includes the two major periods of ice cover as depicted in this ice sheet reconstruction. For the GIA calculation we use a number of different earth models, both with flat horizontal layers and with various 3D structures of lithosphere thickness. We do not include lateral variations in the viscosity of the mantle.

Comparing the current day rebound velocities predicted by our models with GPS observations from the Bifrost project /Lidberg et al. 2007/, we note that in general, we can obtain a reasonable fit to the observations with our models, and that the results are rather sensitive to the assumed viscosity of the mantle. We also find that the differences between data and model results, for all earth models, have common features which we interpret as due to the ice model. These observations are in agreement with numerous other GIA studies, e.g. /Milne et al. 2004, Whitehouse et al. 2006, Wang and Wu 2006/. Our flat layered models tend to fit the data better than the few models with laterally varying lithosphere thickness, where especially the horizontal velocities vary significantly between models and between the models and the data.

The regional patterns of stress distribution and stress directions are remarkably similar for all earth models, while the magnitude of the induced stresses vary significantly between models, mainly due to variations in the stiffness of the uppermost layer. The temporal stress evolution at 500 m depth in Forsmark and Oskarshamn is determined by the ice sheet evolution whereas the magnitude of the induced stresses depend on the earth model. For models with realistic stiffness distributions, the induced horizontal stresses both in Forsmark and in Oskarshamn are similar to the magnitude of the vertical stress of the ice load. Stress histories for the Pärvie fault, which is located close to the western edge of the ice sheet, show that although the Pärvie fault is the largest known endglacial fault, the induced stress magnitudes are not very high, which is due to the relatively modest thickness of the ice sheet here all through the glacial history.

In the fault stability analysis we use mainly two synthetic background stress fields, one reverse and one strike-slip. In agreement with previous studies /Wu et al. 1999, Lund 2005a, 2006b/ we find that the background stress field is very important for the resulting stability field. We show that in a reverse state of stress at 9.5 km depth, with a glacially induced pore pressure head of 50% of the local ice weight, both Forsmark and Oskarshamn would experience fault instability at the end of glaciation. In a strike-slip stress state, the stability field is more sensitive to variations in the direction of the background field, but for our reference field both Forsmark and Oskarshamn show mostly stable conditions. Stability analysis at the Pärvie fault shows that in a strike-slip background field the Pärvie fault would be stable all through the glaciation while in a reverse faulting background stress field our models show unstable conditions at the end of the glaciation, in general agreement with the observations /e.g. Lagerbäck, 1979/. The assumed background stress field, with the direction of maximum horizontal stress in the direction of local plate motion, also predicts a fault orientation in general agreement with the overall strike of the Pärvie fault.

Our simulations of fault stability show a very strong dependence of fault stability on the glacially induced excess pore pressure. Increasing the pressure head to 90% of the local ice weight will cause wide-spread instability during ice covered conditions in a strike-slip background field, while in a reverse field instability is promoted earlier in the glacial cycle. Our approach to estimating the induced pore pressure in this study has been one of very simple static conditions and high permeability, implying an immediate propagation of pressures at the base of the ice sheet to the studied depth. Pore pressure diffusion modelling or poroelastic simulations are probably necessary to correctly estimate induced stresses and pore pressures.

All of the above simulations were performed with the same ice history. The results for the overall pattern of the induced stresses, stress magnitudes and their duration through time, may be very different for a different ice history. However, since Forsmark and Oskarshamn are both located within the ice sheet margin, stress magnitudes are mostly determined by the thickness and duration of the ice sheet. The /Näslund 2006/ ice sheet is generally considered rather thick, as compared e.g. to the /Lambeck et al. 1998/ Fennoscandian ice sheet, but has shorter duration than the /Lambeck et al. 1998/ ice. This implies that maximum stress magnitudes may not be underestimated using the /Näslund 2006/ ice history relative to the /Lambeck et al. 1998/ ice history, although the temporal behaviour is difficult to assess without modelling.

Contents

1 Introduction

A nuclear waste repository constructed at high latitudes, such as in Fennoscandia, northern Russia or Canada, will eventually be subject to a glaciation /e.g. SKB 2006b/. The ice sheet will increase the mechanical load on the repository, both through the additional weight of the ice itself and through the flexural response of the Earth's lithosphere. The flexure is important as it will induce horizontal stresses of the same magnitude as the vertical stress due to the weight of the ice. In addition to the increased stresses, the ice sheet will increase the water pressure in the rock below the ice. The increased pore pressure, in combination with the increased stresses, may cause the rock to fail, thereby causing disturbances ranging from increased fracture permeability to large earthquakes, such as the endglacial faults of northern Sweden /e.g. Lagerbäck 1979/.

In order to analyse how a glaciation affects the stresses in the solid Earth it is necessary to model the Earth's response to the ice load, the so called glacial isostatic adjustment (GIA). GIA models incorporate an ice model for the temporal and spatial evolution of the ice sheet and an earth model which subsides or rebounds as the ice load varies. Since the observables in glacial rebound are mostly related to displacements of the Earth's surface, usually in the form of relative sea-level measurements such as lake isolation events, raised beaches or tide-gauge data but today increasingly in the form of GPS-measurements, most GIA modelling results are presented as displacements. Stresses are occasionally presented, mostly in studies of glacially induced faulting, e.g. /Wu and Hasegawa 1996a, Johnston et al. 1998, Klemann and Wolf 1998, 1999, Wu et al. 1999, Ivins et al. 2003/.

The processes underlying the stress conditions necessary to create the large endglacial faults of northern Fennoscandia have been studied by a large number of authors. As this report considers the response of quantitative GIA models, the following review will concentrate on studies of faulting based on crustal stresses from such models. Early investigations /Walcott 1970, Stein et al. 1979/ found that postglacial rebound stresses alone could be responsible for the mode of earthquake failure in eastern Canada. /Quinlan 1984/ pointed out that the rebound stress probably rather acts a triggering mechanism for faults close to failure in the ambient tectonic stress field. The models used in these studies were elastic plates on fluid mantles, neglecting the effect of stress relaxation in a viscoelastic medium. /Johnston 1987, 1989/ showed that earthquakes are suppressed by large ice sheets and discussed strain accumulation under the ice sheets but did not consider rebound stresses. /James and Bent 1994/ calculated rebound strain rates in a viscoelastic model and found that they were greater than current seismic strain rates in Canada, implying that rebound alone could cause the earthquakes. During the last decade, P. Wu and collaborators have presented a number of studies on fault stability during glaciation and deglaciation, both basic, generic models /Wu and Hasegawa 1996a, Johnston et al. 1998/ as well as applied to Canada /Wu and Hasegawa 1996b, Wu 1997, Wu and Johnston 2000/ and Fennoscandia /Johnston et al. 1998, Wu et al. 1999/. These are all viscoelastic models with an elastic lithosphere which use the difference in Fault Stability Margin (dFSM, essentially a Coulomb failure stress /Quinlan 1984/) to infer increased or decreased fault stability. dFSM was also used by /Klemann and Wolf 1999/ as a parameter in their study of the implications of a ductile layer in the crust for the deformation caused by the Fennoscandian ice sheet. These studies generally find that earthquake activity is suppressed by the emplacement of the ice sheet but greatly enhanced at the end of deglaciation. The onset and location of increased fault instability, however, varies with ice sheet dimension and temporal evolution, lithospheric and mantle structure and the initial state of stress. Recently, /Hetzel and Hampel 2005, Turpeinen et al. 2008/ incorporated faults in their finite elements models in order to study how glaciation affects slip rates on faults. They conclude, in general agreement with the studies above, that slip on faults is decreased during glacial advance but enhanced during deglaciation. The influence of deglaciation on seismicity is of importance also today, as glacier retreat is widespread due to the current global warming trend. /Sauber et al. 2000, Sauber and Molina 2004/ showed how current retreat of Alaskan glaciers affects strain localisation and earthquake activity.

In this report we attempt to understand how the stresses induced by a recent model reconstruction of the latest Fennoscandian (Weichselian) ice sheet evolve in time and space, and how those stresses interact with, and affect, the regional state of stress in Fennoscandia. This study is a continuation of the investigations reported previously in /Lund 2005a, b, 2006a, b, Lund and Näslund 2009/ and the main focus of the current report is on the effects of high resolution, three-dimensional modelling. We use the three-dimensional Weichselian ice sheet of /Näslund 2006/, which is the reference ice sheet evolution for the Swedish Nuclear Fuel and Waste Management Co. (SKB), in combination with both simple, horizontally layered Earth models and more complex 3D representations of the Earth. The resulting displacement fields are compared to available GPS data and we present maps and vertical cross-sections of the evolution of glacially induced stress in the models. In order to investigate the interaction of the glacial stresses with the background stress field we construct models of the background field and show how the combined stress field evolves. Using the combined stress field we estimate how the stability of faults is affected by the glaciation, presenting maps and vertical cross-sections of the stability field. We limit the analysis to glacially induced and tectonic stresses, not including stress accumulation during the glaciation as suggested by /Johnston 1987/ and /Adams 2005/. In particular, we zoom in on the proposed nuclear waste repository sites of Forsmark and Oskarshamn and for comparison show a similar analysis for the Pärvie fault in northern Sweden, the largest of the endglacial faults.

This project aims to provide stress information as boundary conditions for nuclear waste repository models at different scales, which is why we present the stress evolution at Forsmark and Oskarshamn at repository depth (500 m). We also assess fault stability at the proposed repository sites, which is performed at seismogenic depths (9.5 km).

2 Modelling glacial isostatic adjustment

Techniques and methods for the modelling of glacial isostatic adjustment (GIA) have developed rapidly during the last decade. Traditionally based on spectral decomposition in relaxation modes e.g. /Peltier 1974, Wu and Peltier 1982, Wolf 1991/, the current move to incorporate lateral variations in the Earth's composition, its spherical shape and gravitation has lead to the adoption of various finite element techniques e.g. /Martinec 2000, Wu and van der Wal 2003, Wu 2004, Latychev et al. 2005/. Other efforts have been directed to incorporating the effects of changing sea-levels and the rotation of the Earth e.g. /Johnston 1993, Milne and Mitrovica 1998, Mitrovica et al. 2001/ and investigations into the effects of compressibility on GIA predictions e.g. /Han and Wahr 1995, Klemann et al. 2003/. A recent review of many aspects of GIA modelling can be found in /Whitehouse 2009/. In this report we use a finite element (FE) methodology based on /Wu 1992, 2004/ which allows for the modelling of GIA using commercial finite element packages; we use Abaqus /Abaqus 2007/.

The momentum equation for quasi-static, infinitesimal perturbations of a stratified, compressible, fluid Earth initially in hydrostatic equilibrium subject to gravitational forces is typically written /e.g. Wolf 1991, Wu 2004/.

$$\nabla\cdot\boldsymbol{\sigma}-\nabla(\boldsymbol{u}\cdot\rho_0 g_0\hat{\boldsymbol{r}})-\rho_1 g_0\hat{\boldsymbol{r}}-\rho_0\nabla\phi_1 = 0 \qquad (2\text{-}1)$$

Here $\boldsymbol{\sigma}$ is the stress tensor, $\mathbf{u}$ is the displacement vector, $\hat{\boldsymbol{r}}$ a unit vector in the radial direction and ρ, g, ϕ are the density, gravitational acceleration and gravitational potential, respectively. The subscript 0 refers to the initial background state and the subscript 1 to the perturbed state. The first term is the divergence of stress and the second term is the so called pre-stress advection term, which describes how the initial background stress field is carried by the material in motion /Wu and Peltier 1982, Wolf 1991, Wu 2004/. The third term is usually referred to as the internal buoyancy term, as it accounts for the density change due to compression or dilation of the material. The fourth term is self-gravitation, accounting for changes in the gravitational potential due to mass redistribution. In our flat-earth models we will not take self-gravitation into account, as /Amelung and Wolf 1994/ showed that the two approximations of ignoring both self-gravitation and the sphericity of the Earth, i.e. using a flat-earth model, largely compensate each other. In addition, we will not consider the change in density due to compression of the material, i.e. ignoring the internal buoyancy term, but we will allow so called material compressibility. This is a mathematical construct, as material compressibility and buoyancy cannot be physically separated, but it allows for the inclusion of compressibility in the FE models /Klemann et al. 2003, Wu 2004/. Equation (2-1) therefore simplifies to:

$$\nabla\cdot\boldsymbol{\sigma}-\nabla(\boldsymbol{u}\cdot\rho_0 g_0\hat{\boldsymbol{r}}) = 0 \qquad (2\text{-}2)$$

Our methodology was reviewed in /Lund 2005a/ where benchmarks of the modelling scheme were presented. /Bängtsson and Lund 2008/ show how the Abaqus implementation of material compressibility in an elastic material with Poisson's ratio 0.2 underestimate the vertical displacements by approximately 10% below the centre of the ice sheet and how the solution converges to the expected results for more incompressible material. This is due to the implementation of pre-stress advection essentially as a surface load boundary condition, not accounting for volumetric effects. Recently, /Schotman et al. 2008/ compared the /Wu 2004/ flat-earth FE technique to a spectral model with an incompressible, viscoelastic spherical self-gravitating earth. The authors study a number of different details in the FE model and conclude that the two techniques agree very well for vertical displacements and geoid heights. The horizontal velocity field is less accurately modelled by the FE technique, as was also indicated in /Lund 2005a/. The modelling approach used in this study has also been applied in a study of glacially induced faulting in Fennoscandia /Lund and Zoback 2007, Lund and Näslund 2009/ and in studies of current deglaciation in Iceland /Pagli et al. 2007, Árnadóttir et al. 2009/.

The modelling of fault stability in this report will proceed according to:

1. An ice model is defined in terms of ice thickness and areal extent at specific times throughout an entire glaciation.
2. An earth model is defined in terms of material definitions (elastic parameters and rheology) and the lateral and depth extent of the materials. This is the finite element model, which we implement in Abaqus.
3. Using Abaqus, the ice load is applied to the earth model surface in time steps defined by the ice model. Displacements, strains and stresses are calculated by Abaqus at each time step.
4. The displacements are used both for relative sea-level curves and to calculate vertical and horizontal velocities of the Earth's surface.
5. A synthetic, regional background stress model is defined for use with the glacially induced stresses calculated by Abaqus.
6. Fault stability is calculated from the combined background and glacial stresses using a Mohr-Coulomb failure criterion.

2.1 Further development of the implementation of GIA in Abaqus

In his description of how to implement pre-stress advection into commercial finite element software, /Wu 2004/ advocates the use of Winkler foundations at all density contrasts. This is also the approach used in /Lund 2005a, 2006a, b/. However, when adding lateral variations in material composition into the finite element models we find that the Abaqus foundations implementation (key word FOUNDATION) may not be appropriate for elements at material interfaces which are not perpendicular to the direction of gravity, since the foundations always act perpendicular to the element face. In our models the direction of gravity is the vertical direction as the models do not include self-gravitation, i.e. gravity does not change as the material compresses or dilates. The purpose of Winkler foundations is to replace a distributed body force (gravity) with an equivalent concentrated force that is applied at the density interface. Only body forces relative to the hydrostatic background state need to be considered. If the interface between Layer 1 and Layer 2, with respective densities ρ_1 and ρ_2, is displaced by a vertical deflection w (Figure 2-1), then the total body force acting on a column of material of horizontal cross-section A is given by:

$$F_b = -Awg(\rho_2-\rho_1) \tag{2-3}$$

This force acts in the direction of the gravity vector, which in our model always points exactly downward. Ideally, the gravity force should be distributed over a number of elements in the vertical (Figure 2-1 b). In order to replace the body forces with equivalent surface forces at the interface,we have to use a force of the same magnitude as F_b above. However, it is clear from Figure 2-1 that the gravity force is not perpendicular to the density interface if the layer is inclined at an angle θ. The resulting normal and tangential components of the forces acting on the surface are:

$$F_n = -Awg(\rho_2-\rho_1)\cos\theta \tag{2-4}$$

and

$$F_t = -Awg(\rho_2-\rho_1)\sin\theta \tag{2-5}$$

These two force components are applied at the interface. The forces should be distributed equally over area A, but in a finite element code they are concentrated at the element nodes. The use of vertical springs ensures that the equivalent surface force of the gravitational body force is applied at the same angle relative to the interface as the gravity force itself.

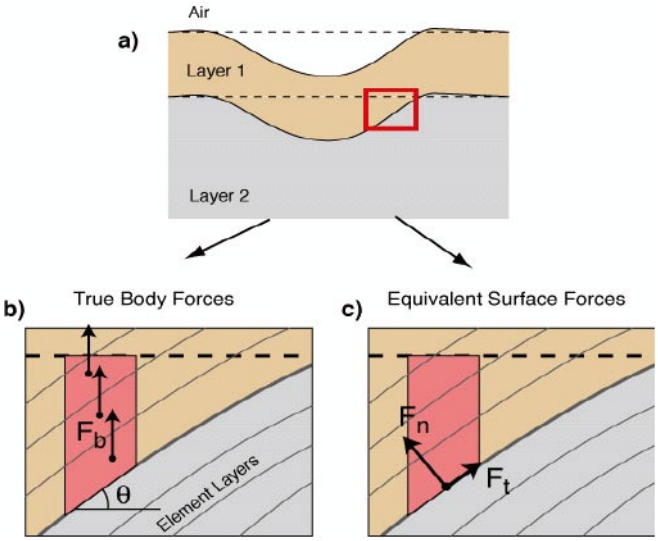

Figure 2-1. *Body forces and equivalent surface forces. a) Layer 1 is displaced vertically out of its hydrostatic equilibrium configuration indicated by dashed lines. b) The gravitational body force acts at every point in the continuum where material of a given density has been displaced by material of another density. In a finite element discretization, the body force acts at the centre of the corresponding elements. For a sloping density interface, the gravitational force has a component that is tangential to the surface. c) The effect of the body force is replaced by a surface force of equal magnitude and direction. Part of the surface force therefore acts parallel to the surface.*

Two points are worth noting:

1) The use of the equivalent surface force is obviously a simplification that is used in order to allow the solution of the equations by a numerical code such as Abaqus. Physically, it is equivalent to concentrating the volumetric buoyancy due to the interface deflection into an infinitesimally thin layer at the boundary. This physical construct implies that stress continuity no longer is satisfied at the boundary, but that there is a stress jump at the interface given by $\Delta\sigma_n = F_n/A$ for the normal component and $\Delta\sigma_t = F_t/A$ for the tangential component.
2) It was noted previously by /Bängtsson and Lund 2008/ that replacing a body force with a concentrated normal surface force introduces an error if the material is compressible. A similar error is introduced when the tangential component of the body force is replaced with a tangential surface force. Both of these errors are small as long as the vertical displacement of the density interface is small (formally, the requirement is that the induced elastic displacements are small relative to the total displacement, which implies $wg\,(\rho_2-\rho_1)\cos\theta \ll K$ (where K is the bulk modulus) and $wg\,(\rho_2-\rho_1)\sin\theta \ll G$ (where G is the shear modulus).

Instead of Winkler foundations, we therefore implemented spring elements (SPRING1 in Abaqus) which always act in the vertical (gravity) direction no matter how the surface of the element is inclined. These spring elements are attached to the top nodes of the element. We apply the same spring constants as those suggested by /Wu 2004/, i.e. the density contrast at the interface times the gravitational acceleration, $(\rho_- - \rho_+)g$. In order to test the springs vs. foundation approaches we set up a two-dimensional GIA model scenario, see Figure 2-2.

The model has an elastic upper layer with Young's modulus 10 GPa, density 2,800 kg/m^3 and Poisson's ratio 0.3. The half-space below has Young's modulus 100 GPa, density 3,300 kg/m^3 and viscosity 10^{21} Pa s. We also ran a reference model with a flat material interface at 90 km depth. The inclined material boundary can be implemented either as steps, using similar sized elements with horizontal faces, or using elements with inclined element faces, see Figure 2-2. The ice load is a box car which was ramped up linearly from zero to 28 MPa over 10 kyr and then held constant for 50 kyr. In Figure 2-3 we show the difference in vertical and horizontal displacements for the two different boundary condition approaches, using the reference model and models with the inclined material interface implemented using steps or inclined elements. For the reference model there is no difference between using springs or

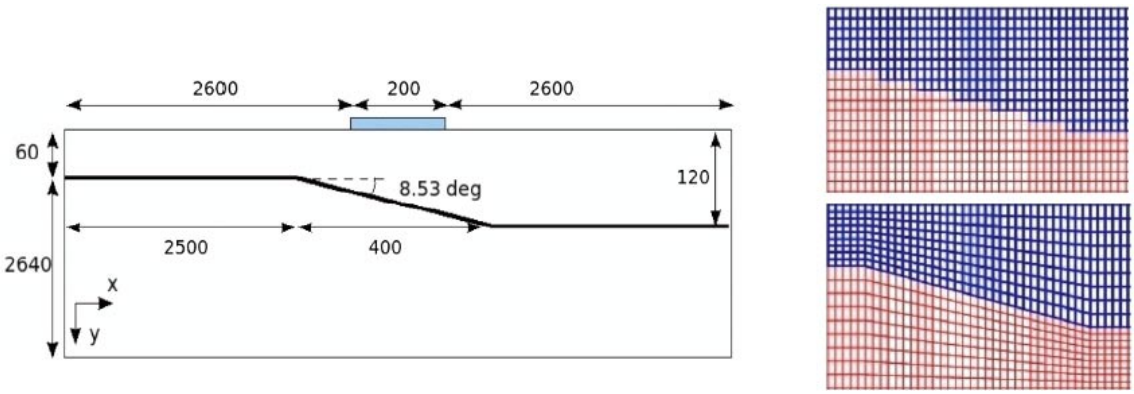

Figure 2-2. *Left: Geometry of the 2D model used to test spring vs. foundations as implementations of pre-stress advection in the finite element models. The blue box on the top surface is the ice load, numbers indicate distances in km. Right: Implementing the inclined boundary as steps (above) or smooth, inclined elements (below).*

Winkler foundations, showing that the two approaches are equivalent (the red dots visible in the two first rows for the difference in vertical displacements are due to numerical noise close to the cut-off 0.1). If the inclined material interface is implemented with steps, as in Figure 2-2, the middle panel of Figure 2-3 shows that there is very little difference between the spring and the foundation approaches, as expected. However, a stepping interface invariably introduces stress concentrations at the corners, which makes this mesh less attractive. A sloping interface implemented using elements with sloping faces is obviously the natural finite element choice.

For such models we see in the lowermost left plot in Figure 2-3 that there is an appreciable difference in the horizontal displacements between the model using springs and the model using foundations. In fact, the differences in the horizontal displacements are in places more than 50% of the absolute horizontal displacements, notably in the region of the material interface and at the surface below the ice load. The differences in the vertical displacements are much smaller and insignificant in relation to the absolute vertical displacements. Notwithstanding, the large differences in horizontal displacements do produce significant differences in the induced stress field. We interpret these results as the foundations pushing the material to the right, down slope, in Figure 2-3, due to the fact that the foundations act perpendicular to the sloping element faces. As we consider the behaviour of the foundations erroneous, our models in this study will use springs as boundary conditions for the implementation of the pre-stress advection.

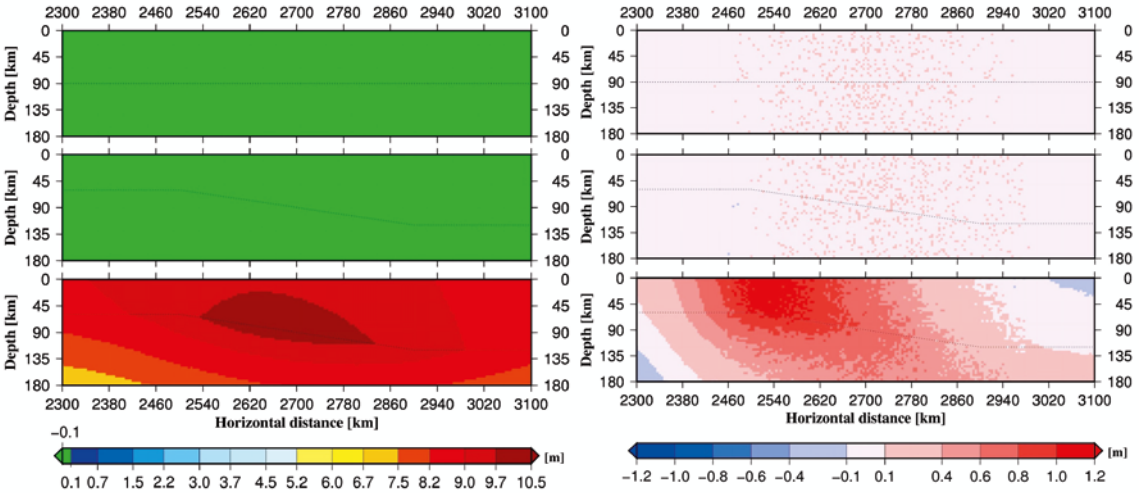

Figure 2-3. *Difference in displacement when pre-stress advection is modelled either by springs or by foundations at material interfaces. Left column: horizontal displacement differences; right column: vertical displacement differences. The upper row shows results from the reference model with a flat layer at 90 km depth. The middle row shows the results from an inclined boundary implemented using steps as in Figure 2-2. The lower row shows results from an inclined boundary using elements with an inclined face, Figure 2-2.*

2.2 Benchmarks

The benchmarks presented by /Wu 1992, 2004, Lund 2005a/ show that the Abaqus GIA implementation works well within its defined physical boundaries, i.e. GIA models using earth models that are flat and incompressible. /Bängtsson and Lund 2008/ agreed that for an elastic half-space model which is incompressible, the Abaqus implementation is correct but that the inclusion of material compressibility, as discussed above, did not agree perfectly with a finite element implementation of the correct pre-stress advection term. Deviations were on the order of 10% at maximum vertical displacements. Below we further investigate the applicability of the Abaqus GIA implementation in comparisons to spectral GIA models by V. Klemann, GFZ-Potsdam, and also ensure that our 3D models behave as expected.

2.2.1 Axisymmetric model benchmarks with Klemann's spectral code

A benchmark suite of models are being analysed in order to compare the results of our FE implementation with those of V. Klemann's axisymmetric, flat-earth spectral code. Due to time constraints this comparison could not be completed in time for this report but will be reported in a scientific paper which is under preparation. Preliminary results are available for a model with a 100 km elastic layer overlying a viscoelastic half-space using a 350 km radius rectangular cross-section ice sheet with 1.5 km height. We compare both an incompressible model (IK in the terminology of /Klemann et al. 2003/) and a model with material compressibility but without the buoyancy term (C1 of /Klemann et al. 2003/). Preliminary results indicate that horizontal and vertical displacements and stresses for the IK model agree very well between the two modelling techniques. For the C1 model, the vertical displacements still agree just as well, which also agrees with numerous other studies on the effects of material compressibility, e.g. /Schotman et al. 2008/. The horizontal displacements, however, deviate 10%–15% at the maximum horizontal displacements. This is in agreement with /Bängtsson and Lund 2008/ and may also be the cause of the misfit in the horizontal velocities observed by /Schotman et al. 2008/. More in-depth analysis is under way, as is a comparison between the compressible FE model and the fully compressible, including buoyancy, C2 model of /Klemann et al. 2003/.

2.2.2 Benchmarking our 3D implementation

In order to ensure that our 3D finite element model implementation is correct, and to study how the relatively coarse mesh of the 3D model respond, we performed benchmark tests against the 2D analytical viscoelastic half-space model of /Wu 1992/ and the elastic layer over viscoelastic half-space axisymmetric model of /Klemann and Wolf 1998, Lund 2005a/. Our earth models used here all utilize the 3D mesh described in detail below. This mesh has an interior box of 4,110×2,800 km, designed to fit the Weichselian ice model described below, which is not ideal in order to simulate a wide 2D ice sheet in 3D. We have therefore modified the benchmarks slightly.

Wu 1992

The viscoelastic half-space benchmark model used by /Wu 1992/ had a 2D ice model, shaped as a boxcar, with half-width 1,000 km. Since our 3D interior mesh is only 4,110 km long, we decided to use a model ice sheet of only 500 km width instead of the full 2,000 km. With a 4,110×500 km long ice we have an aspect ratio of approximately 1:8, which makes for a decent 2D approximation across the centre of the ice. Using Equations A1 and A2 in Appendix A of /Wu 1992/ we can calculate the theoretical vertical displacements for the 500 km ice load on the viscoelastic half-space (Young's modulus 113 GPa, Poisson's ratio 0.5, density 5,000 kg/m3 and viscosity 1.45×10^{21} Pa s). We evaluate the displacements after 1,840, 5,510 and 18,400 yr, as in /Wu 1992/. Figure 2-4 shows the result of the 3D Abaqus model and we see that the vertical displacements agree well with the theoretical results, even though the element size of the mesh is 50×50 km so that the ice only covers 10 elements in cross-section. The largest misfits are observed in the steeply sloping sections, which is expected since the load edge is very steep and the elements cannot capture the gradients properly due to their size. The horizontal displacements are very small which agrees well with theory, since in an incompressible viscoelastic half-space there should be no horizontal displacements at the surface /O'Keefe and Wu 2002/.

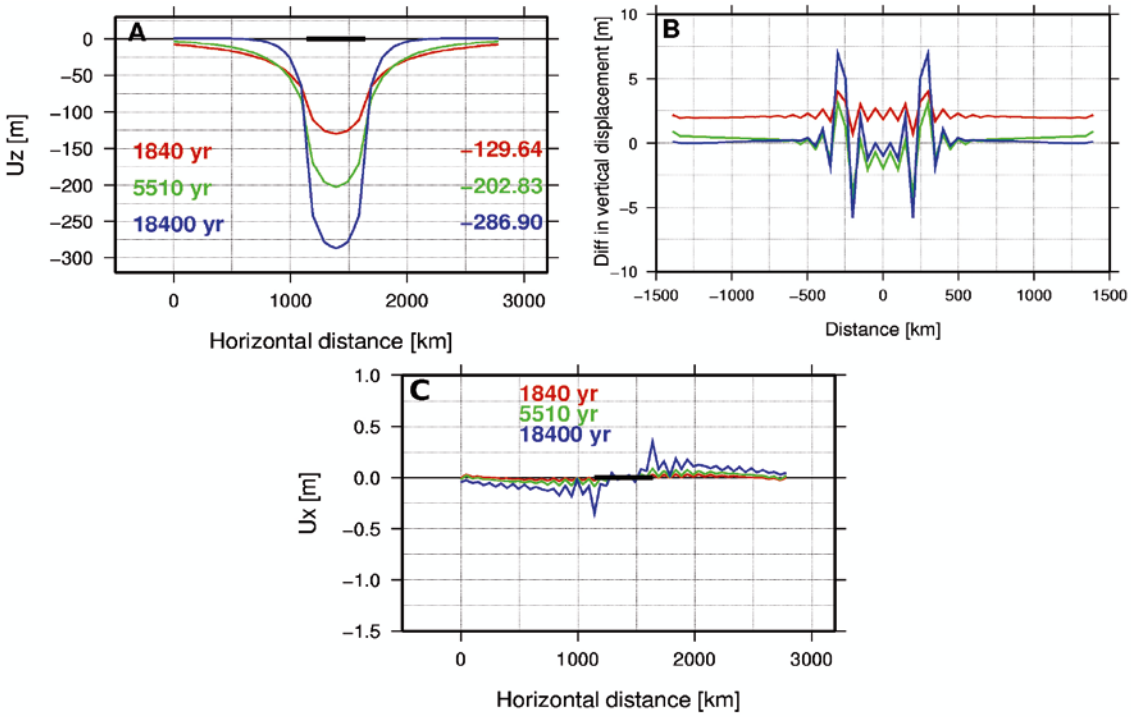

Figure 2-4. *Benchmark using a model similar to /Wu 1992/ with a 500 km wide boxcar ice load, indicated by a thick black line in (A) and (C), loading a viscoelastic half-space. (A) Vertical displacements at 1,840 (red), 5,510 (green) and 18,400 (blue) yr from the 3D Abaqus model. Maximum theoretical displacements are annotated in the figure. (B) Difference between the Abaqus results and theory, same colour code as in (A). (C) Horizontal displacements from the Abaqus model.*

Klemann and Wolf 1998, Lund 2005a

/Lund 2005a/ presented a benchmark study using the axisymmetric model of /Klemann and Wolf 1998/, similar to the models presented in Section 2.2.1 above. He then used a 2D version of the /Klemann and Wolf 1998/ model as a reference for the remainder of the report. Here we present a benchmark of our 3D model to the 2D model of /Lund 2005a/. As above, the 2D ice model is difficult to simulate on our limited interior box in the 3D model. We constructed a 3D ice model with elliptical cross-section, 25 MPa load at the centre and 900 km half-width, in agreement with the 2D ice model in /Lund 2005a/, stretching along the full 4,110 km length of the 3D interior mesh. This, however, produces an ice with aspect ratio of only 1:2.3, which does not produce a very good 2D approximation across the centre of the ice. The ice is ramped up during 90 kyr (to the "last glacial maximum"), then immediately ramped down during 10 kyr (to the "end of glaciation") and then there is no ice for 8 kyr (to the "present time"). The earth model has a 100 km elastic layer (Young's modulus 192 GPa, Poisson's ratio 0.5, density 3,380 kg/m3) overlying a viscoelastic halfspace (Young's modulus 435 GPa, Poisson's ratio 0.5, density 3,380 kg/m3, viscosity 10^{21} Pa s).

We see in Figure 2-5 that in spite of the expected relatively poor 2D approximation in a cross-section through the ice, the results of the 2D and 3D Abaqus models agree well, both in the shape of the stress contours and the magnitudes. Having compared both displacements, above, and stresses in our 3D model we conclude that although the element size in the high resolution part of our 3D model is relatively coarse (50×50×5 km in X, Y and depth) compared to the much higher resolution 2D models of /Lund 2005a, 2006b/, the 3D model performs very well.

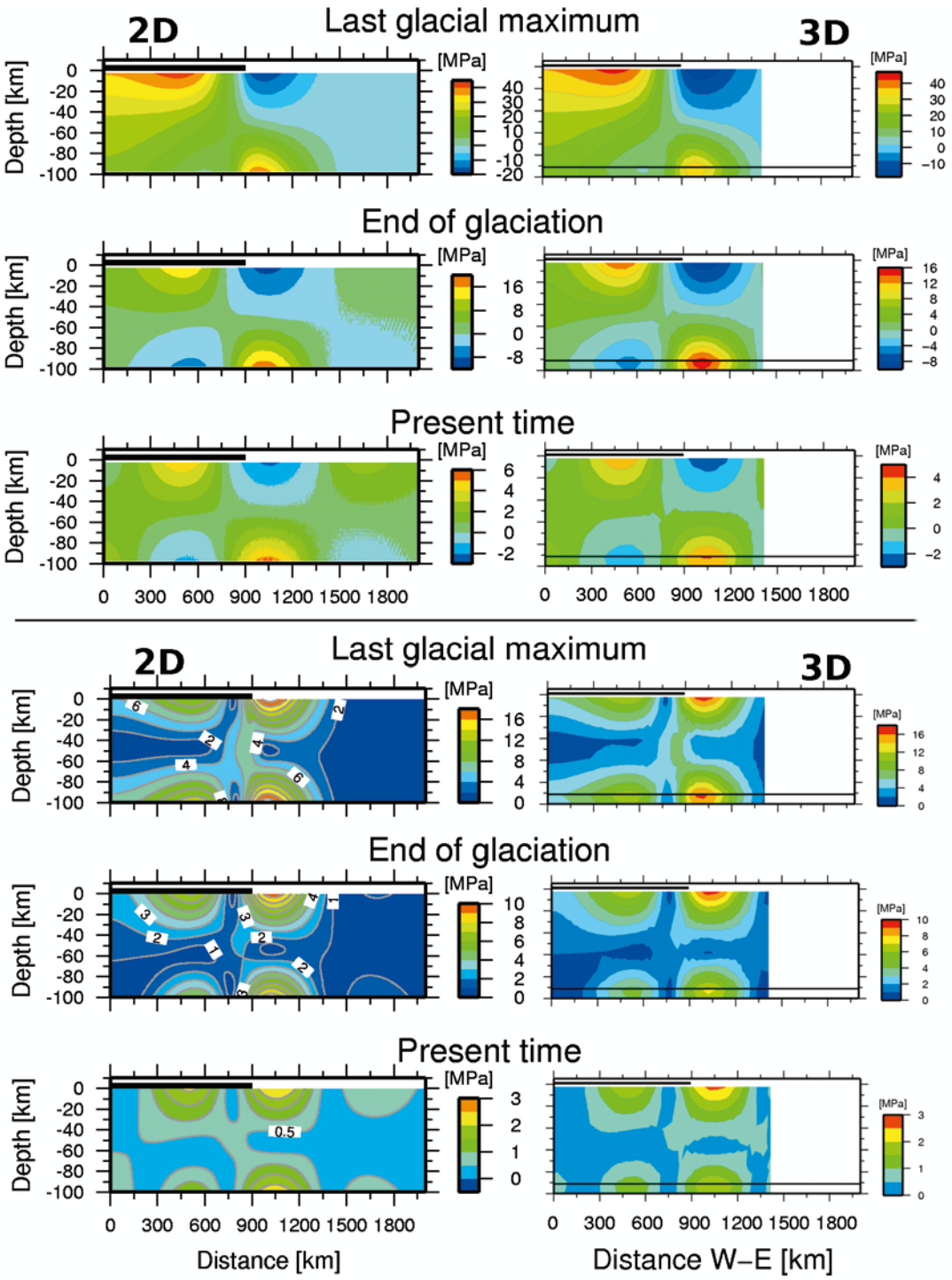

Figure 2-5. *Comparison of the magnitude of the maximum horizontal stress (upper three rows) and the maximum shear stress (lower three rows) in 2D and 3D models based on /Klemann and Wolf 1998, Lund 2005a/. The left column shows the 2D results and the right column the 3D results. Results are only shown from the high resolution inner box in 3D. The line at 91 km depth in the 3D figures indicates the last row of element centroids in the layer.*

2.3 GIA effects not included in our models

The field of GIA modelling is currently growing very rapidly, with new techniques being developed that take more and more of the GIA related effects into account. Currently there is no single technique that can model all the known theoretical GIA aspects together with fully 3D earth models. The finite element technique we use is especially well suited for complicated earth models, but there are GIA related effects which we do not model that are known to influence the resulting earth response. The reason for not including these effects are partly due to the available modelling tools (most of the recently developed tools have not been publicly released) and partly due to constraints in terms of resources. The omissions can be loosely subdivided into two classes; 1) load related effects and 2) model implementation effects. We estimate that the non-modelled effects do not significantly influence the results of this report.

2.3.1 Load related effects

Perhaps the most severe omission in our models is the lack of a sea-level equation. /Milne et al. 2004/ indicate that the redistribution of water during glaciation, the local ocean load, adds approximately 10% of the total signal to the current rebound velocity field. In our models we simply produce the ice from vapour, and vaporize the ice at deglaciation, we do not model any water. /Schotman et al. 2008/ use the eustatic ocean-load output from their spectral model as an additional load in their FE-model. They conclude that the error in predicted geoid heights by using the eustatic ocean-load instead of a "realistic" self-gravitating sea-level function is small compared to the absolute geoid heights. In future work such a eustatic ocean-load should be included in our models.

Our GIA model is a regional model for northern Europe and as such does not include the effects of the other large ice sheets of the last glacial cycle, most importantly the Laurentide ice sheet. /Mitrovica et al. 1994, Wang and Wu 2006/ showed that the Laurentide ice sheet produced significant displacements also on the Fennoscandian crust, and that part of the current horizontal displacement field may still be affected /Whitehouse et al. 2006/. However, /Klemann et al. 2008/ show that if plate boundaries are approximated as low viscosity zones, these produce discontinuities in the horizontal displacement field which may decrease the influence of e.g. the Laurentide ice sheet on Fennoscandia.

Most, if not all, current ice models are constructed in close interaction with a particular earth model. If the parameters of the earth model is changed then the shape and temporal evolution of the ice may also change e.g. /Lambeck et al. 1998, Peltier 2004/. None of the earth models we run below is a replica of the model that was used to produce the ice sheet we utilize and in that respect we do not have consistency between ice and earth models. We have not tried to quantify the effect of this coupling between ice and earth model but for reasonable choices of earth models the effect is considered relatively small (Näslund 2009, private communication).

In our models we have not included residual effects of previous glaciations, which depend on the mean viscosity of the Earth. For viscosities of the order of 10^{21} Pa s the effect is small but this may not be true for viscosities of 10^{22} Pa s or higher /e.g. Wu and Peltier 1982/. It is estimated that today, some 10 kyr after deglaciation, there is still approximately 50 m of rebound remaining in central Fennoscandia /Ekman 1991/. The residual stresses are inferred to be small /Wu et al. 1999, Lund, 2006b/ and even if the current inter-glacial ends relatively shortly it is likely that the coming ice sheet takes tens of thousands of years to grow to significant thickness, if it follows the patterns of the Weichselian glaciation. In an assessment of sea-level change and shore-line migration in Sweden /Whitehouse 2006/ models two consecutive glaciations to study the effect of multiple glaciations. She concludes that the difference in sea-level predictions between one and two glacial cycles is negligible. In this study we will also neglect any effects of previous glaciations.

2.3.2 Model implementation effects

As discussed above our Abaqus implementation of the GIA momentum equation suffers from some drawbacks. We do not correctly model material compressibility and we do not at all include the effect of internal buoyancy. We intend to quantify these simplifications in the benchmarks with V. Klemann. For the time being we refer to Figure 4 of /Wu et al. 1999/ where it is shown that the difference in Fault Stability Margin (FSM) between a compressible and incompressible spherical model is small, and to /Schotman et al. 2008/ who showed that the differences between the flat-earth FE model and a spherical spectral model are small.

In addition, our models are not self-gravitating, but as showed by /Amelung and Wolf 1994/ the effect of this approximation is partly counteracted by the flat-earth approximation, which is confirmed by /Schotman et al. 2008/.

In our modelling approach we add tectonic (deviatoric) stresses to the output from the Abaqus modelling. A non-hydrostatic initial stress state will, however, affect the GIA momentum equation and the response to loading. To our knowledge (V. Klemann, personal communication, 2009) this has not been discussed in the literature so the effect of this simplification is unknown.

Finally our models are inertial models, so do not take into account the effect of the Earth's rotation. This is, however, a second order effect /Milne et al. 2004/.

3 Relationship between 2D and 3D models

Previous reports in this series /Lund 2005a, 2006a, b/ used 2D or axisymmetric ice models to model the stress field induced by a glaciation. Specifically, /Lund 2006b/ used 2D profiles through the 3D ice model of /Näslund 2006/. We will shortly return to the /Näslund 2006/ model, now using the full 3D formulation, but in this section we first illustrate how models using such 2D profiles compare to the full 3D results. We perform the comparisons in order to be able to judge the validity of the results of these previous reports, so that e.g. the effects of earth model variations can be used also for 3D models. For the purpose of illustration we use a simple ellipsoidal ice sheet, with a 2,450 km long axis in the north-south direction and a 1,450 km short axis in the east-west direction, see the black outline in Figure 3-1. The ice exerts a maximum pressure of 22.5 MPa at it's centre, corresponding to 2.5 km of ice. The dimensions of the ice sheet have been chosen to reasonably resemble those of the Fennoscandian ice sheet. We will extract a 2D model using a north-south ice profile offset 150 km west of the centre of the ice sheet, see Figure 3-1, simulating the 2D profile of /Lund 2006b/. The ice along the profile is 2,450 km long (corresponding to 49 elements of 50 km length) and has a maximum pressure of 22.05 MPa. It is rampedup linearly during 10 kyr, then stays in place for 40 kyr. Deglaciation occurs linearly over 10 kyr and the model is continued an additional 8 kyr for a total of 68 kyr model time. The earth model used has 50×50×5 km elements at the surface of the interior box, and a 100 km compressible elastic layer (Young's modulus 192 GPa, Poisson's ratio 0.5, density 3,380 kg/m3, Poisson's ratio 0.25) overlying an incompressible viscoelastic half-space (Young's modulus 435 GPa, Poisson's ratio 0.5, density 3,380 kg/m3, viscosity 10^{21} Pa s).

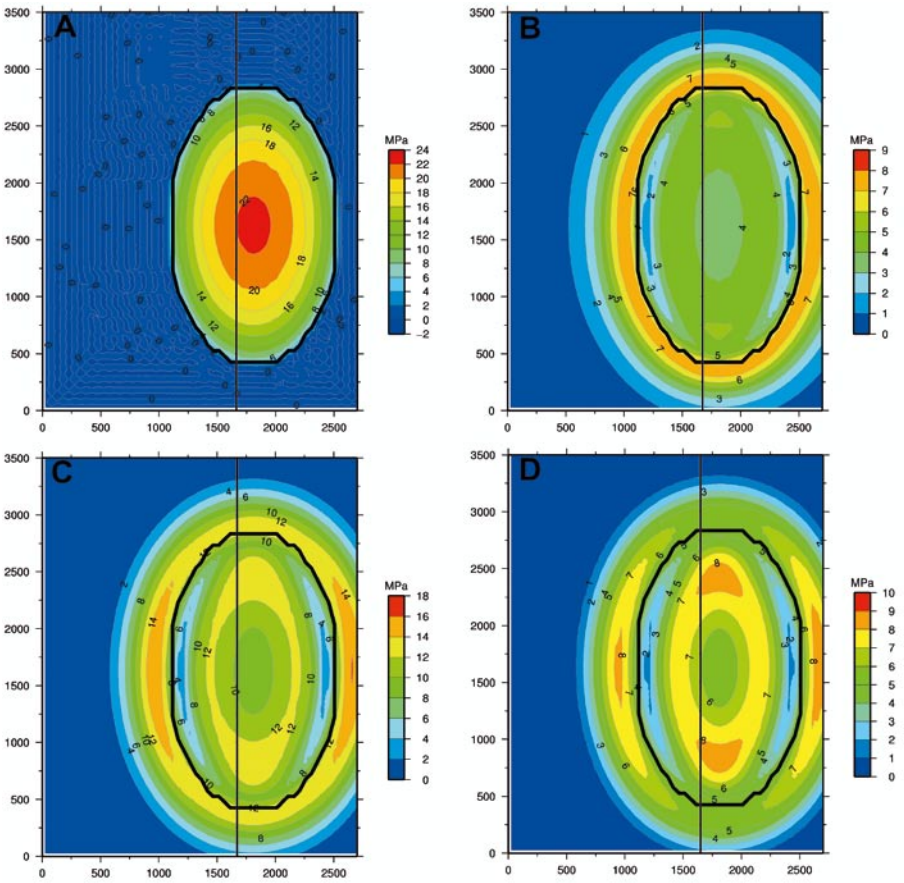

Figure 3-1. *Modelling an ellipsoidal ice sheet (black line). The vertical line indicate the position of the 2D profile. (A) The vertical stress at 2.5 km depth and 10 kyr after the onset of glaciation. (B), (C) and (D) show the maximum shear stress at 2.5 km depth. (B) 10 kyr (C) 50 kyr (D) 60 kyr.*

In Figure 3-1 we show the vertical stress at 2.5 km depth after loading the ice and snapshots of the maximum shear stress at 2.5 km depth and 10 kyr, 50 kyr and 60 kyr. Comparing with Figure 3-1A, where the vertical stress outlines the size of the ice sheet, we see in Figure 3-1 B-D that the highest shear stress develops around the rim of the depression bowl and later in the interior of the depression. We also note that shear stresses are higher and more varied along the short axis of the ellipsoid than along the long axis. As the lithosphere flexes under the weight of the load we see how shear stresses increase.

In Figure 3-2 the magnitude and direction of the maximum horizontal stress, S_H, is shown. Again we note how stress magnitudes increase under the load from 10 kyr to 50 kyr as the lithosphere flexes. We also see how a fore-bulge develops outside the load where the induced S_H becomes tensional. The direction of S_H is perpendicular to the long-axis of the ellipsoid under the ice, as expected since the stress depends on the change in displacement and thus S_H follows the maximum curvature as long as it is compressive. Outside the ice front, however, it rapidly rotates to align itself with the outline of the ice sheet reflecting the low (tensional) stress in the fore-bulge region. The fore-bulge moves toward the centre of the ice depression as the ice disappears and 8 kyr after deglaciation, in Figure 3-2D, we see that a wave like pattern has developed in both magnitude and direction of S_H. We also note how the stress directions under the former ice sheet rotate as the lithosphere rebounds.

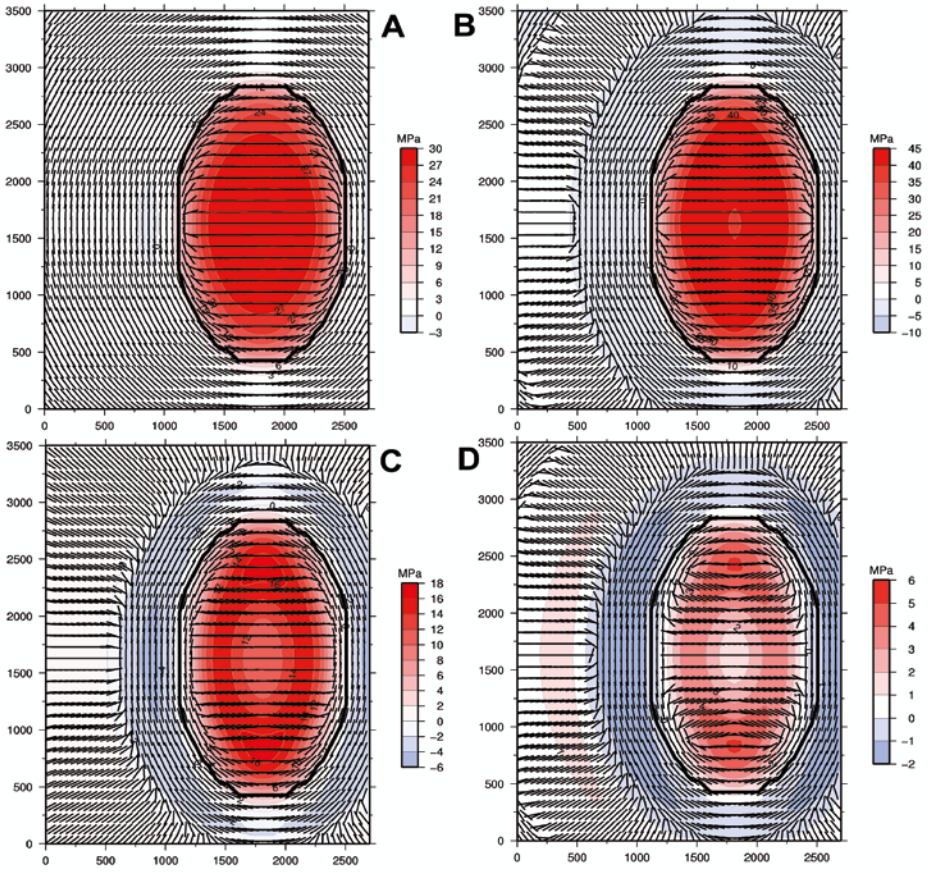

Figure 3-2. *Modelling an ellipsoidal ice sheet (black line). Magnitude and direction of the maximum horizontal stress at (A) 10 kyr, (B) 50 kyr, (C) 60 kyr and (D) 68 kyr.*

Turning now to the comparison of 2D and 3D models we plot the horizontal northward stress S_{NN}, Figure 3-3, and the maximum shear stress, Figure 3-4, along the north-south profile both for the 3D model and using a 2D section of the ellipsoidal ice in a 2D model. As the 2D model implicitly assumes that the ice is infinite in the east-west direction, we expect to see some differences in the earth responses. Figure 3-3 shows that the S_{NN} stresses develop very similarly through the loading phase and while the load resides on the model. There are slight differences in the distribution of the stresses in 2D and 3D, the high stresses continue deeper in 2D, but the differences are generally small both in magnitude and distribution. During deglaciation, however, the two models diverge and the 3D model has stresses that remain higher for a longer time than in the 2D model. The difference in positive stress magnitudes is up to 50% at 60 kyr and higher at 68 kyr. In Figure 3-4 we note that the 3D model has higher and more widely distributed shear stresses during the entire glacial period. The stress differences are not very large and only amount to a few MPa. These differences in 2D and 3D induced stresses is easily understood in terms of the additional flexure of the lithosphere caused by the 3D shape of the ellipsoid. We noted already in Figure 3-1 that shear stresses are in fact higher along the east-west axis and these flexural stresses affect the entire model. We conclude that there are substantial differences between the induced stresses in 2D and 3D models when the ice sheet has dimensions such as those used here. Based on the behaviour during deglaciation in this model we would also predict that for an ice sheet which grows and melts in pulses, the stress differences between 2D and 3D models will increase. The 2D stress results obtained in /Lund 2005a, 2006b/ may therefore be less suitable to use as input for repository related assessment.

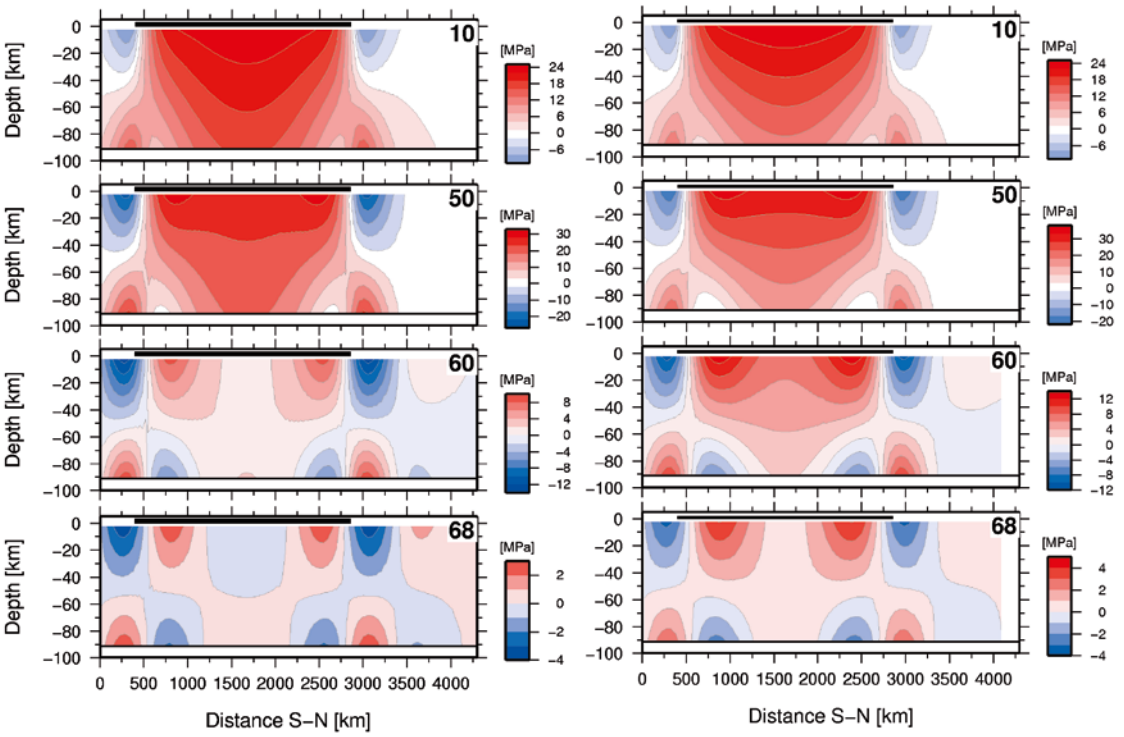

Figure 3-3. *The horizontal normal stress S_{NN} along a north-south profile. The left column shows the 2D results and the right column the 3D results. The rows show snapshots in time, with the time in kyr indicated on the plots. The black bar at depth zero indicates the extent of the ice sheet. Red are positive and blue negative stresses.*

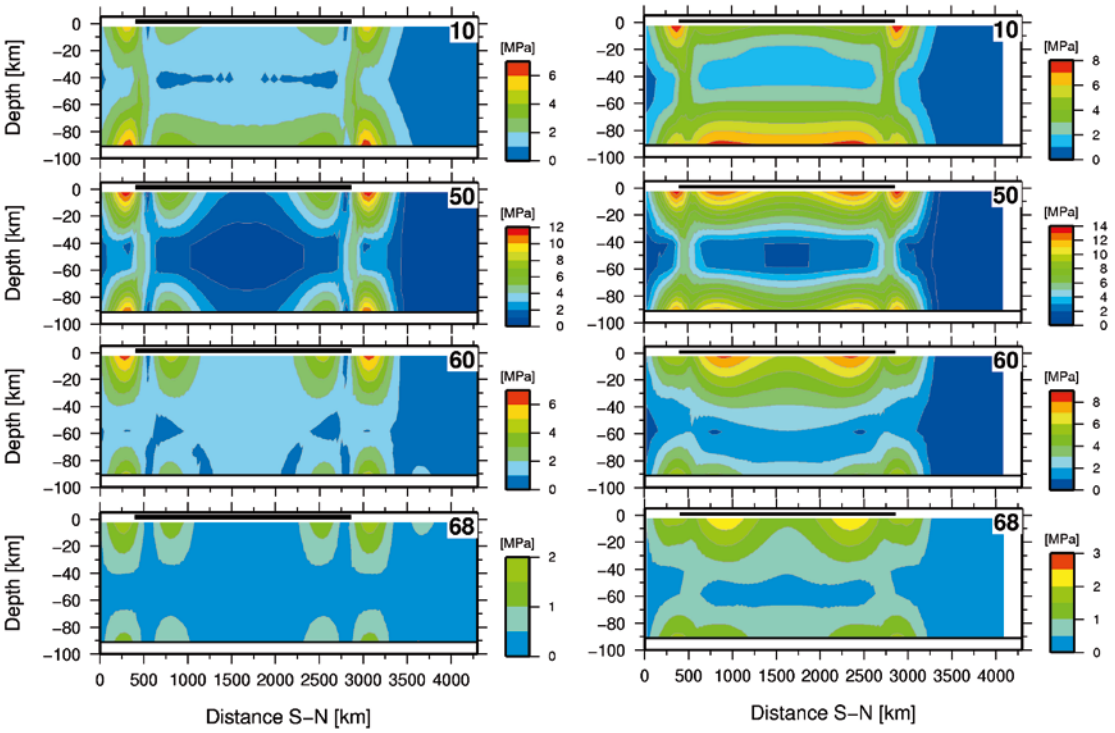

Figure 3-4. *The maximum shear stress along a north-south profile. The left column shows the 2D results and the right column the 3D results. The rows show snapshots in time, with the time in kyr indicated on the plots. The black bar at depth zero indicates the extent of the ice sheet.*

4 Models of the Weichselian glaciation

The ice model is one of the two corner stones in GIA applications (the second being the earth model) and a well calibrated, detailed ice model is a prerequisite when comparing the displacements from GIA modelling with real data. There are a number of ice models available for the Weichselian glaciation and they are essentially based on two very different principles. The first kind is constructed from geological markers of ice sheet extent at different times, such as moraines, and then the ice thickness is adjusted so that the GIA model used for ice reconstruction fits the available data (mostly relative sea-level data, tide-gauge data and GPS data). The ice models by Lambeck /Lambeck et al. 1998, Lambeck and Purcell 2003/ and Peltier /Peltier and Tushingham 1991, Peltier 2004/ are of this type.

The second kind of ice model is built from thermo-dynamical ice sheet models where palaeoclimate data govern the growth and decay of the ice sheet and geological data, such as moraines and raise shore lines, are used as constraints on the models. The ice sheet model used for the reference climate development by SKB is of this kind /Näslund et al. 2003, Näslund 2006/. The ice models have different lateral extent and different resolution, the Peltier models (e.g. ICE-3G, ICE-5G) are global models, Lambeck's group have a number of regional ice models which they join to a global model and the Näslund model is a purely regional, high resolution model of the Weichselian ice sheet.

In this study we use the /Näslund 2006/ ice model as that is the SKB reference model and as it is also the most recent high resolution model for Scandinavia, incorporating recent results on ice margin fluctuations and ice free stages /Lokrantz and Sohlenius 2006, Wohlfarth 2009/. The model resolution is 50×50 km and the model covers much of northern Europe, see Figure 4-1. We note in Figure 4-1 that the ice reached a maximum thickness in excess of 3 km at the last glacial maximum. The model spans the time period from 120 kyr BP until today and covers a simulation of the entire Weichselian ice sheet. Figure 4-2 shows the evolution of ice volume, area and temperature from the simulation used in /Näslund 2006/. We see that, after early phases of ice sheet development around 100 to 80 kyr BP, there are two main periods of ice cover during the Weichselian in this reconstruction. The first is during Marine Isotope Stage (MIS) 4, around 60 kyr BP, and the second at MIS 2, around 20 kyr BP. Between these two periods, the ice sheet is considerably smaller (during MIS 3). This development is in line with most, but not all, recent information on the Weichselian glacial history /Näslund et al. 2008, Wohlfarth 2009/. The two main periods of ice sheet coverage will be prominent in our models of the temporal evolution of stress and fault stability below. Only the ice history from 68 kyr BP onwards was used in our simulations as the early stages of the ice development includes much smaller and thinner ice sheets with small ice volumes, Figure 4-2, 4-3, and in parts are more uncertain /Näslund 2006, personal communication/. Instead we initialize the model using a 1,000 year long ramp to reach the 68 kyr ice cover. At 68 kyr BP only the mountainous region of south-central Norway was ice covered. We see in Figure 4-1 that the ice model also includes part of the ice sheet on north-easternmost Greenland. Since we only have data for a very small portion of Greenland we have neglected the Greenland ice sheet in this study. The ice sheet reconstruction of /Näslund 2006/ used calibration against geological information on dated ice marginal positions when available, except in the northernmost parts, which have resulted in that the ice sheet coverage over Barents sea is highly uncertain. Figure 4-4 shows snapshots of the extent of the ice at 14, 13, 12 and 11 kyr BP, illustrating how rapidly the ice retreated during the later stage of deglaciation. At 10.3 kyr BP the model shows mainly ice free conditions in Fennoscandia.

Although originally run at higher temporal resolution, the extracted ice model is defined in 1,000 year intervals from 68 kyr BP to 20 kyr BP and from there on in 100 year intervals. Figure 4-5 shows the ice time histories at Forsmark and Oskarshamn, we see that the ice reaches almost 3 km thickness over Forsmark and almost 2.5 km thickness over Oskarshamn. The ice cover over Forsmark also last for a longer time period than it does over Oskarshamn. During the stadial at approximately 60 kyr BP the difference in ice coverage at Forsmark and Oskarshamn is especially noticeable, we will see the effect of this later in the modelling results. Figure 4-5 also includes a recent ice model by /Lambeck 2005/. We see that there are pronounced differences in both the thickness and duration of the ice cover at LGM (Last Glacial Maximum).

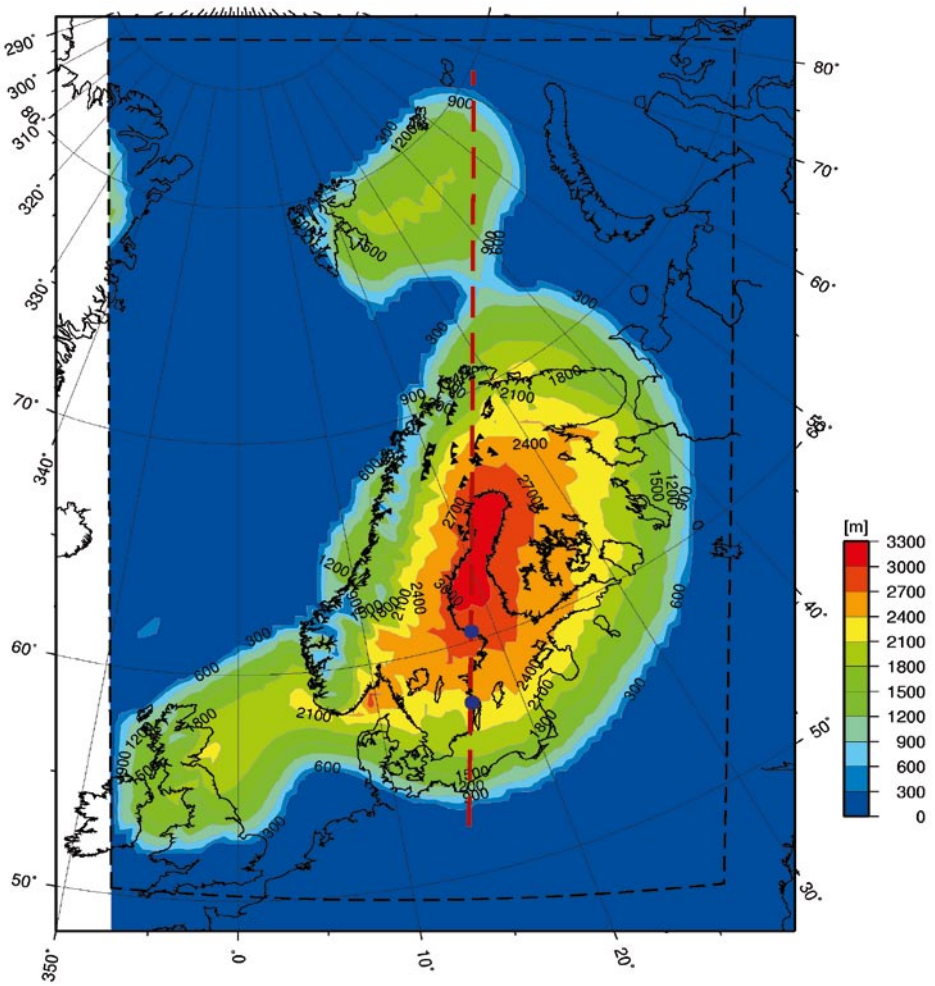

Figure 4-1. *Ice thickness in the Weichselian ice sheet simulation by /Näslund 2006/ at 18.4 kyr BP when the ice has its largest extent. The ice sheet reconstruction is calibrated against geological information on dated ice marginal positions, except in the northernmost parts which has resulted in the ice coverage over Barents sea probably being too small. The 2D profile used in /Lund 2006b/ is marked by the red dashed line, the large end-glacial faults of northern Scandinavian are marked by black triangles (Olesen, personal comm.) and the proposed nuclear waste repository sites, Forsmark and Oskarshamn, have been marked with blue dots on the 2D line. The black dashed line outlines the boundary used as the interior box in the 3D finite element model.*

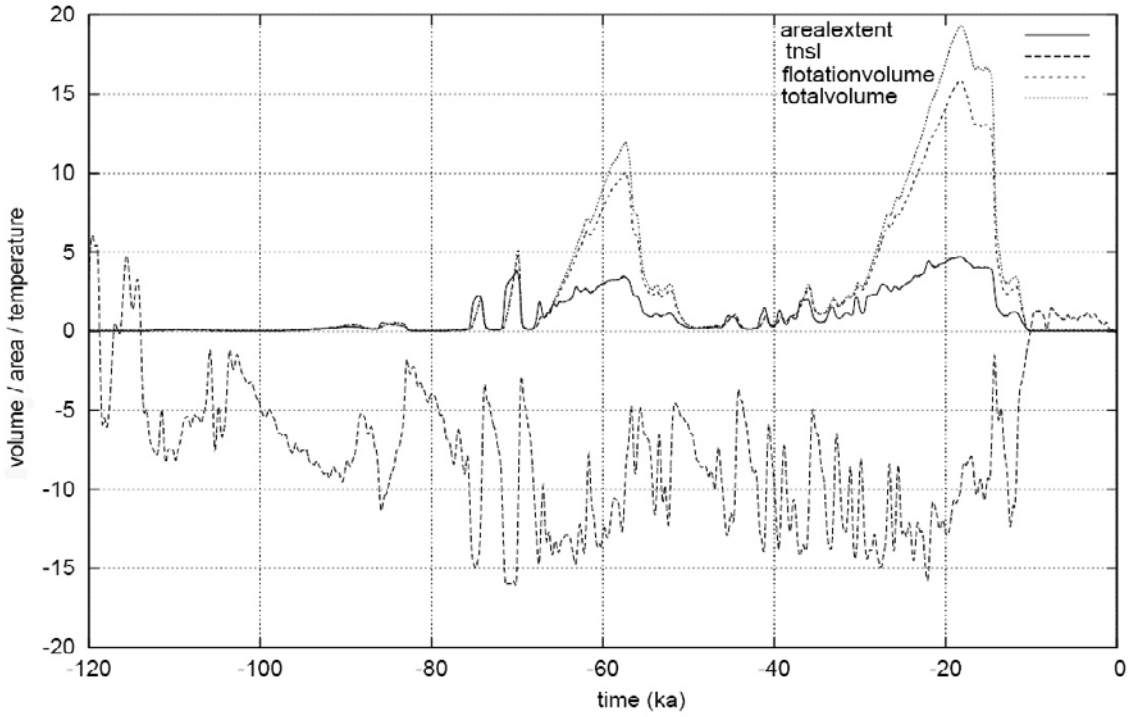

Figure 4-2. *Temporal evolution of the Weichselian ice sheet simulation by /Näslund 2006/. Shown is the temperature near sea-level (tnsl) in degrees C, the areal extent in Mkm², total volume and total volume minus the volume of floating ice (flotation volume), in units of meter sea-level.*

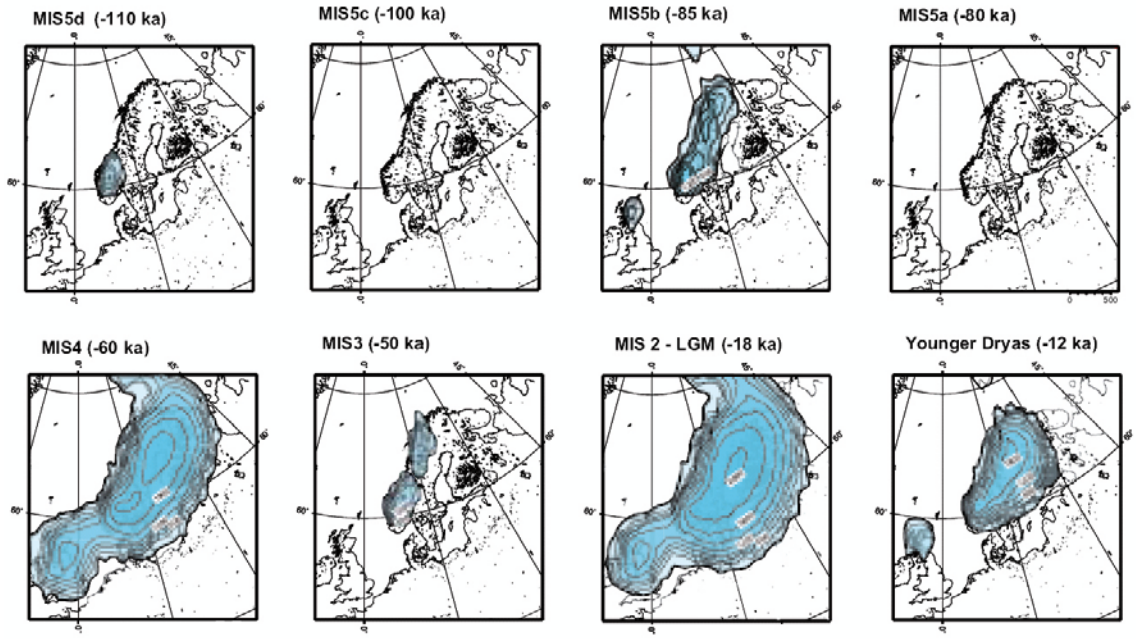

Figure 4-3. *Selected maps of ice thickness during the Weichselian in the reference glacial cycle simulation. The ice sheet grows to its full LGM configuration in progressive phases of increasing maximum extent, with intervening periods of more restricted ice coverage. MIS is Marine Isotope Stage. Figure from /Näslund 2006/.*

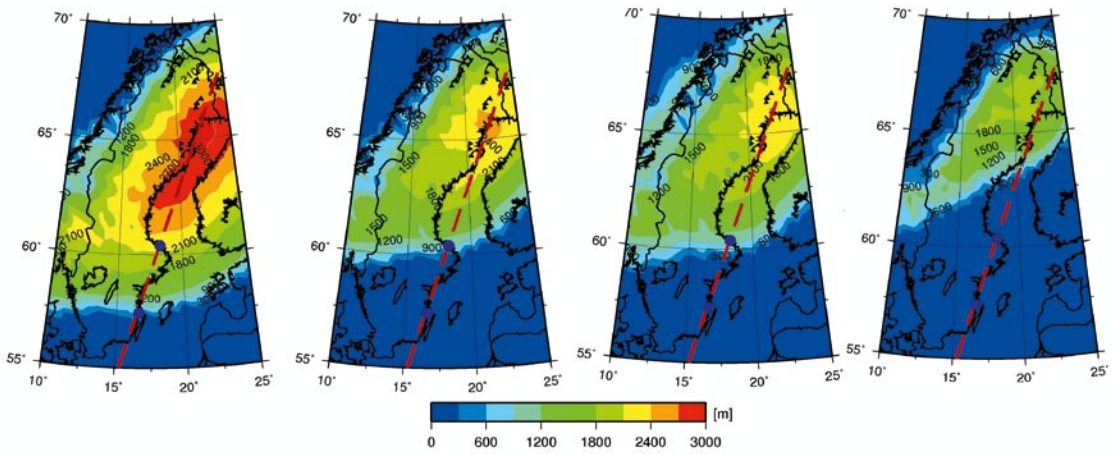

Figure 4-4. *Ice thickness at 14 kyr BP, 13 kyr BP, 12 kyr BP and 11 kyr BP, from left to right, respectively, from the /Näslund 2006/ model. The 2D profile used in /Lund 2006b/ is marked by the red dashed line and the proposed nuclear waste repository sites, Forsmark and Oskarshamn, have been marked with blue dots on the 2D line.*

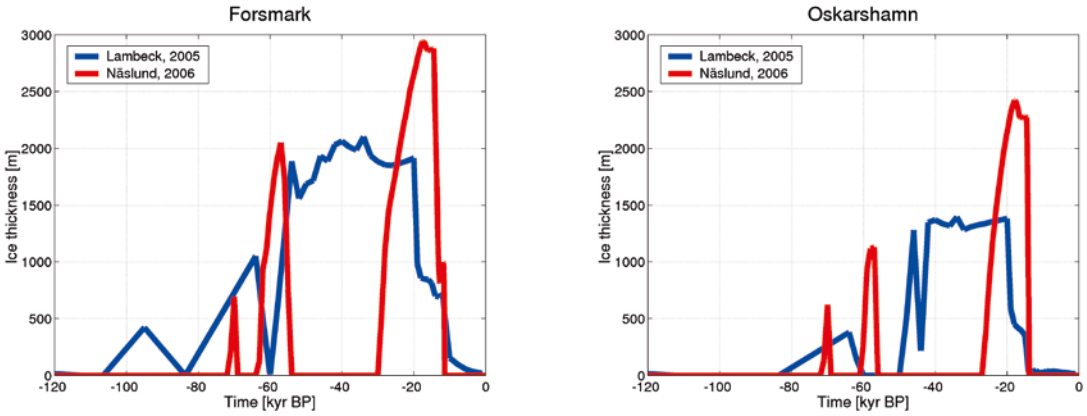

Figure 4-5. *Ice thickness histories at Forsmark, left, and Oskarshamn, right. In red the ice sheet simulation by /Näslund 2006/ and in blue the simulation by /Lambeck 2005/. The smaller peak at approximately 70 kyr BP in the /Näslund 2006/ simulation will not be included in the modelling in this study due to its uncertainty (Näslund, personal communication).*

It is today generally believed that previous Late Pleistocene glaciations over Fennoscandia have had basically the same course of events, in that the ice sheets started to grow in the Scandinavian mountains with subsequent expansion over surrounding lowlands /e.g. Porter 1989, Kleman and Stroeven 1997/. There are variations in maximum ice sheet configurations, with the largest ice sheet occurring during the penultimate glaciation, i.e. during the Saalian glaciation /e.g. Svendsen et al. 2004/. In line with this, the Saalian ice sheet was larger also than the last, Weichselian, ice sheet, especially east of Fennoscandia where it stretched far into Siberia. Over Fennoscandia and in northern Europe, the difference between the maximum configurations of the Saalian and Weichselian ice sheets is considerably smaller. Nevertheless, comparing the last and the penultimate glaciations, the last Weichselian ice sheet constitute a more representative Late Pleistocene Fennoscandian ice sheet, not being the largest nor the smallest one. There is no reason to believe that a future ice sheet over Fennoscandia would be fundamentally different than previous Late Pleistocene Fennoscandian ice sheets. Therefore, a Weichselian ice sheet reconstructed by a thermo-dynamic ice sheet model /Näslund 2006/ was selected for the present study to investigate how a future glaciation will affect the crustal stresses in Fennoscandia in general and at the proposed nuclear waste repository sites in particular. For the purpose of studying how different ice sheet models affect the crustal stress history during a glacial cycle it would have been advantageous to include an additional ice sheet model, based on different principles. The differences in the /Näslund 2006/ and /Lambeck 2005/ models in Figure 4-5 indicate that we could probably expect significant differences in both crustal displacements and stress.

5 Solid earth models

The focus of this study is the three-dimensionality of the models used to predict the response of the solid Earth to glaciation. We construct a three dimensional finite element (FE) model in the sense that we model a three-dimensional block of the Earth. However, the ice load is represented by a two-dimensional distribution of pressure sources and many of the earth models presented here are in fact one-dimensional, in the sense that material parameter only vary with depth. Nevertheless, the 3D FE model is necessary in order to properly model the effect of the ice sheet on the solid Earth.

5.1 The finite element model

Due to the large model domain, the need to model stresses at repository depth, approximately 500 m, and our lack of access to a large parallel computer, we had to divide each model run into two stages. We first run a coarse large scale model incorporating the entire ice model domain and then a fine meshed sub-model in the region of interest. The computations have been carried out with the commercial finite element software Abaqus /ABAQUS 2007/ on a dual processor Itanium2 computer with 24 GB memory. The models use 8-node solid elements (hexahedrons) with reduced integration (C3D8R) in the interior of the mesh and 8-node infinite elements (CIN3D8) as the outer boundary, effectively simulating stress boundary conditions. In addition, SPRING1 elements are used at all density contrasts, as discussed in Section 2.

The large scale models contain a central box of elements whose upper surface area is determined by the area of the /Näslund 2006/ ice model at LGM, see Figure 5-1. The ice model uses a 50×50 km grid and covers 82×56 elements which is equivalent to 4,100 km in the X-direction (approximately north, see Figure 4-1) and 2,800 km in the Y-direction (approximately east). Vertically the central box contains 12 elements spanning the distance from the surface to 1,200 km depth. Half of these elements are thinner and are generally situated in the upper 100 km, although for the models with internal topography on the lithosphere-asthenosphere boundary this distance varies. The central box is embedded in a half-sphere which extends out to a radius of 41,000 km, in accordance with /Lund 2005a/ who found that in spite of the use of infinite elements on the boundary, the model should

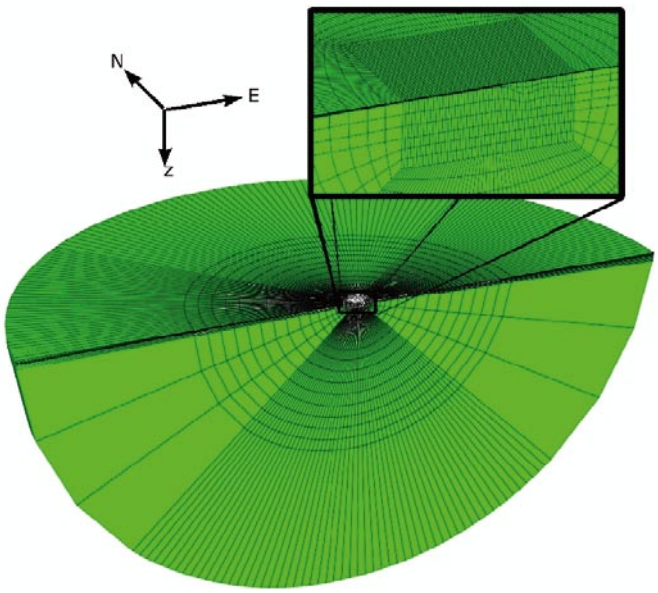

Figure 5-1. *Section through the large scale finite element model. The model has an interior box of 4,100×2,800×1,200 km and is then expanded into a half-sphere. The outermost layer of elements are infinite elements. The inset shows lateral variation in lithosphere thickness. Sub-models are defined in the interior box using only a few layers of the large scale elements shown here.*

be at least a factor 10 larger than the half-width of the load. Beyond 41,000 km we attach infinite elements as stress boundary conditions. The spherical shells are only used to shield the interior model and we do not use any data from outside of the central box. These large scale models contain approximately 260,000 elements, use 14 GB of computer memory and take 30–35 hours to run.

Two sub-models were run for each large scale model, zooming in on the two sub-regions shown in Figure 5-2. The sub-models have 10×10×1 km elements in the upper 15-20 km, depending on the type of model, and then the element thickness is adjusted to ensure that the sub-model is terminated on an element face in the large model. The 1 km thick elements at the surface allow stress estimates at the centroid depths of 500 m, as needed for repository depth inferences. The sub-models inherit their material properties from the large scale models and are driven by the displacements estimated by the large model, effectively acting as boundary conditions on the model. Therefore, no spring elements need to be attached to the surface nodes to account for pre-stress advection, as this is already accounted for by the displacement field. At internal density contrasts, however, springs have to be attached also in the sub-model. Abaqus includes a mechanism to run sub-models like these from the large scale models. Unfortunately, the Abaqus mechanisms did not work satisfactory, apparently due to the bilinear interpolation performed when distributing the large scale displacement field onto the sides of the sub-model. We ended up implementing our own interpolation scheme and using the interpolated displacements as boundary conditions, constraining all degrees of freedom of the boundary nodes on the sub-model. To ease the interpolation and make it as correct as possible, all sides of the sub-models coincide with nodal planes in the large model and the time stepping is equal in both the large scale and sub-models.

We step through the ice model in 1,000 year time steps from 68 to 20 kyr, using a linear load interpolation between ice definitions. From 20 kyr we use 500 year steps through the end of the glaciation up until the last 1,000 years which are modelled in smaller time steps to allow comparison with relative sea-level, tide-gauge and GPS data.

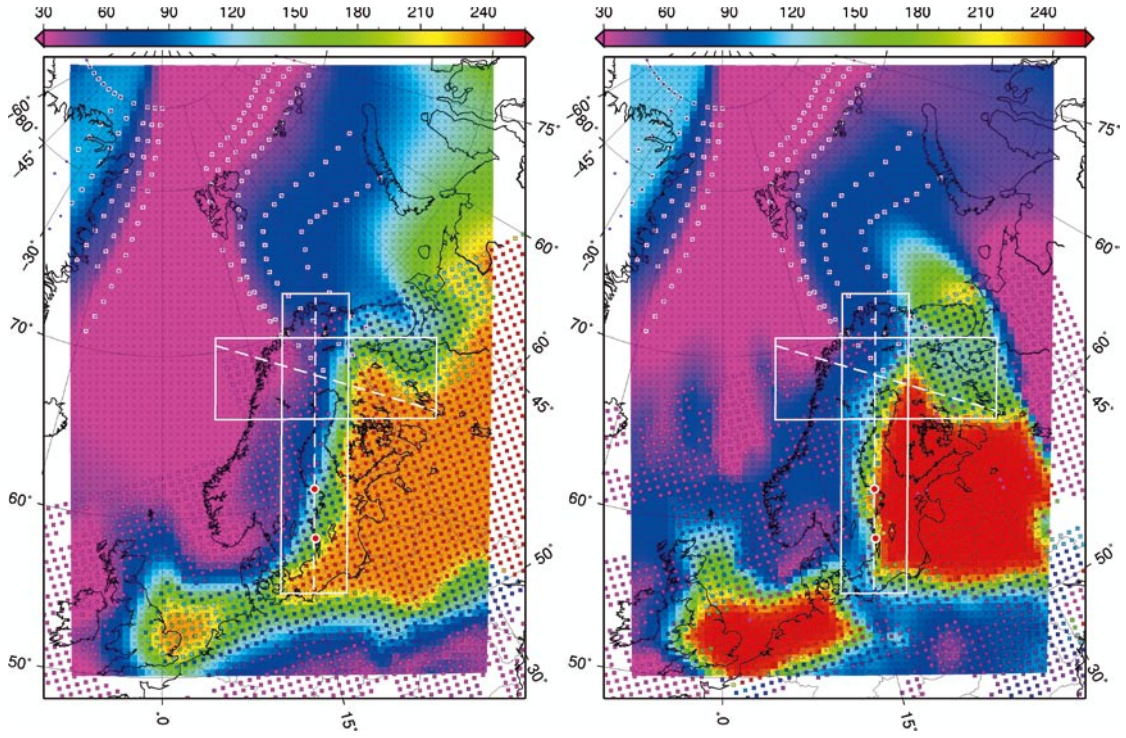

Figure 5-2. *Models of lithospheric thickness based on scaled estimates from /Perez-Gussinye et al. 2004, Perez-Gussinye and Watts 2005, Priestly and McKenzie 2006, Artemieva and Thybo 2008/. The map to the left shows lithospheric thickness based on gravity data and Bouger coherence modelling, the map to the right is based on the same data but using free-air admittance modelling. The white boxes show the sub-regions where finite element sub-models were used to increase the resolution and the white dashed lines are 2D profiles used in /Lund 2006b, Lund and Näslund 2009/. The coloured small squares indicate where the models are constrained with data from studies referred to in the text.*

5.2 Material descriptions

We have tested a number of solid earth models with different rheological stratification, both with planar, horizontal layers and layers with significant lateral variation. Common to our models is an upper, purely elastic compressible structure representing the lithosphere and a lower incompressible Maxwell viscoelastic structure representing the mantle below the lithosphere. We use an incompressible sublithospheric mantle in order to simplify the modelling, as discussed above, and since e.g. /Árnadóttir et al. 2009/ showed that the compressibility of the sublithospheric mantle has little effect on near surface displacements. In Abaqus the elastic material parameters used are Young's modulus, Poisson's ratio and density. For viscoelastic material the viscosity is the only additional parameter. The models presented below have been chosen either to agree with models used in previous studies, such as in /Milne et al. 2004, Lund 2005a, 2006b/, or to explore how variations in these parameters affect the results. We have chosen to focus on the structure of the lithosphere and ignore effects of lateral viscosity variations in the mantle, although /Wang and Wu 2006, Whitehouse et al. 2006/ indicate that such variation could potentially be resolved by current GPS resolution. Our models fall into two classes, one with planar horizontal layers and one where there is topography on the lithosphere-asthenosphere boundary (LAB), see Figure 5-3. Elastic parameters in the models are generally derived from volume averages of the Preliminary Reference Earth Model (PREM) /Dziewonsky and Anderson 1981/. Viscosities for the mantle are taken from /Klemann and Wolf 1998, Milne et al. 2004, Lund 2006b/. The displacement response of the models below will be tested against current GPS data in chapter 6 and only some of the models will be further studied.

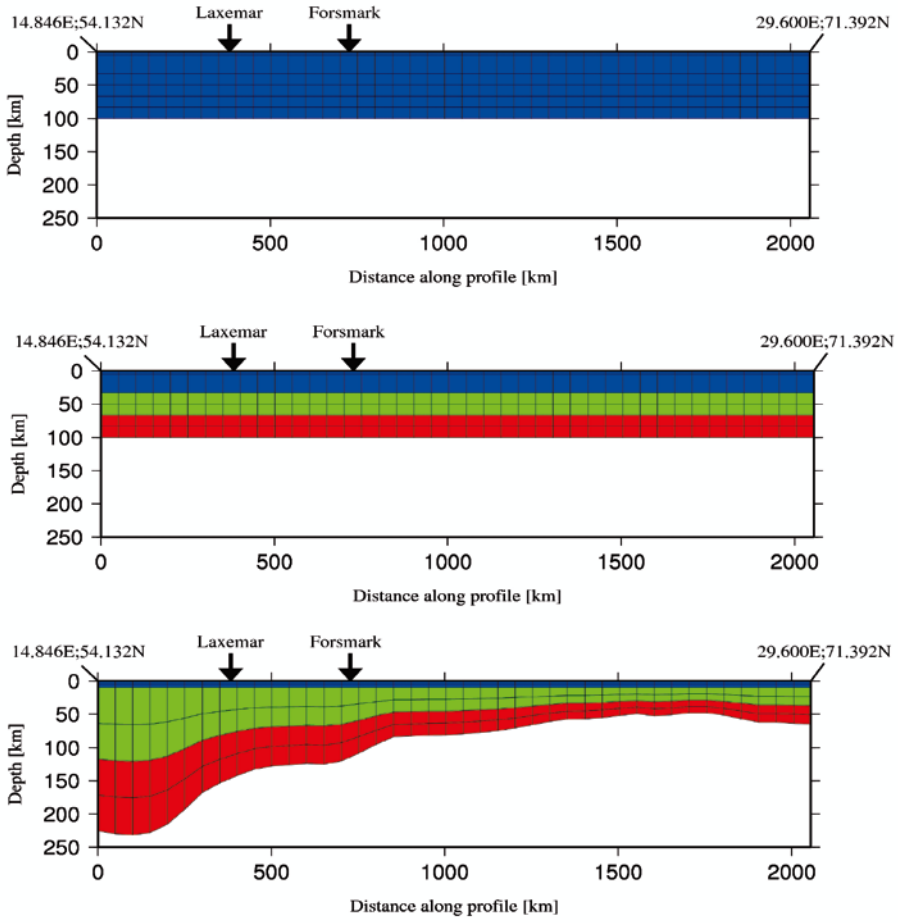

Figure 5-3. *Illustrations showing typical depth sections through the finite element models along the 2D north-south profile indicated in Figure 5-2. The upper panel shows a uniform flat 100 km lithosphere, as Model 1. The middle panel shows Model 2, with three uniform horizontal layers. The lower panel shows Model 3 with laterally varying lithospheric thickness. The colours indicate different elastic parameters at different depths in the lithosphere, but are not necessarily the same from model to model.*

5.2.1 Horizontally stratified models

The material parameters for the models can be found in Table 5-1. Here are brief descriptions. Note that the T in the model names below does not have any significance.

Model 1: This model corresponds to model A of /Lund 2006b/ and has a 100 km thick uniform compressible elastic plate overlying an incompressible viscoelastic half-space with viscosity 10^{21} Pa s, see Figure 5-3. This model is also identical to model EE of /Klemann and Wolf 1998/.

Model 2: This model corresponds to model K of /Lund 2006b/ with a three-layered 100 km thick compressible elastic plate overlying a viscoelastic half-space with viscosity 10^{21} Pa s, see Figure 5-3. The elastic layer boundaries are at 33, 67 and 100 km depth, and the volume average of Young's modulus for the entire lithosphere is the same as for *Model 1*. Note, however that the flexural rigidity of *Model 2* is only 83% of that of *Model 1*.

Model T5: Similar to *Model 1* but with an elastic plate thickness of 50 km.

Model T7: Model with a three-layered 100 km thick compressible elastic plate overlying a viscoelastic half-space with viscosity 3×10^{21} Pa s /Milne et al. 2004/. The elastic layer boundaries are at 15, 50 and 100 km depth. The material parameters are different from those of *Model 2*, and the lithospheric volume average of Young's modulus is 149 GPa, significantly lower than the 192 GPa of *Model 1* and *Model 2*. Models T7, T8 and T9 have elastic properties and discontinuities more in agreement with seismic results for Fennoscandia, but varying mantle viscosities.

Model T8: Identical to *Model T7* in the elastic layer but with a two-layered viscosity structure in the mantle; viscosity 8×10^{20} Pa s down to 670 km and 1×10^{22} Pa s below /Milne et al. 2004/.

Model T9: Identical to *Model T7* but uses a half-space viscosity of 1×10^{21} Pa s.

Table 5-1. Material parameters for horizontally stratified solid earth models.

Model 1						**Model 2**					
Layer	**To depth [km]**	**Density [kg/m³]**	**Young's [GPa]**	**Poisson's ratio**	**Viscosity [Pa s]**	**Layer**	**To depth [km]**	**Density [kg/m³]**	**Young's [GPa]**	**Poisson's ratio**	**Viscosity [Pa s]**
1	100	3,380	192	0.25	–	1	33	2,730	90	0.25	–
2	–	3,380	435	0.4999	1×10^{21}	2	67	3,370	196	0.25	–
–	–	–	–	–	–	3	100	3,380	290	0.25	–
–	–	–	–	–	–	4	–	3,380	435	0.4999	1×10^{21}
Model T5						**Model T7**					
1	50	3,380	192	0.25	–	1	15	2,750	64	0.28	–
2	–	3,380	435	0.4999	1×10^{21}	2	50	3,251	156	0.28	–
–	–	–	–	–	–	3	100	3,378	170	0.28	–
–	–	–	–	–	–	4	–	3,891	452	0.4999	3×10^{21}
Model T8						**Model T9**					
1	15	2,750	64	0.28	–	1	15	2,750	64	0.28	–
2	50	3,251	156	0.28	–	2	50	3,251	156	0.28	–
3	100	3,378	170	0.28	–	3	100	3,378	170	0.28	–
4	670	3,610	217	0.4999	8×10^{20}	4	–	3,891	452	0.4999	1×10^{21}
5	–	4,000	553	0.4999	1×10^{22}	–	–	–	–	–	–

5.2.2 Laterally varying lithosphere

As demonstrated by a number of authors e.g. /Kaufmann and Wu 1998, 2002, Kaufmann et al. 2000, Latychev et al. 2005, Steffen et al. 2006, Wang and Wu 2006, Whitehouse et al. 2006, Klemann et al. 2008/, the lateral structure of the Earth significantly influence GIA model results and /Whitehouse et al. 2006/ showed that the differences between a 1D model and a true 3D model are larger than the uncertainties in current permanent GPS networks, such as BIFROST, and therefore could be observed. However, /Spada et al. 2006/ conclude that until ice models are more accurate, relative sea-level observations cannot be used to constrain 3D structure and /Wang and Wu 2006, Whitehouse 2009/ show that heterogeneities at different depths in the Earth produce perturbations that are similar or mask those from other depths and that it therefore may be difficult to uniquely constrain the Earth's structure /Whitehouse 2009/. In addition /Martinec and Wolf 2005/ showed that the central uplift under the ice sheet is relatively insensitive to lithospheric thickness. Considering the rapid change in lithosphere thickness expected on an east-west profile from central Finland to the North Atlantic ocean we decided to construct a laterally varying lithospheric thickness model for Fennoscandia in order to asses how such models affect the displacement and stress fields. Estimating the lithospheric thickness is, however, not a trivial task as it is strongly dependent on the type of data used. Seismological inferences of the depth to the LAB typically produce relatively large depths in Scandinavia, 200–300 km, e.g. /Olsson et al. 2007/. Heat flow data and thermal modelling generally give similarly large or slightly smaller depths, 150–200 km, /e.g. Artemieva and Thybo 2008/ and magetotelluric data produce yet another LAB. GIA models yield a significantly smaller LAB depth, typically around 100 km in Scandinavia /Wolf 1993, Milne et al. 2004/ and effective elastic thickness estimates from gravity data generally produce the thinnest lithosphere, 40–80 km /Perez-Gussinye et al. 2004/. As we are interested in the mechanical properties of the lithosphere, estimates from GIA and gravity seem the most appropriate and since there are no independent estimates of varying lithospheric thickness from GIA we will use the /Perez-Gussinye et al. 2004, Perez-Gussinye and Watts 2005/ (PG) estimates as a basis for our laterally varying models. We do not use the PG estimates "as is" since the Bouger coherence and free-air admittance models that they stem from refer to tectonic, orogenic time-scales and are probably not appropriate for the GIA time-scale. Instead we follow /Whitehouse et al. 2006/ and rescale the PG estimates. An additional problem is that the PG model does not cover the Barents Sea nor the north-western part of the model. In order to have constraints on the continental lithosphere thickness in these regions, we use the results of /Priestly and McKenzie 2006, Artemieva and Thybo 2008/. The trends of lithospheric thickness in these studies are compared to the PG models and we convert these generally thicker lithospheres to a model which is in general agreement with the PG thickness. As opposed to /Whitehouse et al. 2006/ we do not have a global model but scale the average lithosphere thickness within our FE interior box such that it equals a "normal" GIA elastic plate thickness of 100 km. Our lithospheric thickness model based on the PG Bouger coherence model is shown in Figure 5-2, left, and a model based on the PG free-air admittance model is shown to the right in Figure 5-2. Due to meshing constraints we have fixed the thinnest, oceanic parts of the lithosphere to 30 km thickness and see that in order to have a 100 km average the thickest sections of the model grow to 240 km. It should be noted that although the general trend of the PG model, thickening from the Atlantic into central Finland, agrees with seismological inferences, the thickening of the model from central Sweden south into Germany is in stark contrast to the seismological models e.g. /Shomali et al. 2002/. We also note that the model based on free-air admittance has a thin zone in the north-south direction over southern Sweden.

Material parameters for the laterally varying models can be found in Table 5-2. Short descriptions follow here:

Model 3: Lithosphere thickness based on the PG Bouger coherence model with 100 km average thickness. Three compressible elastic layers in the lithosphere where the upper layer is 10 km thick uniformly over the entire region. The two lower layers follow the lithospheric topography and therefore reach depths from 20 to 122 km and from 30 to 234 km, respectively, see Figure 5-3. The sublithospheric mantle has two layers, one above 670 km and one below with viscosities 8×10^{20} Pa s and 1×10^{22} Pa s, respectively.

Model T1: Lithosphere thickness based on the PG free-air admittance model with 100 km average thickness. Three compressible elastic layers in the lithosphere where the upper two layers have uniform 10 km thickness over the model, reaching 10 km and 20 km depth, respectively and the third layer varies with topography, from 30 km depth to 258 km depth. Otherwise as *Model 3*.

Model T10: Similar to *Model 3* but the average thickness is 170 km, varying from 90 km to 350 km, more in accordance with the Scandinavian section of the model by /Whitehouse et al. 2006/.

Model T12: Similar to Model 3 but with uniform viscosity of 1×10^{21} Pa s in the sublithospheric mantle layers.

Table 5-2. Material parameters for laterally varying lithospheric thickness models.

Model 3 Bouger coherence, 100 km average					**Model T1** Free-air admittance, 100 km average				
Layer depth to bottom	**Density [kg/m³]**	**Young's [GPa]**	**Poisson's ratio**	**Viscosity [Pa s]**	**Layer** depth to bottom	**Density [kg/m³]**	**Young's [GPa]**	**Poisson's ratio**	**Viscosity [Pa s]**
1 10 km	2,750	64	0.28	–	**1** 10 km	2,750	64	0.28	–
2 20–122 km	3,210	148	0.28	–	**2** 20 km	3,210	148	0.28	–
3 30–234 km	3,375	169	0.28	–	**3** 30–258 km	3,375	169	0.28	–
4 670 km	3,650	228	0.4999	8×10^{20}	**4** 670 km	3,650	228	0.4999	8×10^{20}
5 ———	4,040	597	0.4999	1×10^{22}	**5** ———	4,040	597	0.4999	1×10^{22}
Model T10 Bouger coherence, 170 km average					**Model T12** Bouger coherence, 100 km average				
1 10 km	2,750	64	0.28	–	**1** 10 km	2,750	64	0.28	–
2 50–180 km	3,210	148	0.28	–	**2** 20–122 km	3,210	156	0.28	–
3 90–350 km	3,375	169	0.28	–	**3** 30–234 km	3,375	170	0.28	–
4 670 km	3,650	228	0.4999	8×10^{20}	**4** 670 km	3,650	452	0.4999	1×10^{21}
5 ———	4,040	597	0.4999	1×10^{22}	**5** ———	4,040	452	0.4999	1×10^{21}

6 Observational constraints

This study is primarily focussed at understanding the distribution of glacially induced stress and its effect on fault stability. We do not aim at determining an optimal structural earth model by fitting model predictions to observables such as GPS or relative sea-level data. Notwithstanding, we would like to know that the models we use to study stress patterns and magnitudes are able to predict observables in reasonable agreement with the data. We are also interested in how laterally varying lithospheric thickness affects the observables. Only the large scale finite element models will be used for the analysis in this section. We compare our models to GPS data collected and analysed in the Bifrost project /Lidberg et al. 2007/ and relative sea-level data from three sites in the Baltic /Whitehouse 2007/.

6.1 Current velocities from GPS data

The Bifrost data is collected at high quality GPS stations in Fennoscandia and countries along the Baltic and North Sea coasts, see Figure 6-1 which also shows the processed vertical and horizontal station velocities (in the ITRF2000 reference frame). We see in Figure 6-1 the well known pattern of glacial rebound centred in the Bothnian Bay, with a maximum amplitude of approximately 11 mm/yr. We also see how the relatively small horizontal velocities, 1–2 mm/yr, point in a general radial direction away from the centre of rebound and that they are very small in central Europe, away from the former ice sheet. Using our GIA models we predict the annual velocities over a five year interval, the last five model years, and calculate velocities at the locations of the Bifrost stations. We compare our velocities with the Bifrost data and compute χ^2 for vertical velocities, horizontal velocities and a joint χ^2 for all three velocities. We use χ^2 = WRSS/(N-m) where WRSS is the weighted residual sum of squares, WRSS = $\sum ((v^{obs} - v^{mod})/\sigma)^2$, N the number of stations and m the number of model parameters. As we are not rigorously fitting the models to the data we use m = 0 for simplicity. Below follows a rather brief summary of the difference in velocities for the different models, and their fit to the Bifrost data.

6.1.1 Horizontally stratified models

In Figure 6-1 we show the predicted velocities from our models 1, T5 and T9 together with the velocities observed in the Bifrost project /Lidberg et al. 2007/. We see that the models predict a similar pattern of uplift as that observed over Fennoscandia, with high uplift rates over the Bothnian Bay and horizontal velocities that radiate out from the centre. Reducing the thickness of the elastic lithosphere from 100 km to 50 km (Model 1 to Model T5) is shown to affect both the magnitude of the velocities but also the rebound pattern. We see an asymmetry in the vertical velocity field, which has a much higher gradient to the west than to the east, and similarly more asymmetric horizontal velocities between east and west. This is due to a much smaller filtering effect of the lithosphere, since a thick lithosphere more effectively averages out the irregularities and spatial variations in the velocity field induced by the ice load. The difference in the response of models 1 and T9 is due to a change in elastic layering and properties, see Table 5-1, with model T9 having a smaller average Young's modulus than model 1. The stiffer model 1 has generally higher velocities than model T9 but the pattern of uplift and horizontal motion is very similar. Interestingly, the pivot curve, where the vertical uplift is zero (grey contour in Figure 6-1), is almost identically located in the three models.

In Figures 6-2 and 6-3 we show the differences between the Bifrost data and our model predictions for the horizontally stratified models. We see that the residual plots all display a similar pattern, with the largest negative residuals in north-central Norrland, relatively large negative residuals around Lake Vänern and Västergötland, and in south-western Norway. Central Sweden and Norway, and southern Finland have relatively positive residuals and the highest relative residuals are found on the German North Sea coast and at the station near Lake Ladoga in Russia. The magnitude of the residuals vary significantly, they generally span 8 mm/yr for each individual model.

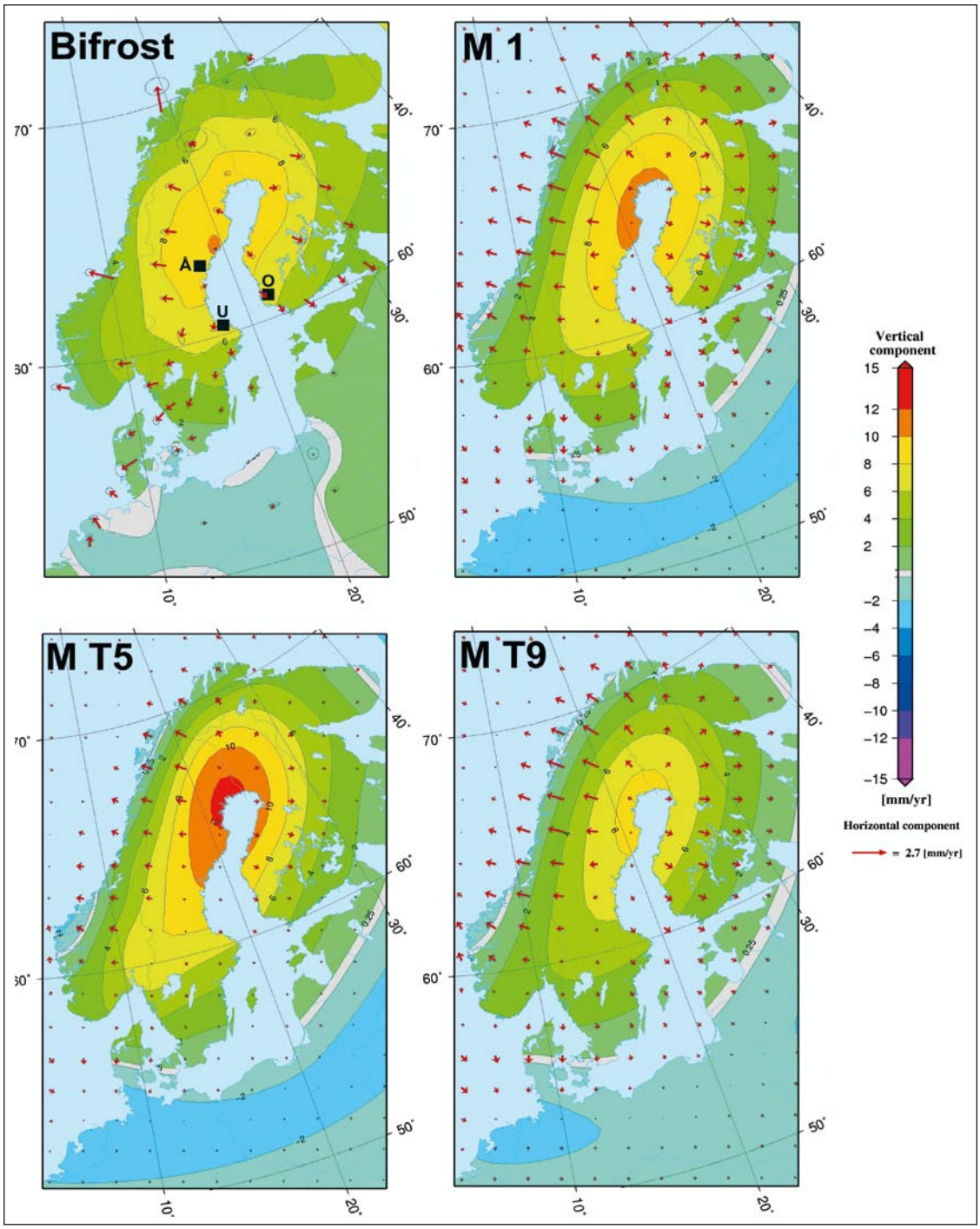

Figure 6-1. *Upper left: Results from the Bifrost project. Colour contour map of observed vertical velocities, horizontal velocities shown with red arrows. The 95% error ellipses are indicated on the horizontal velocities. Also shown are the three RSL sites, Ångerman river (Å), northern Uppland (U) and Olkiluoto (O). M1, MT5 and MT9: Predicted velocities from the respective models. The grey region represents ±0.25 mm/yr.*

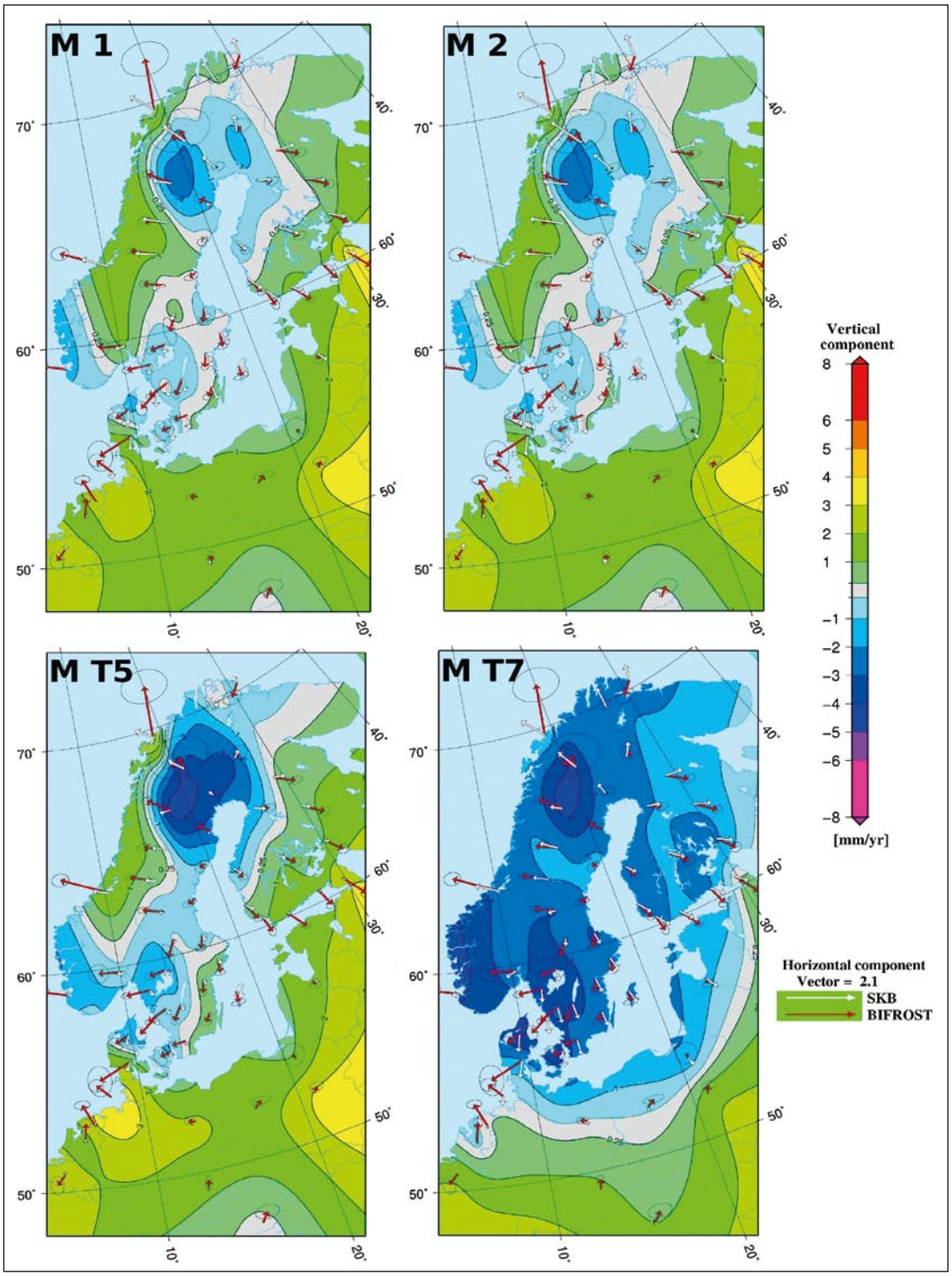

Figure 6-2. *Colour contours: differences in vertical velocities between the Bifrost data and models 1, 2, T5 and T7, respectively. The grey region represents ±0.25 mm/yr. Horizontal Bifrost velocities are shown with red arrows, model velocities with white arrows. The reference horizontal velocity vectors are in mm/yr.*

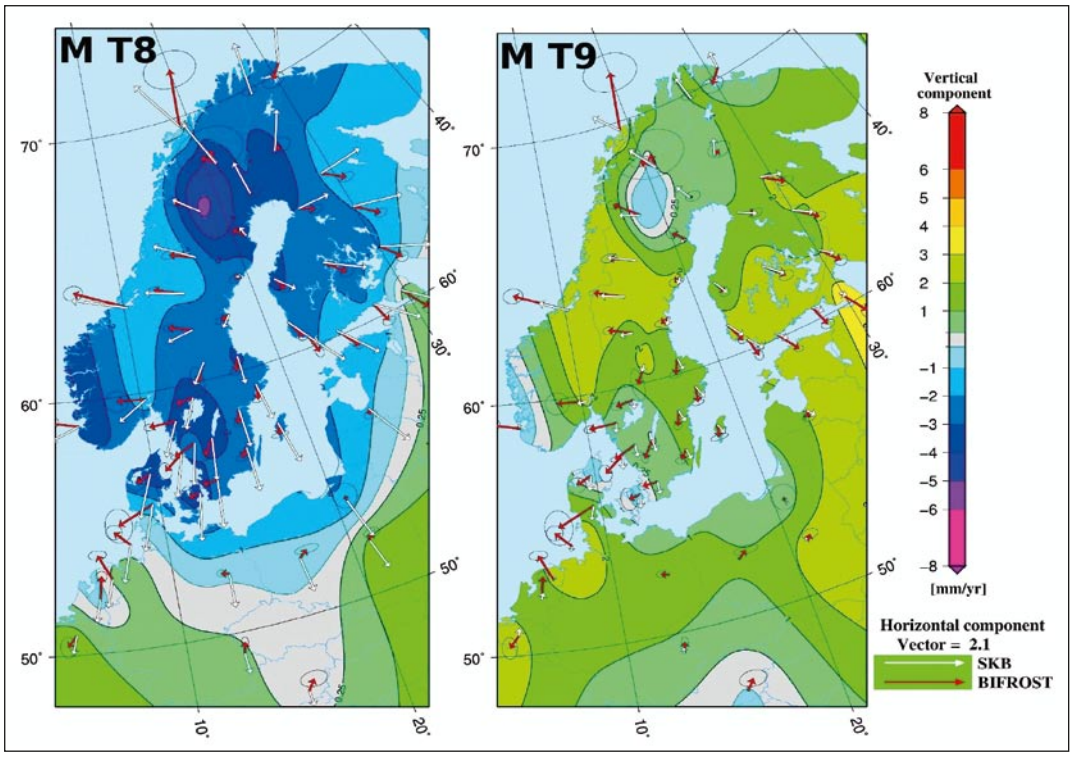

Figure 6-3. *Colour contours: differences in vertical velocities between the Bifrost data and models T8 and T9, respectively. The grey region represents ±0.25 mm/yr. Horizontal Bifrost velocities are shown with red arrows, model velocities with white arrows. The reference horizontal velocity vectors are in mm/yr.*

We see in Figures 6-2 and 6-3, and Table 6-1, that model 1 has the best fit to the data of all our tested models. Model 2 has a very similar χ^2 to model 1, indicating that the surface velocities are rather insensitive to the elastic stratification of the elastic plate if the average Young's modulus is the same. Reducing the thickness of the elastic plate to 50 km, as in model T5, produces a poorer fit to the data. This is in agreement with most GIA studies for Fennoscandia, e.g. /Milne et al. 2004/, which estimate an elastic plate thickness of approximately 100 km. We see in Figure 6-2 and 6-3 that models T7 and T8 have very similar response in the vertical velocities, which is also reflected in the vertical χ^2 . However, they vary significantly in the horizontal velocities, in agreement with /Milne et al. 2004, Steffen et al. 2006, 2007/ who found that a two layered mantle, with lower upper mantle viscosity than lower mantle viscosity, mainly affects the horizontal velocities. Model T8, with an upper mantle viscosity of 8×10^{20} Pa s, has horizontal velocities generally twice as large as those for model T7, which does not fit the data, especially in the north-south components. We also note that the viscosities of models T7 and T8, from /Milne et al. 2004/, produce current uplift that is too rapid to fit the Bifrost data using our finite element model. Model T9 is identical to model T7 except that the half-space viscosity is lowered from 3×10^{21} to 1×10^{21} Pa s. We see that the residuals are now mainly positive rather than negative, indicating that the model response is rather sensitive to the viscosity of the half-space.

Table 6-1. χ2 for the horizontally stratified earth models. North-south, east-west and vertical components, respectively plus the total χ2.

Model	North χ^2	East χ^2	Vertical χ^2	Total χ^2
1	27.4	15.8	25.9	23.1
2	39.4	16.2	27.2	27.6
T5	33.2	26.8	48.6	36.2
T7	35.1	19.7	110.5	55.1
T8	241.9	24.3	117.3	127.9
T9	26.1	18.4	59.7	34.7

As evident from Table 6-1, we do not have horizontal χ^2 that are generally a factor 3 larger than the vertical as reported by /Milne et al. 2004/. However, we note that our χ^2 are significantly larger than those of /Milne et al. 2004/. The main reason for this is probably that we use a different ice model, /Milne et al. 2004/ use a combination of ICE-3G and /Lambeck et al. 1998/, but could also partly be because we use more stations than /Milne et al. 2004/, especially south of Scandinavia, and perhaps since we use the /Lidberg et al. 2007/ velocities which have smaller uncertainties. We have, however, not explored this further.

6.1.2 Laterally varying lithosphere thickness

Figure 6-4 shows the forward responses of models 3, T1, T10 and T12. Model T1 is based on the free-air admittance results of /Perez-Gussinye et al. 2004, Perez-Gussinye and Watts 2005/ whereas the other three are based on their Bouger coherence results. We see in Figure 6-4 that the response to the glaciation varies considerably between the models, especially in the horizontal velocities. The vertical velocities show a similar pattern between models, with the centre of rebound asymmetrically displaced westward and the zone of high rebound velocities more elongated to the south-west than in the flat layered models. This is in agreement with /Kaufmann et al. 2000/. This asymmetry and elongation is due to the sharp transition from thin to thick lithosphere going from west to east. Comparing to Figure 5-2 we note, however, that the area of maximum uplift velocity does not coincide with the region of the lithospheric step in thickness. In addition, the differences between the thick average lithosphere in model T10 and the much thinner average lithosphere in model 3 is manifest in the uplift velocities just as we saw for models 1 and T5. The thin model reflects spatial variations in the ice load much more than the smoothed thick model. The thicker model also changes the direction of the horizontal velocities on the coast of Norway and toward Sweden, making them more coherent with the observations. The difference between models 3 and T1 are due mainly to the thicker lithosphere over Sweden and Norway in the admittance model. It is likely that it is the thickness difference that produces the almost 180 degree rotation in the direction of the horizontal velocities off the coast of Norway, and the 90 degree rotation along the Scandinavian mountain chain. In Figure 6-5 we show the residual velocities and we see that the predicted uplift rates in models 3, T1 and T10 are too large.

Interestingly, the residual pattern is rather similar to that observed for the flat models, with areas of high negative misfit in central Norrland, and in the Lake Vänern area, and positive residuals to the south. This is in agreement with studies such as /Kaufmann and Wu 1998, 2002, Kaufmann et al. 2000, Wang and Wu 2006, Whitehouse et al. 2006/ that the pattern of uplift is determined by the ice model, whereas the magnitude of the uplift is determined by earth structure. In order to obtain a better fit to the data we constructed a model, T12, similar to model 3 but with a uniform viscosity of 1×10^{21} Pa s in the mantle.

We see in Figures 6-4 and 6-5 that model T12 predict vertical velocities more in agreement with the observations, but that the horizontal velocities now are completely misdirected in Norway. This is similar to what /Kaufmann et al. 2005/ found in Antarctica. Nevertheless, this model fits the data better than the previous three laterally varying models when the $\chi2$ is considered. It is likely that a thicker model, such as T10, with a half-space viscosity of approximately 1×10^{21} Pa s would fit the data even better.

6.2 Relative sea-level data

Since our modelling does not include the sea-level equation we cannot compute proper relative sea-levels (RSL). Sites that are well within the maximum extent of the former ice sheet are, however, mostly affected by solid Earth rebound and the eustatic sea-level change. We therefore use relative sea-level data collected in three areas around the Baltic; at the Ångerman river in northern Sweden, in northern Uppland in Sweden and in Olkiluoto in southwestern Finland, see Figure 6-1, to compare our models to. The data used here was collected from a number of sources and processed by /Whitehouse 2007/ and we use the eustatic sea-level data of /Fairbanks 1989, Bard et al. 1990/, Figure 6-6, to correct the vertical motion of the solid Earth, e.g. /Schotman et al. 2008, Whitehouse 2009/. An additional problem in comparing our modelled uplift to RSL data is that sea-levels in the Baltic are severely affected by the times when the Baltic was a lake. We cannot correct for this in our modelling, implying that the fit to the RSL data will also be affect. Our estimated RSL curves are only meant to be used as indicators that the ice and earth models reproduce the main features of the RSL-data.

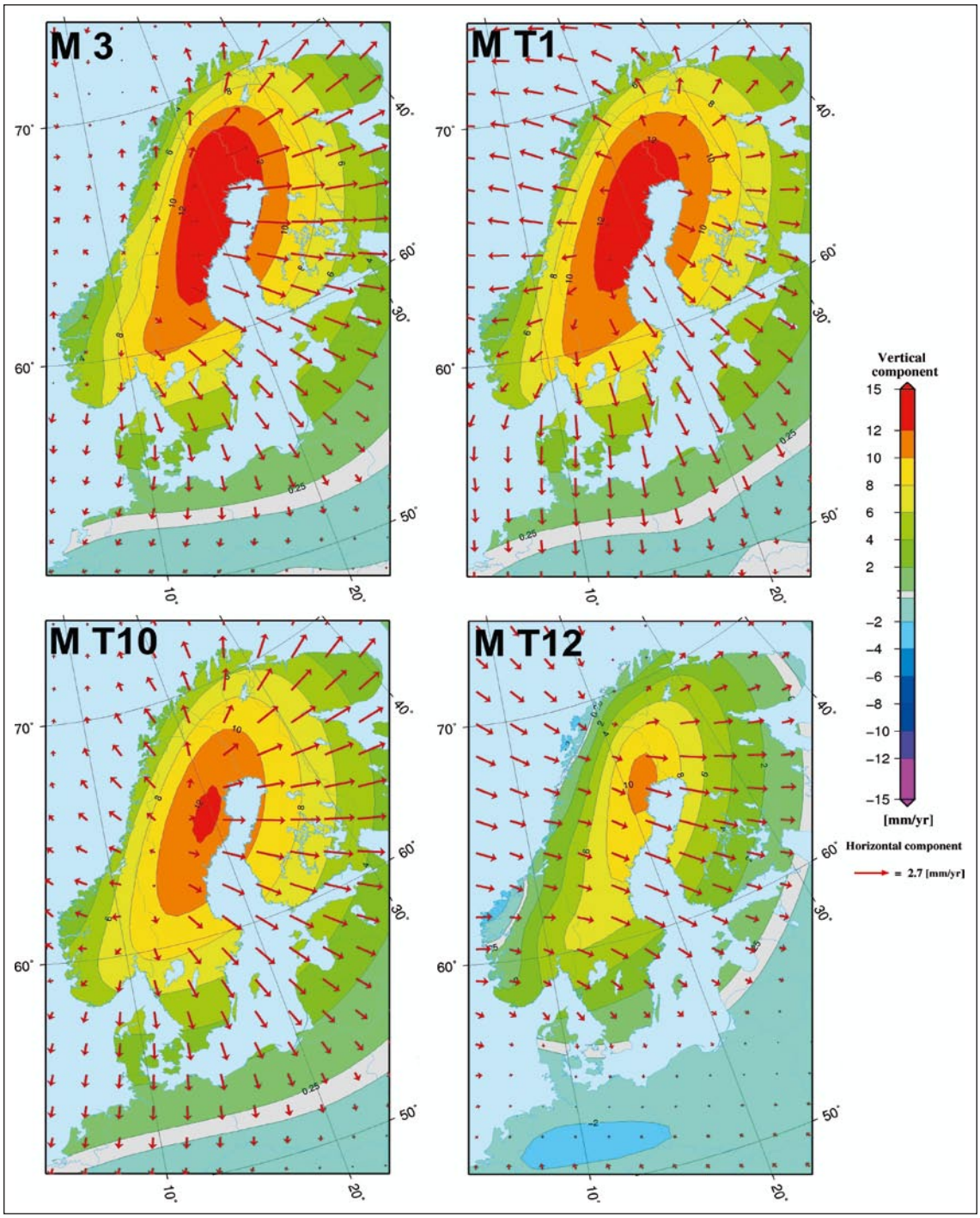

Figure 6-4. *Maps of horizontal and vertical velocities predicted from models 3, T1, T10 and T12, respectively. Colour contours show the vertical velocities, red arrows the horizontal velocities. The grey region represents ±0.25 mm/yr.*

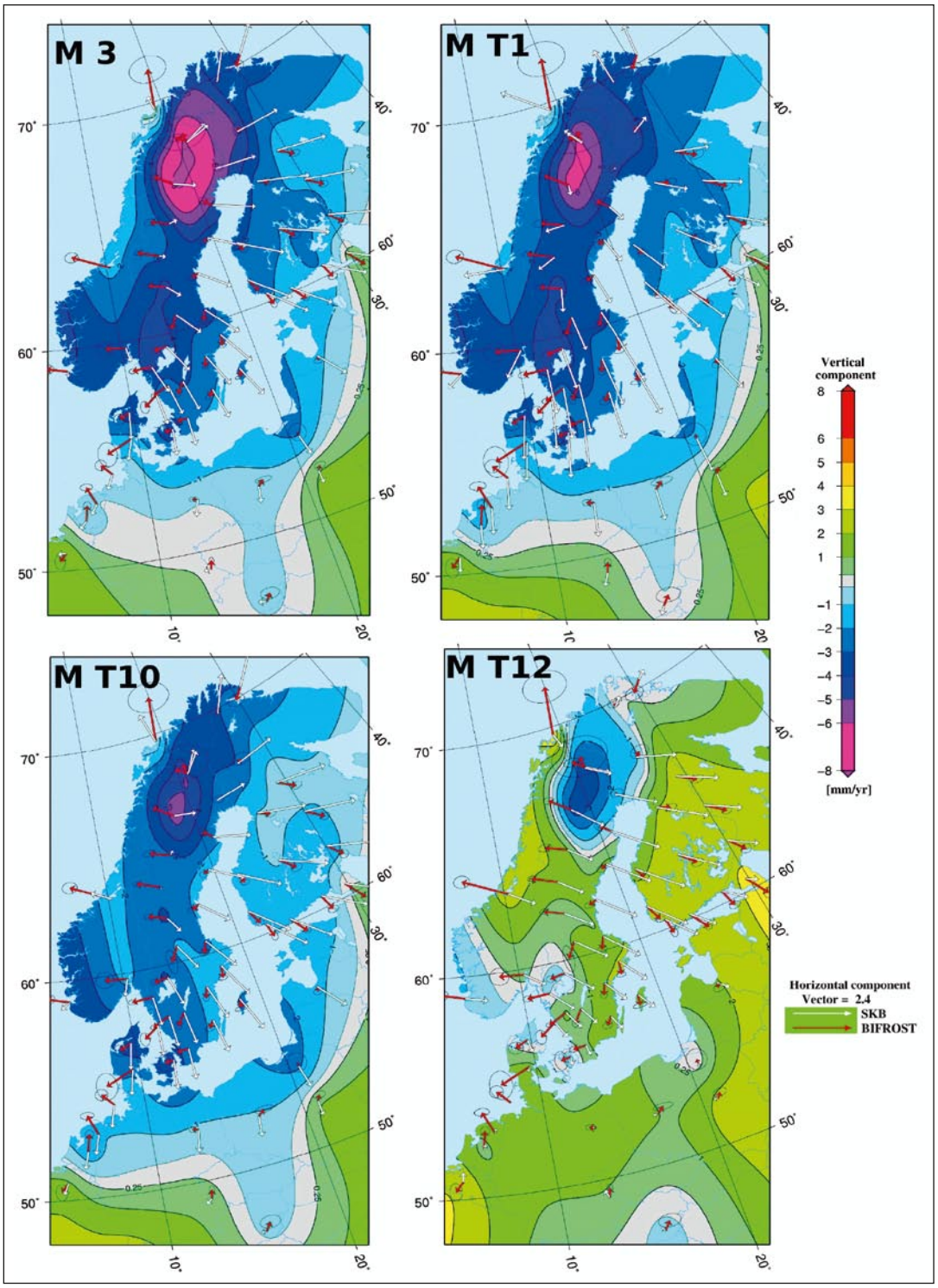

Figure 6-5. *Colour contours of differences in vertical velocities between the Bifrost data and models 3, T1, T10 and T12, respectively. The grey region represents ±0.25 mm/yr. Horizontal Bifrost velocities are shown with red arrows, model velocities with white arrows. The reference horizontal velocity vectors are in mm/yr.*

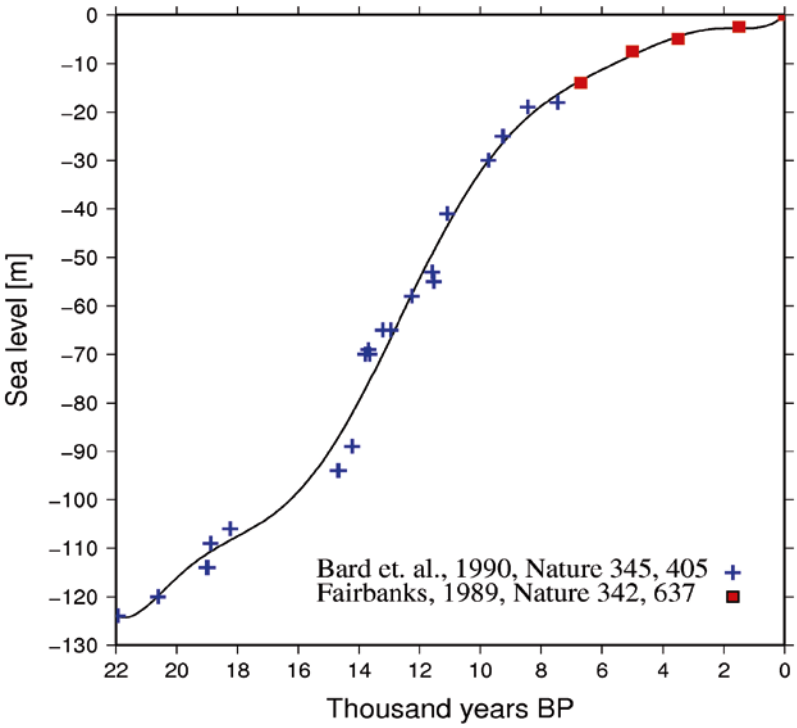

Figure 6-6. *Eustatic sea-level curve used to obtain relative sea-level curves from the solid Earth displacements in our models.*

Figure 6-7 shows the comparison of our modelled relative sea-levels and the data. At the Ångerman river, the models generally over-predict the sea-level at early times and have a slightly steeper gradient than the data. Remember though that the early data is affected by the Ancylus Lake stage. Model T9 has the best fit to the data of the horizontally stratified models, although it under-predicts the data at recent times. The variable thickness models have a worse fit to the data, with model T12 giving the best fit. Comparing to the northern Uppland data, our models again generally over-predict the sea-levels. The best fitting models are T9 and T12, for the two model types, although here the under-prediction at recent times is more pronounced. In the comparison to the Olkiluoto data, the same pattern emerges between our models and the data, i.e. general over-prediction of the sea-levels and the best fitting models, T9 and T12, slightly under-predicting the data at shorter times.

Although our models do not have an excellent fit to the sea-level indicators, we see that the misfit is not severe and that it is systematic enough that a thorough search of earth model space probably will improve the results. In addition, parts of the systematic misfit may be due to problems in the ice model.

Table 6-2. χ2 for the laterally varying earth models. North-south, east-west and vertical components, respectively plus the total χ2.

Model	North χ^2	East χ^2	Vertical χ^2	Total χ^2
3	247.1	202.3	192.4	213.9
T1	376.8	33.5	165	191.8
T10	238.8	140.9	84.2	154.6
T12	137.9	171.3	62.2	123.8

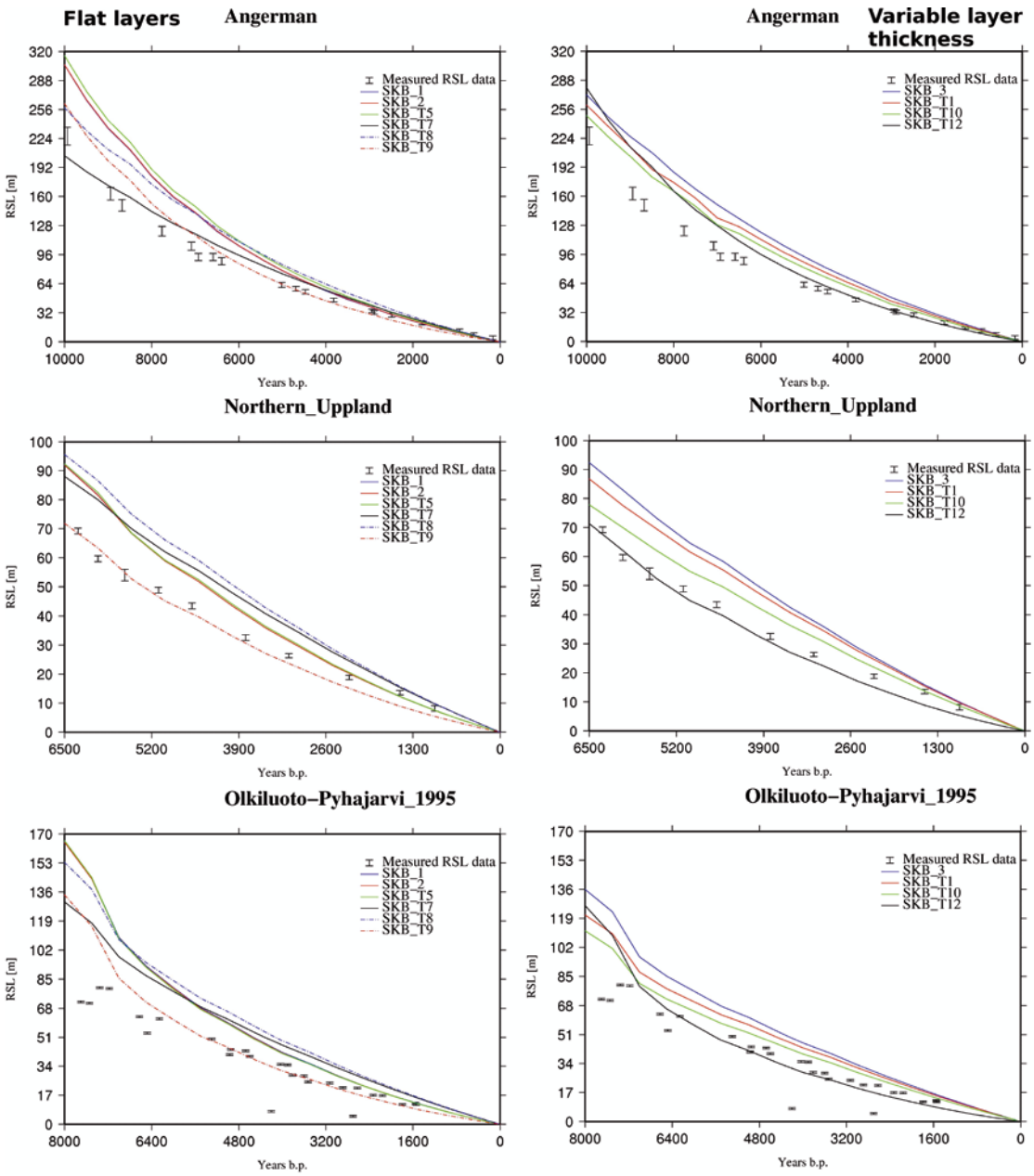

Figure 6-7. *Relative sea-level curves estimated from our models compared to data from the Ångerman river (upper row), northern Uppland (middle row) and Olkiluoto (lower row), see locations in upper left panel of Figure 6-1. The left column shows the results from the flat layered models, the right column shows results from models with laterally varying lithospheric thickness. Times are calibrated C-14 years, note that the time scales are different at the different sites.*

6.3 Summary

From the comparison of our model results to the GPS data we conclude that a mantle viscosity of approximately 1×10^{21} Pa s produces velocities that fit the data reasonably well. The structure of the lithosphere is less important for the fit to the GPS data and we saw that model 1 would be our model of choice if we only considered the GPS data. However, from a rock mechanics point of view the high Young's modulus close to the surface of the Earth in model 1 is unreasonable, and the Young's modulus of Model 2 is also higher than that measured close to the surface. Comparing to the sea-level data, we see that the lithospheric stratification does influence the results. There is a clear difference in fit between the T9 model and model 1. The horizontally stratified models generally fit the GPS data better than the models with lithospheric depth variation, which is mostly because of the poor fit to the horizontal velocities in the latter. For the sea-level results, there is less difference in fit between the flat and the laterally varying models. We will use model T9 as our preferred horizontally stratified model, and model T12 as the preferred model with laterally varying elastic thickness.

7 Glacially induced stress

In this section we will show snapshots from our models of the stress field induced by the ice sheet. Shown below are only the glacially induced stresses, we will add tectonic stresses in Section 9. The stress field will be presented as maps, depth profiles and temporal evolutions at particular sites. As we want to present comparisons between the different models in order to gain an understanding of how the stress field depends on earth model properties, we limit the map and depth profile presentation to two times; 18.5 kyr BP when the ice had its maximum extent and 10 kyr BP, just as the ice sheet has disappeared. For these times we show maps of the induced stress field in Fennoscandia at 2.5 km depth. We chose 2.5 km as it is the shallowest depth available in our large scale models, and therefore closest to the 500 m repository depth. As 2.5 km depth is too shallow to represent earthquake nucleation depths we will also show depth profiles along the NNE-SSW profile shown in Figure 4-1, which is the same profile investigated in /Lund 2006b/. In addition to these maps and depth profiles we will present time histories, extracted from the sub-models described in Section 5, of the stress evolution at 500 m depth at Forsmark, Oskarshamn and at 9.5 km depth at the Pärvie fault. The stress evolution at Forsmark and Oskarshamn is the first of the two main targets of this study.

We will show stress results for the horizontally stratified models 1, 2, T7, T8 and T9. We exclude model T5 as it has an elastic plate thickness which is smaller than that generally established for Fennoscandia, as discussed above. We also show stress maps for the laterally varying models 3, T10 and T12, excluding model T1 which is based on the free-air admittance model of /Perez-Gussinye et al. 2004, Perez-Gussinye and Watts 2005/. We do not include model T1 as /Perez-Gussinye et al. 2005/ indicate that depending on the modelled domain size, the admittance method may underestimate the elastic thickness for areas where the elastic thickness exceeds 30–40 km. For each of the eight models we will show maps of the magnitudes of the maximum (SHmax) and minimum (Shmin) horizontal stresses, the direction of the maximum horizontal stress and the maximum shear stress $(\sigma_1–\sigma_3)/2$. In the depth profiles we plot the SHmax magnitude and the maximum shear stress magnitude and in the temporal evolutions we show SHmax, Shmin and the vertical stress, Sv. As it is not always the case that one principal stress is vertical, we compute the proper SHmax /e.g. Lund and Townend 2007/ and do not use the nearest aligned principal stress. As is common in Earth Sciences we use the convention of compressive stress being positive.

7.1 Stress maps for the horizontally stratified models

In Figures 7-1 and 7-2 we show the magnitudes of the maximum and minimum glacially induced horizontal stresses at 18.5 kyr BP. We see that the general pattern of the stress fields is very similar for the different earth models, but that the magnitudes of the stress vary significantly. This is in agreement with observations of the behaviour of the displacement field referred to above /Kaufmann and Wu 1998, 2002, Whitehouse et al. 2006/. The region of high horizontal stresses basically follows the shape of the ice sheet, from northern Fennoscandia across south-central Sweden to southernmost Norway and then further across the North Sea to Great Britain. The magnitude of the maximum SHmax varies from over 70 MPa in model 1 to about 30 MPa in model T7, with the maximum values generally located in northern Sweden and Finland by the Bothnian Bay. The decrease in the maximum value is not followed by a similar decrease in the minimum value of SHmax, in fact model 1 also has the lowest SHmax magnitudes. This indicates that the range of stress magnitudes decreases from model 1 to the T models. We note that the minimum values of SHmax, outside of the glaciated area, are in fact negative which implies that both induced horizontal stresses are tensional. We see in Figures 7-1 and 7-2 that the regions of negative SHmax, coloured in blue, encircle the glaciated region (Figure 4-1) and correspond to the fore-bulge area. The minimum horizontal stress magnitudes follow a similar pattern to SHmax, with maximum magnitudes decreasing from model 1 to the T models while the range of magnitudes also decreases. The areas of tensional Shmin are more pronounced than than those of SHmax, outlining the fore-bulge region.

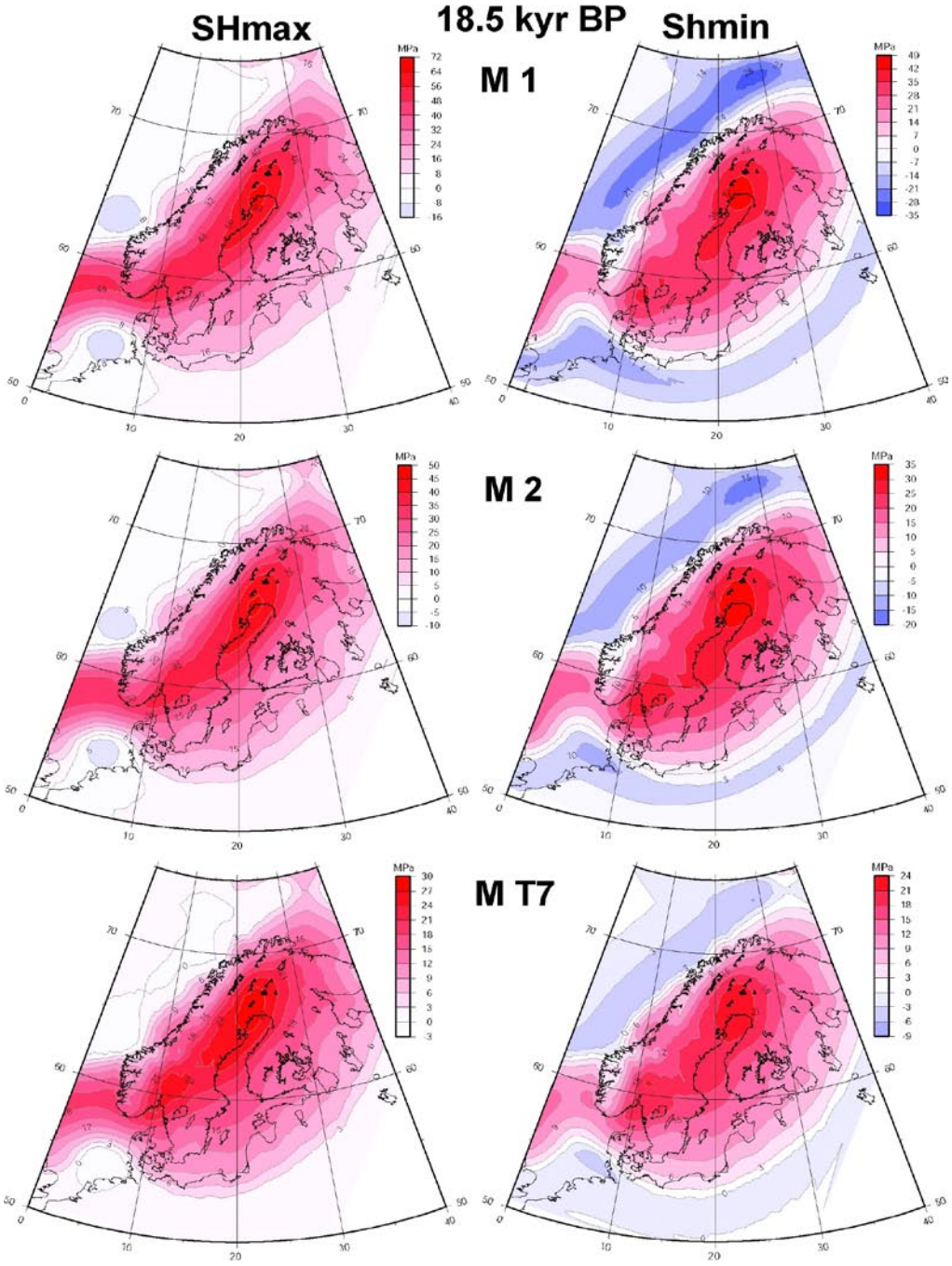

Figure 7-1. *Magnitudes of the maximum (SHmax), left column, and minimum (Shmin), right column, horizontal stress at 18.5 kyr BP and 2.5 km depth for models 1 (top), 2 (middle) and T7 (bottom). Note that the colour scale varies between models.*

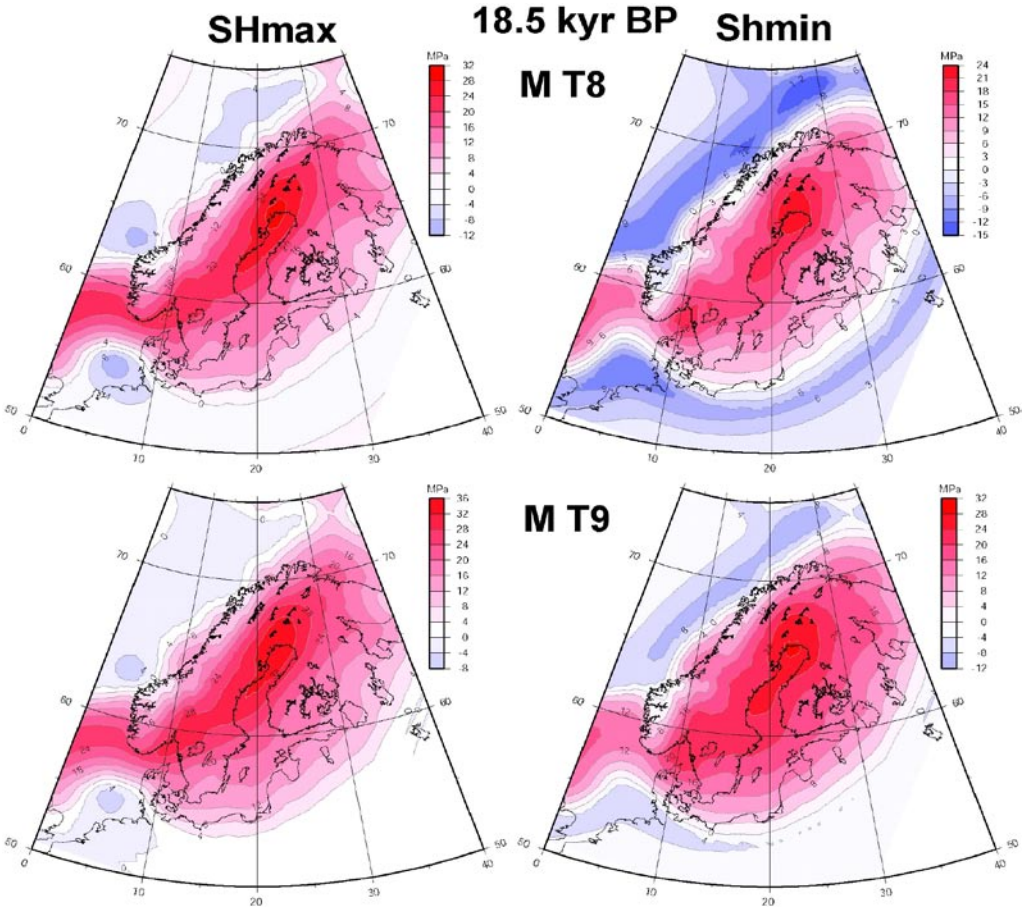

Figure 7-2. *Magnitudes of the maximum (SHmax), left column, and minimum (Shmin), right column, horizontal stress at 18.5 kyr BP and 2.5 km depth for models T8 (top) and T9 (bottom). Note that the colour scale varies between models.*

The decrease in maximum magnitudes corresponds to the decrease in Young's modulus from the stiff model 1, E = 192 GPa in the entire 100 km lithosphere, over model 2 which has E = 90 GPa in the upper 33 km but an average of 192 GPa in the lithosphere, to the T models which have E = 64 GPa in the upper layer and an average lithosphere modulus of 149 GPa (see Table 5-1). We note that the viscosity difference between models T7 (3×10^{21} Pa s) and T9 (1×10^{21} Pa s) produces a higher maximum stress and a larger range in stress magnitudes for the less viscous T9 model. Interestingly, model T8 (viscosity stratification at 670 km depth with upper mantle viscosity of 8×10^{20} Pa s) has a stress distribution that places it between models T7 and T9, despite of the lower viscosity in the upper mantle, which indicates that the stresses are in fact affected by the lower mantle. This is in agreement with the change in horizontal velocities observed between e.g. models T7 and T8, and is due to the different depth sensitivity of the kernels of e.g. the stress field and the vertical motion /e.g. Milne et al. 2004/.

Advancing the clock to 10 kyr BP we investigate the stress field just as the ice sheet has disappeared, in Figures 7-3 and 7-4. Again, we note the similarity of the stress pattern in all the models. We also see that the stress pattern at 10 kyr BP is similar to the pattern at 18.5 kyr BP, it is mostly the magnitudes that have changed. The stress magnitude distribution between the models at 10 kyr BP follows that at 18.5 kyr BP in that model 1 has the both the highest positive stress magnitudes and the lowest negative magnitudes. As expected stress magnitudes decrease during deglaciation and the equilibrium line, where the stresses are zero, move inward toward the former centre of glaciation in agreement with the expected fore-bulge migration. In model T8, however, the equilibrium line is almost stationary for Shmin and for SHmax it actually migrates outward in some areas. We note that at 10 kyr BP the largest Shmin have concentrated in northern Sweden and Finland north of the Bothnian Bay.

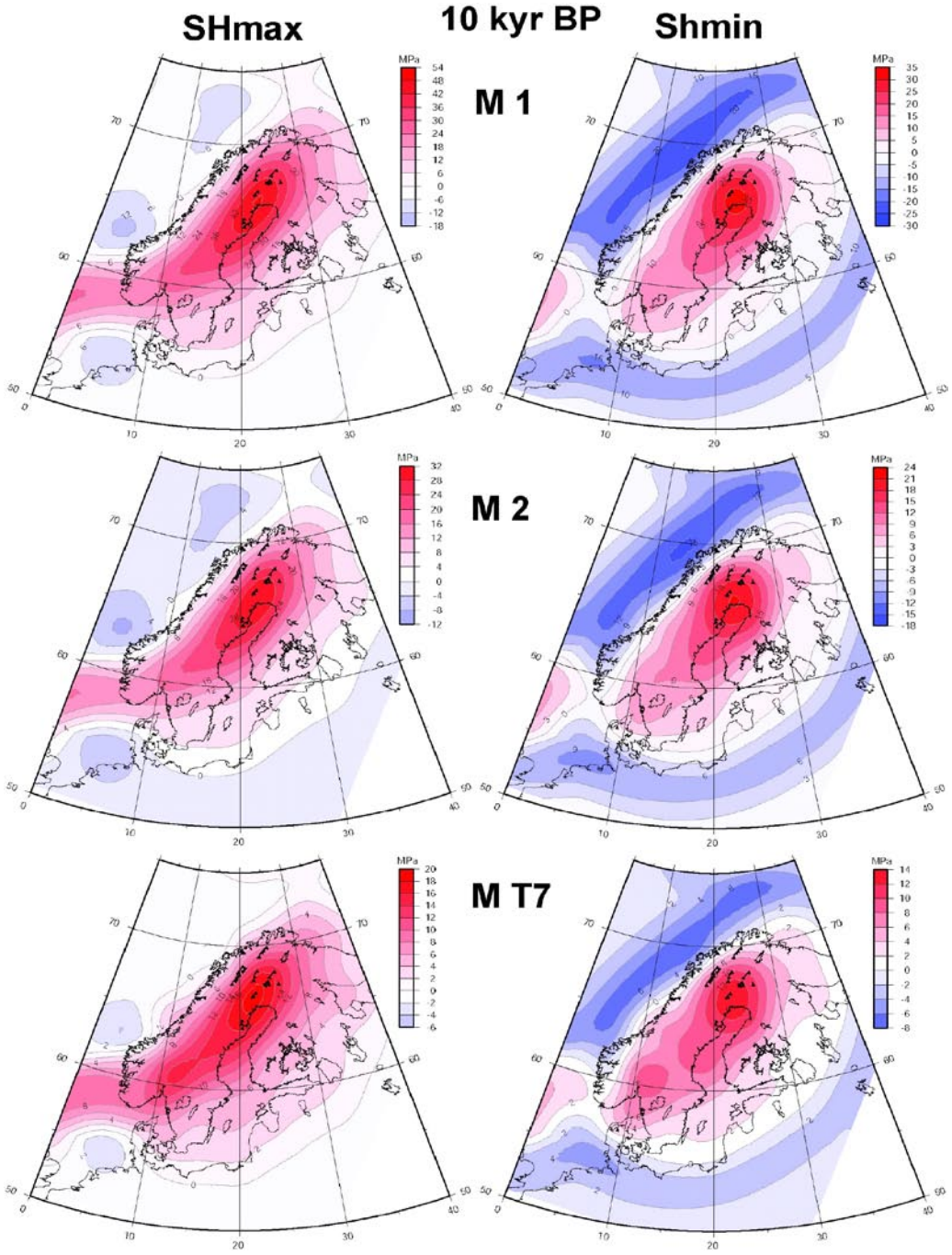

Figure 7-3. *Magnitudes of the maximum (SHmax), left column, and minimum (Shmin), right column, horizontal stress at 10 kyr BP and 2.5 km depth for models 1 (top), 2 (middle) and T7 (bottom). Note that the colour scale varies between models.*

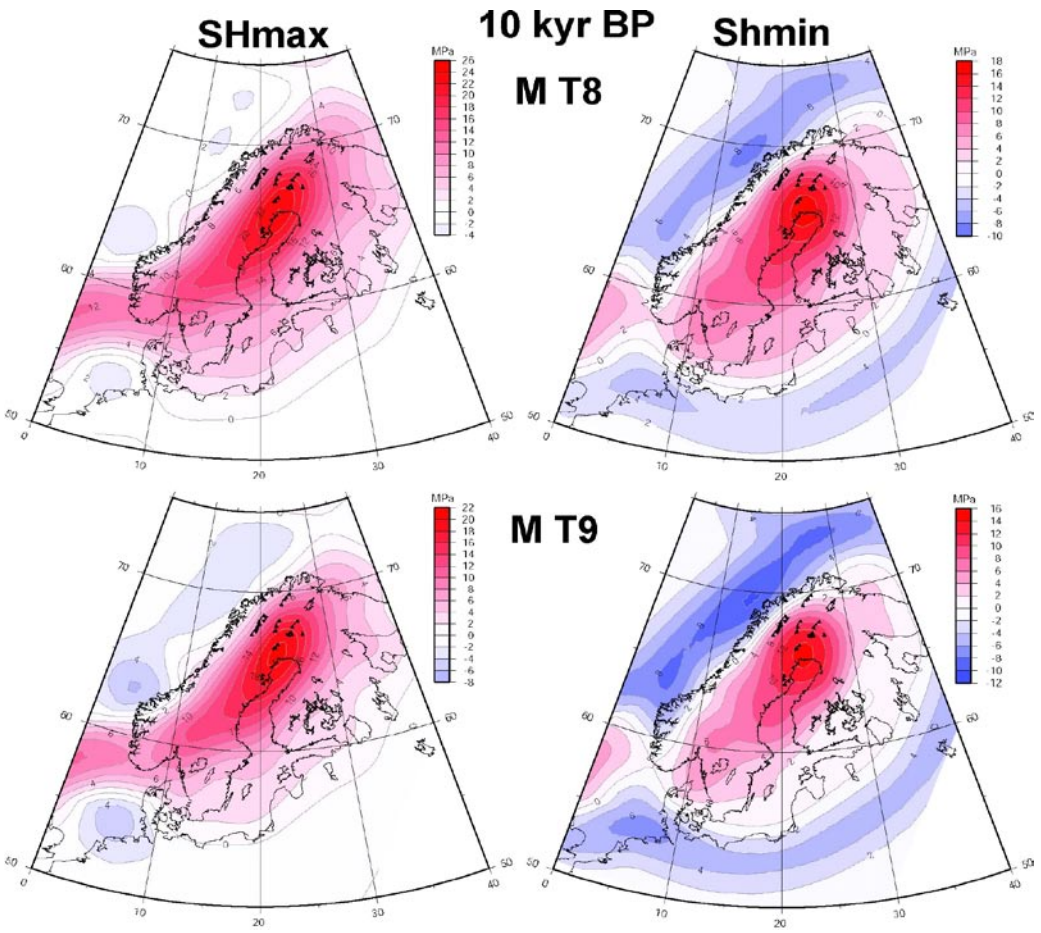

Figure 7-4. *Magnitudes of the maximum (SHmax), left column, and minimum (Shmin), right column, horizontal stress at 10 kyr BP and 2.5 km depth for models T8 (top) and T9 (bottom). Note that the colour scale varies between models.*

In Figures 7-5 to 7-8 we show the corresponding directions of SHmax and the maximum shear stresses for the two times and the five earth models. At 18.5kyr BP, the height of the glaciation, we see that SHmax is directed very much as we expect from the simple ellipsoidal model in Section 3, i.e. perpendicular to the long axis of the ice sheet under the ice and turning to encircle the ice sheet as we move toward the edge of the ice. Along the coast of Norway, where the ice sheet had a very steep edge the SHmax direction changes very close to the ice edge whereas to the east, where the ice was less steeply sloping (cf Figure 4-1) we note that the direction changes long before we reach the edge of the ice. The earlier SHmax rotation is probably also related to the fact that the ice to the south-east were of shorter duration than the ice over the mountain range. We note, in the 18.5 kyr figures, an interesting "channelling" effect of the stress directions in southern Sweden and Norway toward the Norwegian coast south of Trondheim, related to the very thin ice cover in that area. We also see that the SHmax directions rotate almost 90 degrees as we move from southwestern to southeastern Sweden. Just as in the ellipsoid model we see that as we move from the maximum glaciation to deglaciation, the region of stress direction perpendicular to the long axis of the ice decreases and the stresses rotate to encircle the centre of the former ice sheet. In northern Fennoscandia all models at both times predict SHmax directions approximately perpendicular to the strike of the large endglacial faults, in agreement with the direction of slip on the faults if the stress state was reverse.

The shear stress distributions in Figures 7-5 to 7-8 also show a general similarity to the simple ellipsoid model, with a high shear stress region stretching along the long-axis of the ice sheet surrounded by first regions of lower shear stress and then higher stress again. The high shear stress regions coincide with the areas of maximum flexure.

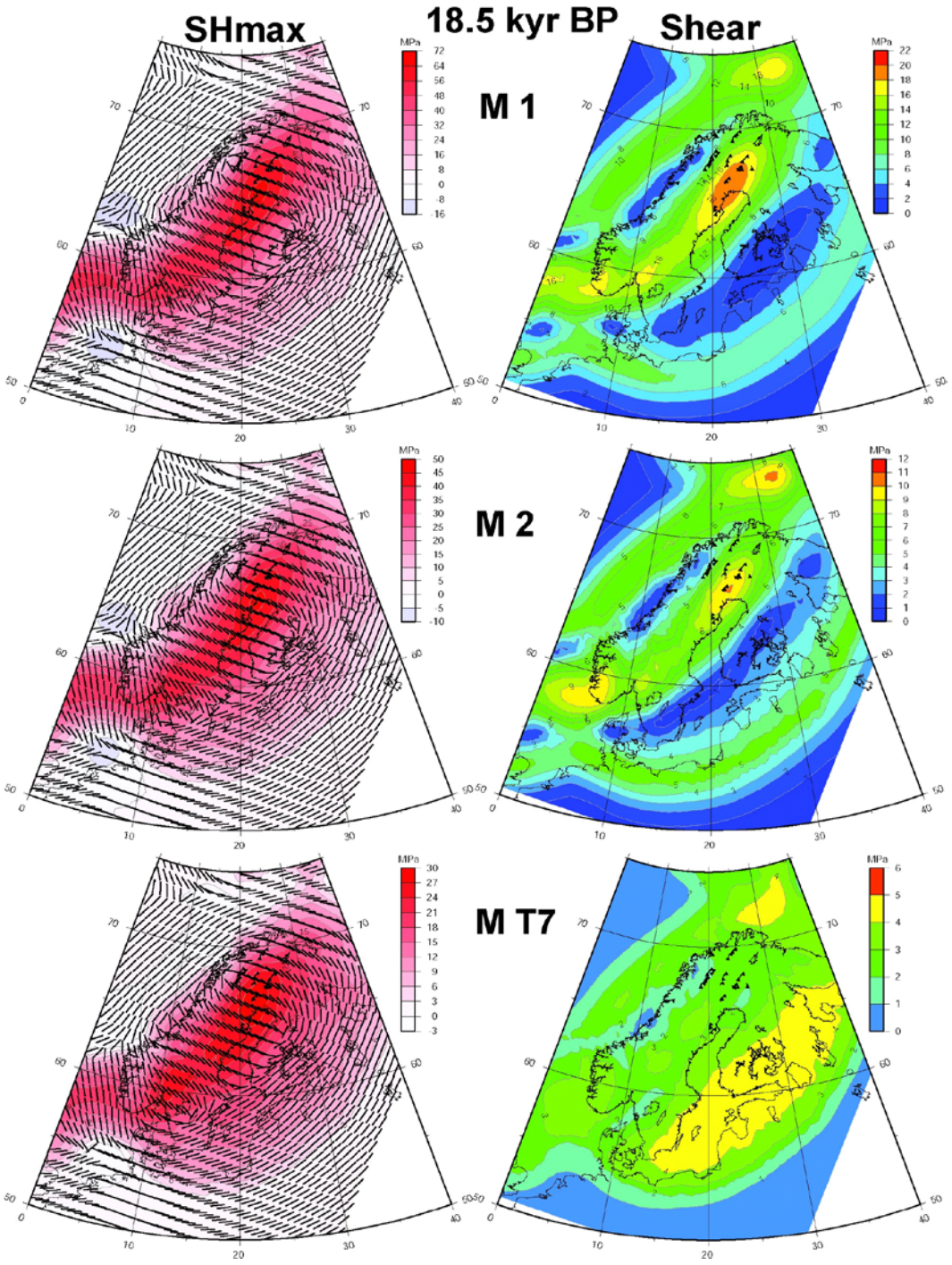

Figure 7-5. *Magnitude and direction of the maximum horizontal stress (SHmax), left column, and maximum shear stress, right column, at 18.5 kyr BP and 2.5 km depth for models 1 (top), 2 (middle) and T7 (bottom). Note that the colour scale varies between models.*

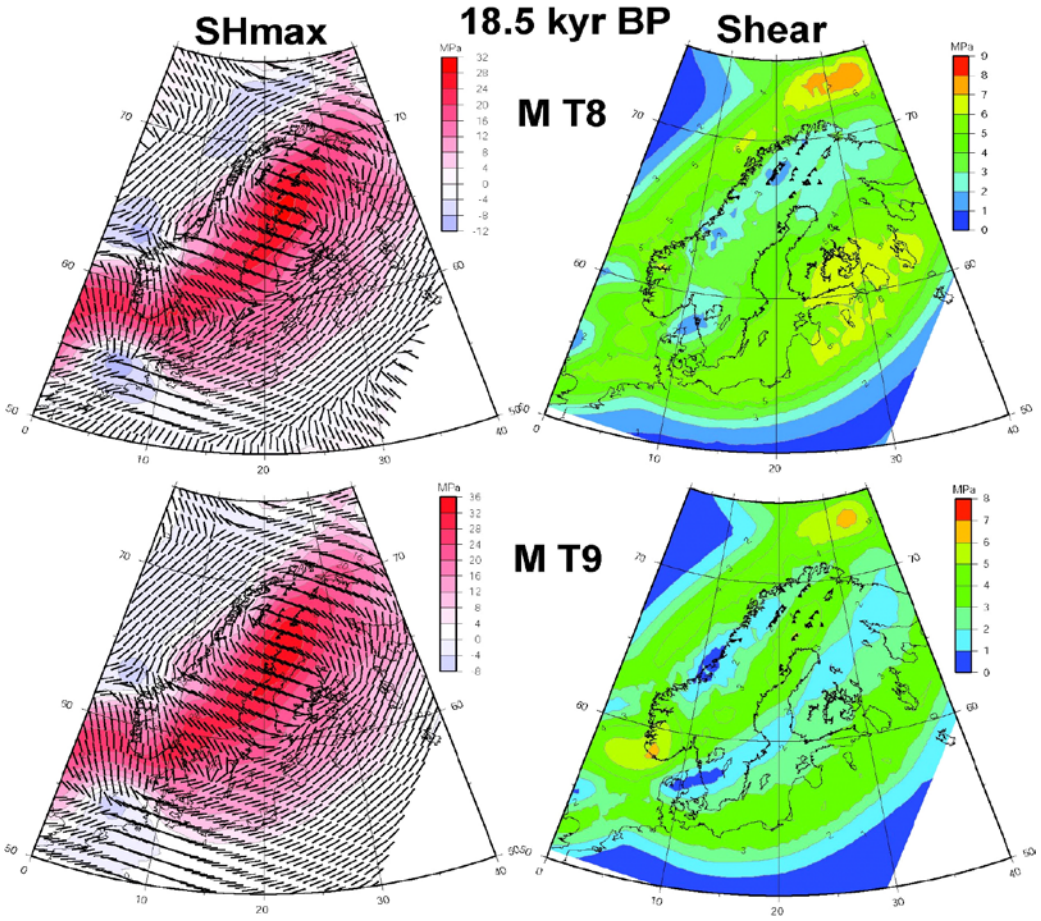

Figure 7-6. *Magnitude and direction of the maximum horizontal stress (SHmax), left column, and maximum shear stress, right column, at 18.5 kyr BP and 2.5 km depth for models T8 (top) and T9 (bottom). Note that the colour scale varies between models.*

At 18.5 kyr BP the stiffer models 1 and 2 show the highest shear stress in northern Sweden and Finland and also high stress north of the north coast of Fennoscandia and in south-western Norway. The softer models lack the central shear stress accumulation but do have high stress north of the north coast. Models T7 and T8 have areas of relatively high shear stress in large parts of southern Finland but those do not appear in model T9. The magnitude of the shear stresses are similar in the T models, larger in model 2 and much larger in model 1, as expected.

At the end of the glaciation, Figures 7-7 and 7-8, the induced shear stresses have increased, relatively, in all models and the maximum shear stresses are concentrated in northern Sweden and Finland, in general agreement with the region of large endglacial faults. A band of elevated shear stress stretches through north-central Sweden and then turns westward over southern Norway and out across the North Sea toward Great Britain. The maximum shear stress magnitudes are again similar in the T models and significantly higher in models 1 and 2.

7.1.1 Depth profiles of stress

Investigating how the stress varies at depth in the models we present depth profiles along the line shown in Figure 4-1, equivalent to the 2D model line of /Lund 2006b/. Here we will not present comparisons between 2D and 3D results, we refer to the ellipsoid example in Section 3 and the stress histories in /Lund 2006b/ and conclude that the 3D stresses are in general higher than the 2D stresses. The interested reader can compare the 3D stress histories for Forsmark and Oskarshamn in Section 7.3 below to those in /Lund 2006b/.

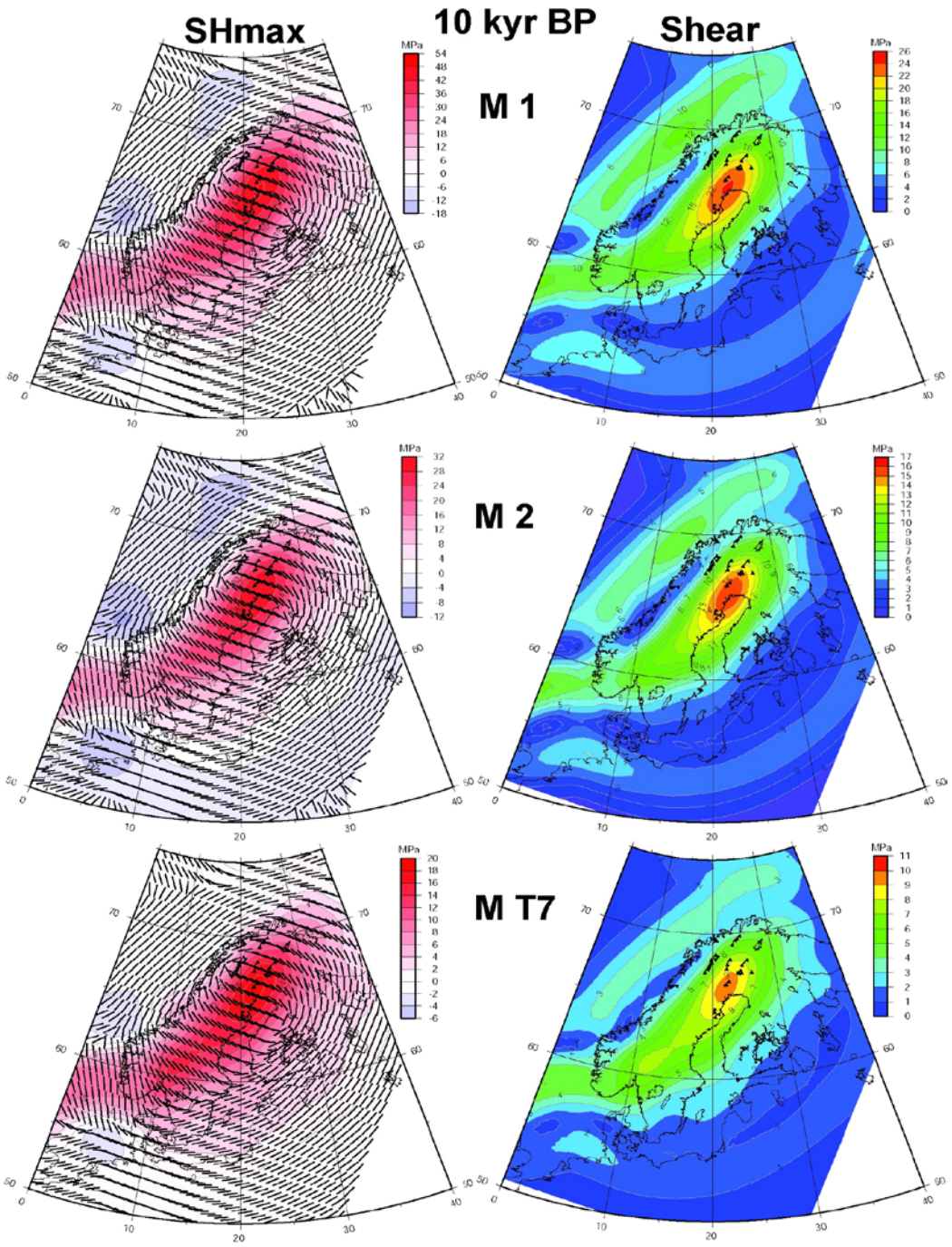

Figure 7-7. *Magnitude and direction of the maximum horizontal stress (SHmax), left column, and maximum shear stress, right column, at 10 kyr BP and 2.5 km depth for models 1 (top), 2 (middle) and T7 (bottom). Note that the colour scale varies between models.*

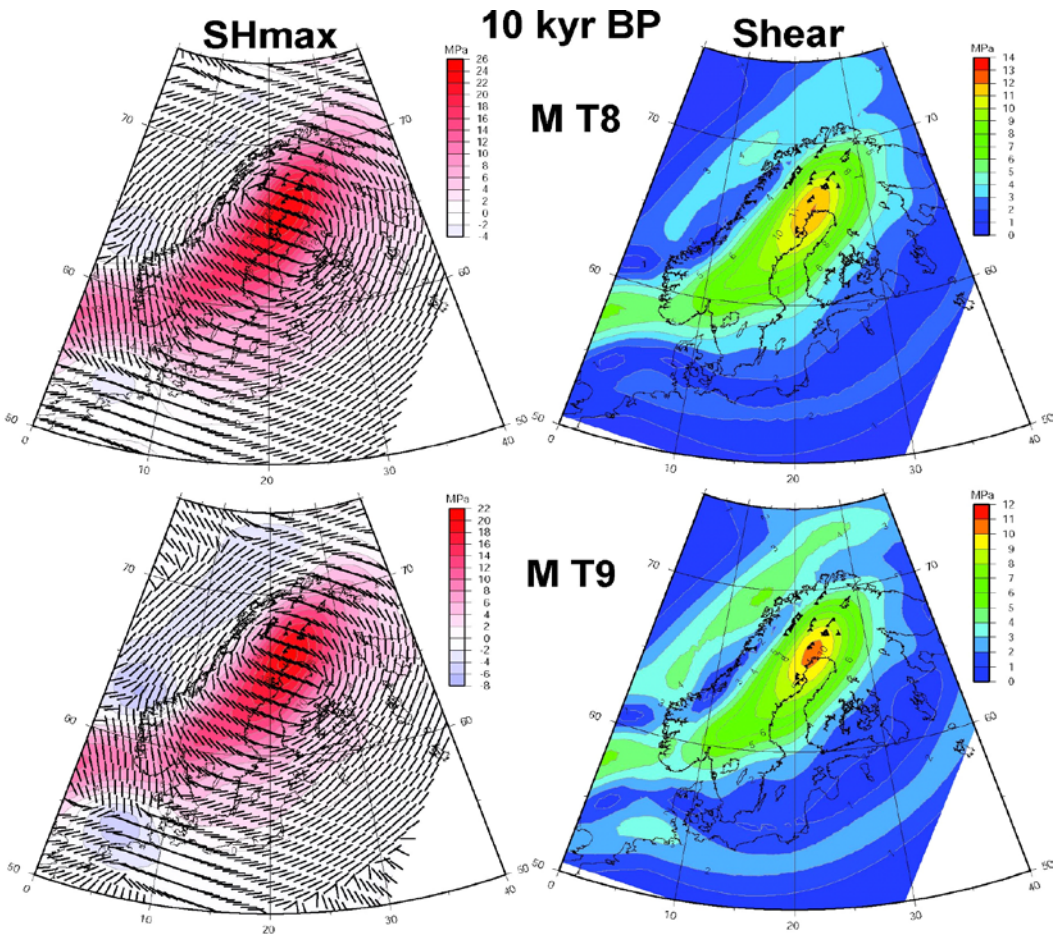

Figure 7-8. *Magnitude and direction of the maximum horizontal stress (SHmax), left column, and maximum shear stress, right column, at 10 kyr BP and 2.5 km depth for models T8 (top) and T9 (bottom). Note that the colour scale varies between models.*

In Figure 7-9 we present depth profiles down to 100 km depth of the maximum horizontal stress magnitudes at 18.5 kyr BP and 10 kyr BP for all the models. In agreement with the discussion above, model 1 has the highest stress magnitudes, and these are concentrated at the surface of the model under the centre of the ice load. The second smaller stress concentration to the north occurs below the Svalbard ice sheet. The layered models show stress concentrations both at the surface and in the upper part of the second layer, with the T models having the largest SHmax in the second layer, with similar magnitudes. At 10 kyr BP stresses have relaxed somewhat and concentrated under the former ice load. We note that SHmax is positive in most of the lithosphere along this profile.

In Figure 7-10 we show the corresponding shear stresses. In agreement with the maps above, model 1 has the highest shear stresses of the models near the surface. However, the softer models show a concentration of shear stress at the base of the lithosphere which is similar in magnitude to that of model 1, which is expected as a consequence of the stiffer material in the lower lithospheric layer. At 18.5 kyr BP the softer models generally have higher shear stress in the middle layer than in the upper layer. At 10 kyr BP shear stresses at the surface have increased, as we saw above. The highest shear stresses are however found in the upper part of the middle layer. The magnitudes are similar in all models, except for the higher values in model 1. Model T7 have the lowest shear stresses of these models. We note that the shear stress distributions are very model dependent, with shear stresses accumulating in the vicinity of material boundaries (the model elements are rather large at depth in the models, and since stresses are only evaluated at the centroids, the contoured maxima are further offset from the material boundaries than they should be).

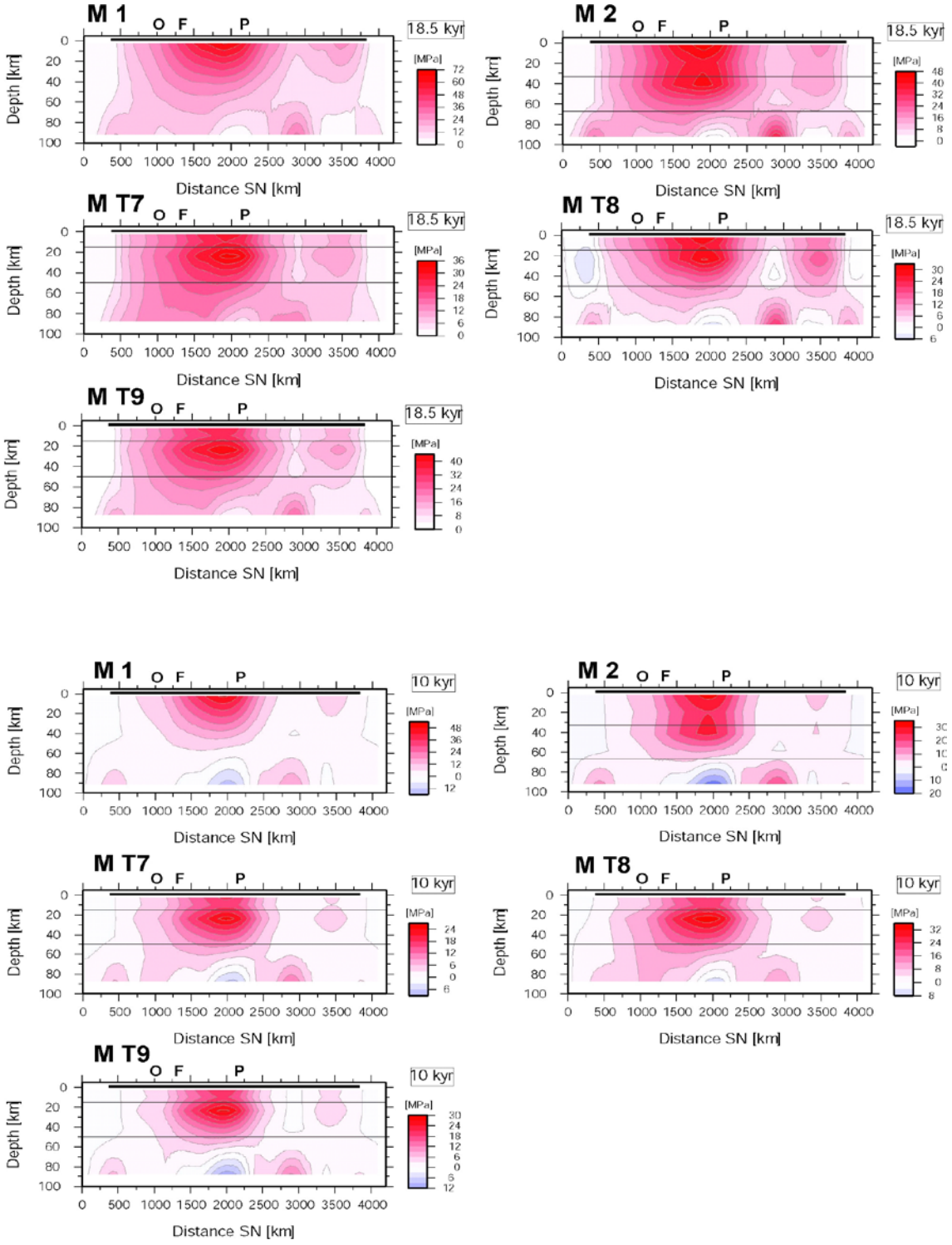

Figure 7-9. *Magnitude of the maximum horizontal stress (SHmax) along the NNE-SSW profile shown in Figure 4-1, which is the same as the profile in /Lund 2006b/. Upper three rows: 18.5 kyr BP, lower three rows: 10 kyr BP. Models 1, 2, T7, T8 and T9 as indicated in the figure. Locations of Oskarshamn (O), Forsmark (F) and the region with endglacial faults (P) are shown on the profiles. Note that the colour scale varies between models. Horizontal black lines show material boundaries.*

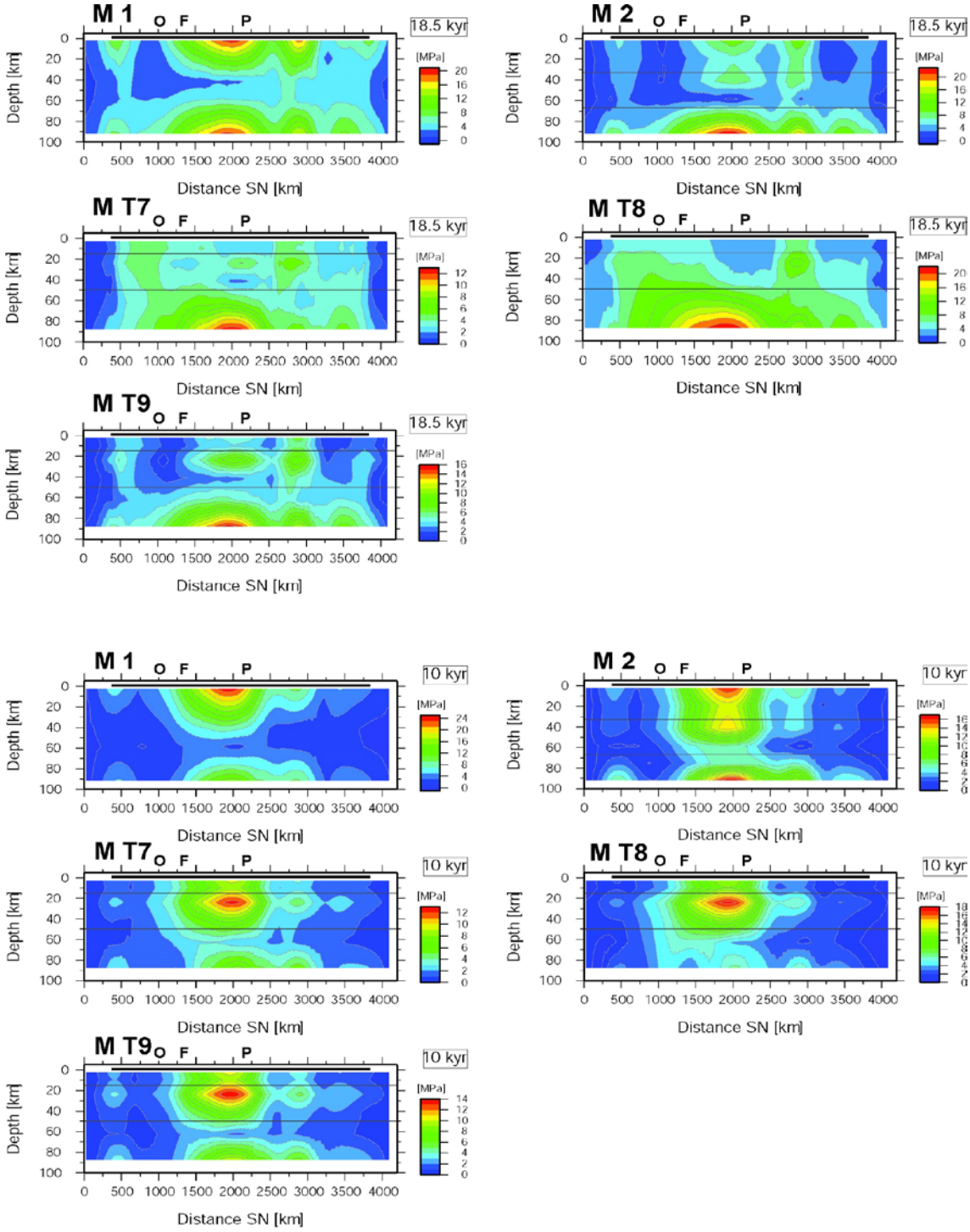

Figure 7-10. *Maximum shear stress along the NNE-SSW profile shown in Figure 4-1, which is the same as the profile in /Lund 2006b/. Upper three rows: 18.5 kyr BP, lower three rows: 10 kyr BP. Models 1, 2, T7, T8 and T9 as indicated in the figure. Locations of Oskarshamn (O), Forsmark (F) and the region with endglacial faults (P) are shown on the profiles. Note that the colour scale varies between models. Horizontal black lines show material boundaries.*

7.2 Stress maps for models with laterally varying lithosphere thickness

In this section we investigate the response of three of the models with laterally varying lithospheric thickness, models 3, T10 and T12 (see Table 5-2). Model 3 is based on the elastic thickness of /Perez-Gussinye et al. 2004, Perez-Gussinye and Watts 2005/ with an adjusted average thickness in the modelled region of 100 km. Model T10 is similar but with the average thickness now adjusted to 170 km. Model T12 is similar to model 3 but has a uniform viscosity of 1×10^{21} Pa s in the sublithospheric mantle, instead of the two-layered viscosity (8×10^{20} Pa s above 670 km and 1×10^{22} Pa s below) of model 3. All three models have a three layered lithosphere with elastic properties similar to the softer T models above. The figures presented here show the stress field at 2.5 km depth, as above.

In Figure 7-11 we show maps of SHmax and Shmin at 18.5 kyr BP. The pattern of the stress field is similar in the three models, but we note that model T10 has fewer irregularities in the stress field along the Norwegian coast than models 3 and T12. As was discussed in Section 6, this is due to the thin lithosphere in western Norway and off the coast, in models 3 and T12 the elastic layer is only about 30-40 km thick in this area, which allows variations in the ice cover to be reflected in the stress field. The magnitude of the stress field is similar in all three models, with model T10 having the highest SHmax magnitudes. Compared to the horizontally stratified T models above we see that the shape and magnitude of the stress field is similar over all, but that models 3 and T12 differ with their high frequency undulations in the field on the Norwegian coast. We note that the sharp NNE-SSW change in lithospheric thickness (Figure 5-3) is not reflected as a clear discontinuity in the stress field. Moving on in time to 10 kyr BP, Figure 7-12, we again have relatively rapid stress variations along the Norwegian coast in models 3 and T12, but the concentration of high stress in northern Sweden and Finland is similar for both the laterally varying and flat models. We see in the Shmin maps that some areas in southwestern Norway have significant tensional stress induced by the deglaciation.

Comparing the stress direction maps at 18.5 kyr BP in Figure 7-13 we see how the stress magnitude undulations in the thin models above are also reflected in the stress directions. There is significant inhomogeneity in the field along the Norwegian coast and in south-central Norway in models 3 and T12. Compared to the flat models we clearly see a westward shift in the area of homogeneous east-west directed stress under the central stress maximum. This area is also slightly larger than in the flat T models. We interpret this as depending on the NNE-SSW striking rapid thinning of the lithosphere. At 10 kyr BP, Figure 7-14, this difference between flat and varying models become even clearer, with larger and more NNE-SSW elongated areas of homogeneous stress direction under the central stress anomaly. Also, we note that the inhomogeneities along the Norwegian coast persist through deglaciation.

The shear stress distributions in Figure 7-13, at 18.5 kyr BP, are similar to the flat models both in pattern and magnitude. There distribution of shear stress is not very well defined, just as we saw above, but the shear stress concentration off the north coast of Norway persists in all three models. Model 3 shows a strong stress concentration in southwestern Norway, which is much less pronounced in the similarly thin T12 model. At 10 kyr BP, Figure 7-14, the shear stresses have concentrated to northern Sweden and Finland, as in the flat models. The band of elevated shear stress off the west coast of Norway is not stronger or larger than in the flat models, indicating that this is not significantly influenced by lithosphere thinning. Overall, shear stress magnitudes in the laterally varying models are similar to those in the flat T models.

7.2.1 Depth profiles of stress

Here we present depth profiles through the laterally varying models 3, T10 and T12 along the NNE-SSW line shown in Figure 4-1. This is the same line as used for the depth profiles in Section 7.1.1 above. In the figures below we have only included data from the lithosphere, the sublithospheric mantle is shown in grey. Figure 7-15 shows the magnitude of SHmax. We see that just as in Figure 7-9, the maximum stresses accumulate in the upper part of the second layer, below the centre of the load. The high stress concentration follows layer two in depth, not penetrating significantly into layer three. We note that in the upper approximately 20 km, there are no major differences between the flat and the laterally varying horizontal layering of the earth models. The magnitudes of the stresses are similar to those of the flat T models, except that these laterally varying models exhibit smaller areas and lower magnitudes of induced tensional stress at 10 kyr BP.

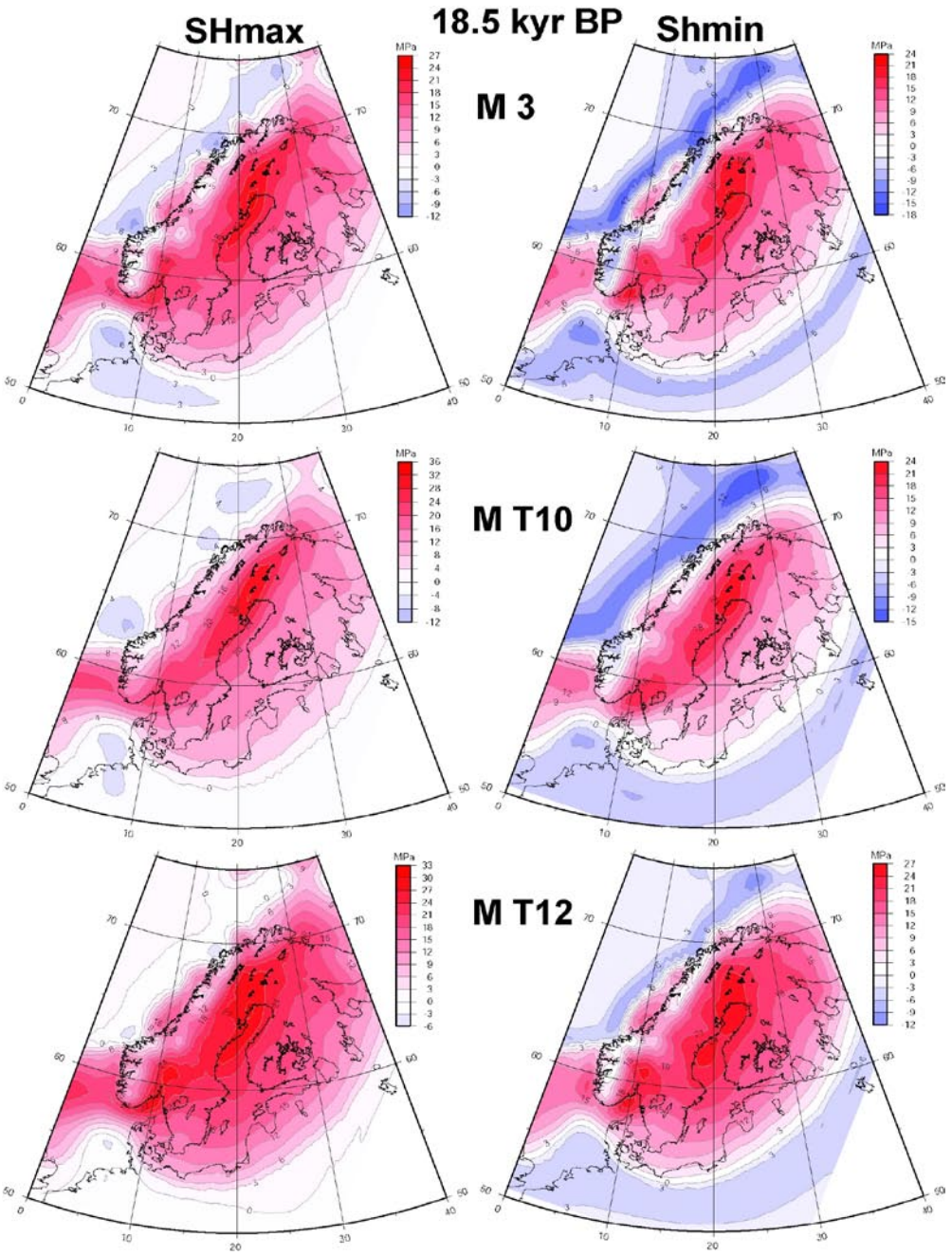

Figure 7-11. *Magnitudes of the maximum (SHmax), left column, and minimum (Shmin), right column, horizontal stress at 18.5 kyr BP and 2.5 km depth for models 3 (top), T10 (middle) and T12 (bottom). Note that the colour scale varies between models.*

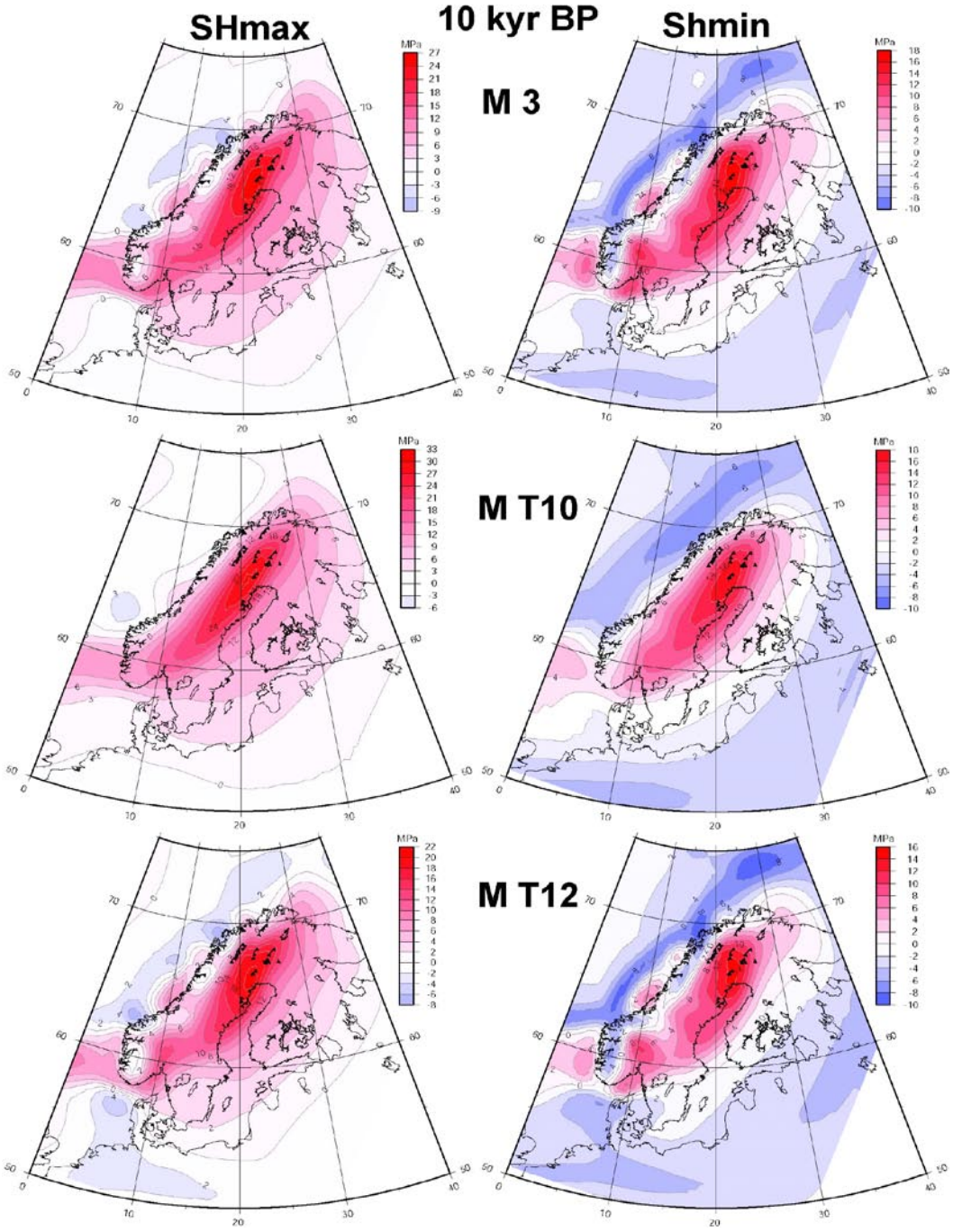

Figure 7-12. *Magnitudes of the maximum (SHmax), left column, and minimum (Shmin), right column, horizontal stress at 10 kyr BP and 2.5 km depth for models 3 (top), T10 (middle) and T12 (bottom). Note that the colour scale varies between models.*

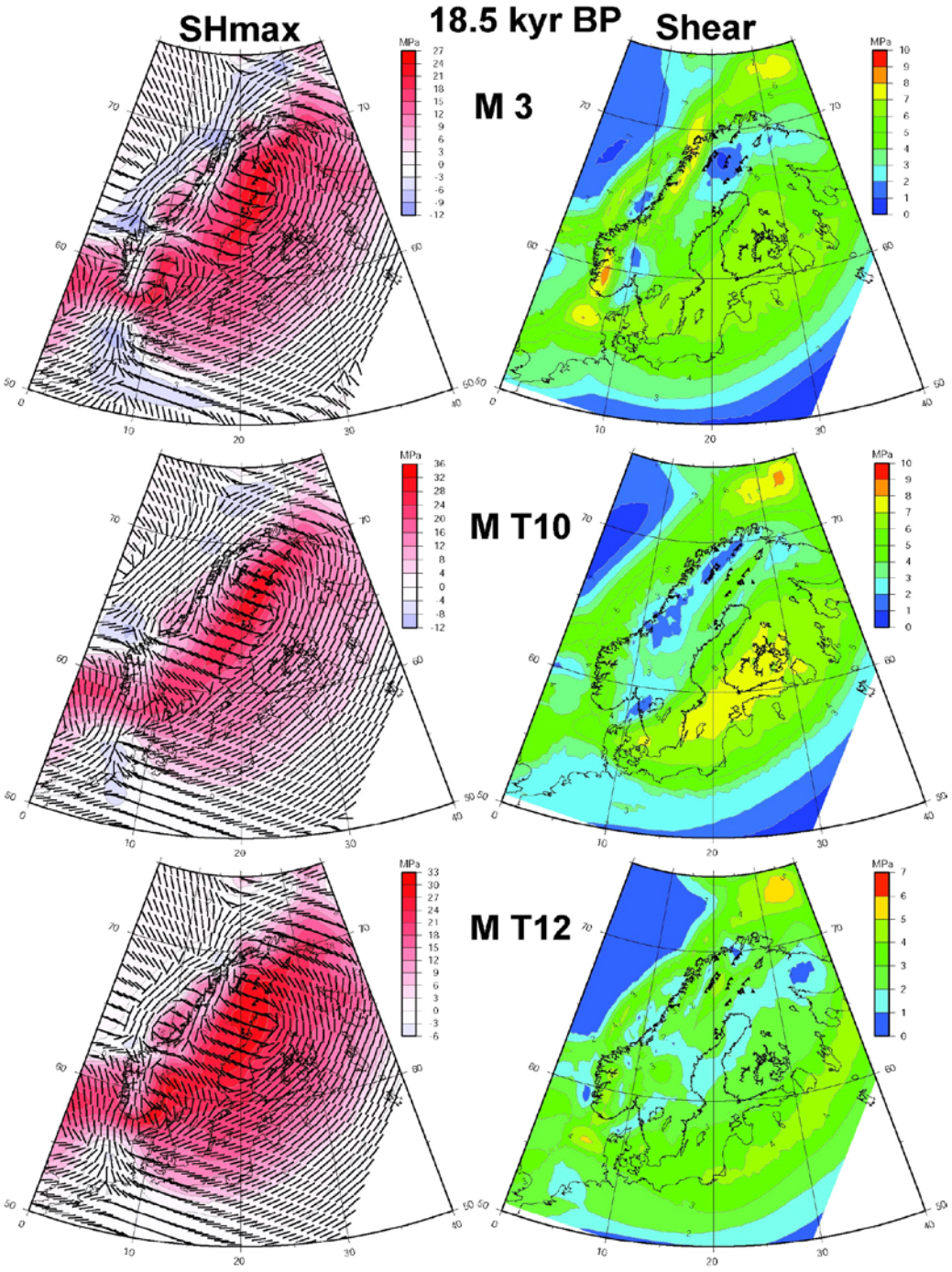

Figure 7-13. *Magnitude and direction of the maximum horizontal stress (SHmax), left column, and maximum shear stress, right column, at 18.5 kyr BP and 2.5 km depth for models 3 (top), T10 (middle) and T12 (bottom). Note that the colour scale varies between models.*

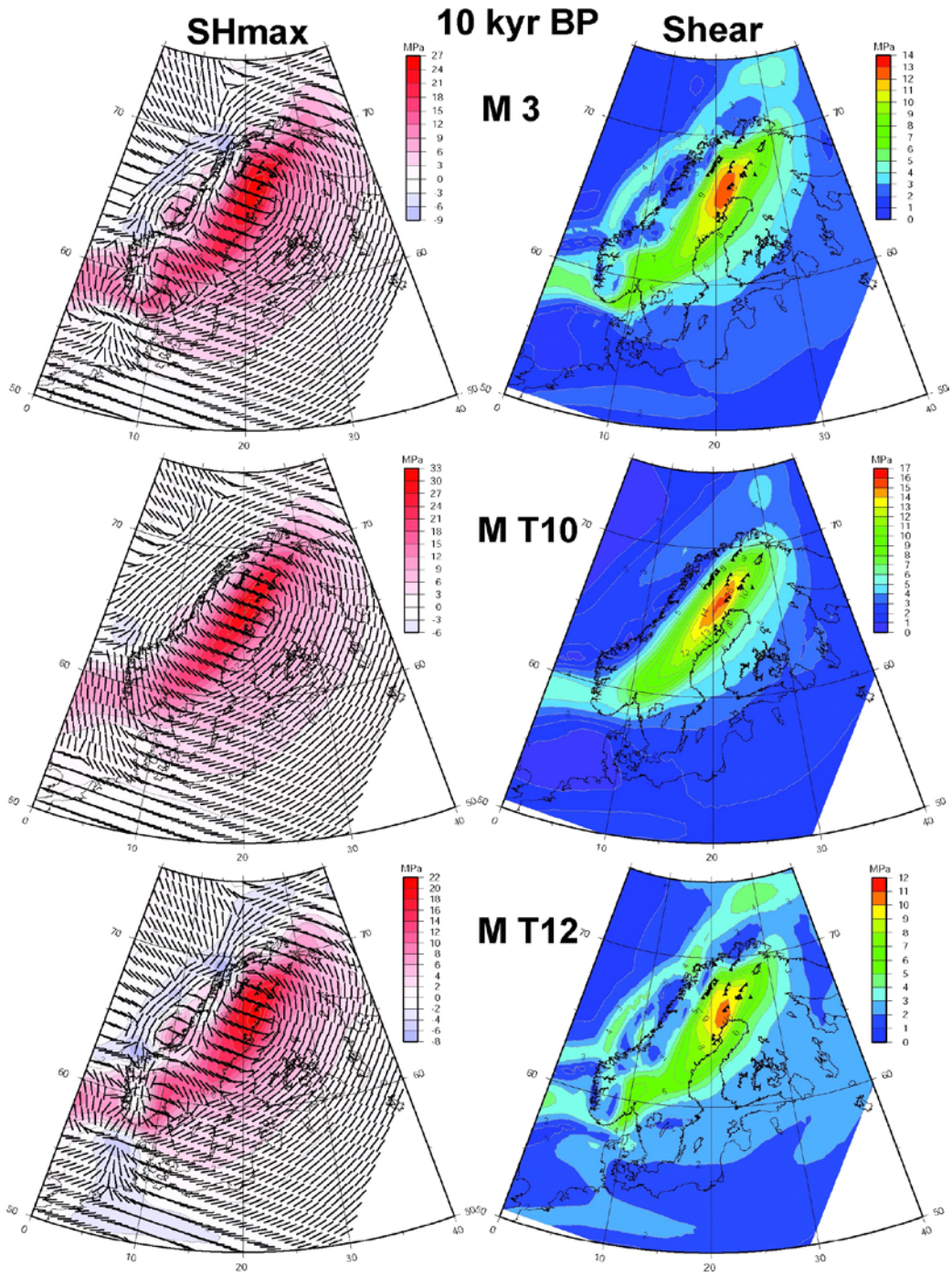

Figure 7-14. *Magnitude and direction of the maximum horizontal stress (SHmax), left column, and maximum shear stress, right column, at 10 kyr BP and 2.5 km depth for models 3 (top), T10 (middle) and T12 (bottom). Note that the colour scale varies between models.*

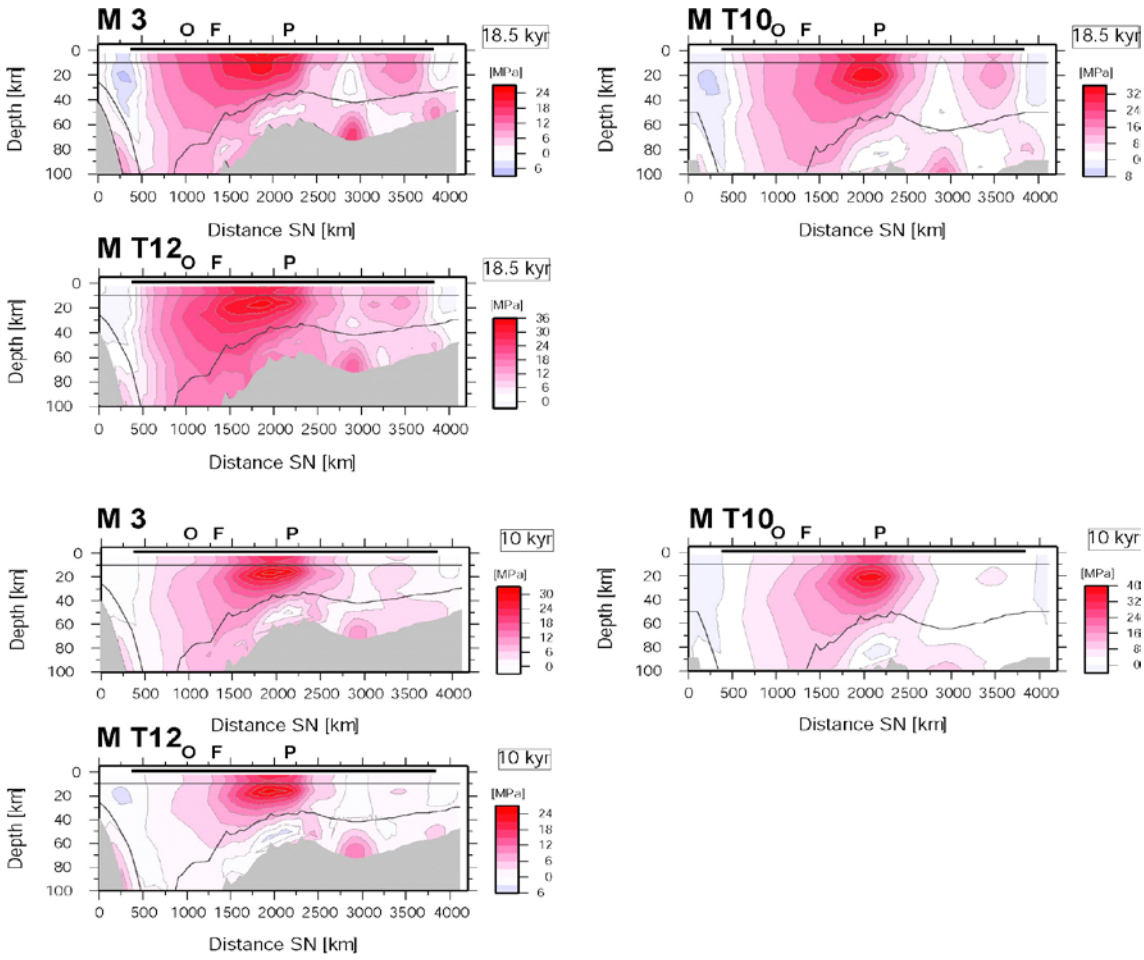

Figure 7-15. *Magnitude of the maximum horizontal stress (SHmax) along the NNE-SSW profile shown in Figure 4-1, which is the same as the profile in /Lund 2006b/. Upper three rows: 18.5 kyr BP, lower three rows: 10 kyr BP. Models 3, T10, T12 as indicated in the figure. Locations of Oskarshamn (O), Forsmark (F) and the region with endglacial faults (P) are shown on the profiles. Note that the colour scale varies between models. The black lines show material boundaries.*

In Figure 7-16 we show the maximum shear stress profiles. Similar to the flat models in Figure 7-10, at 18.5 kyr BP shear stress accumulates in the third layer in the lowermost lithosphere. The shear stresses in the laterally varying models are however significantly larger than in the flat layered T models. This depends on the interaction of the thickening of the lithosphere with the glacially induced flexure. In the uppermost lithosphere the models have similarly patterns and magnitudes of shear stress. At 10 kyr BP the laterally varying models again show similar patterns as the flat models, with shear stresses accumulating in the upper part of layer two, below the former centre of the ice load.

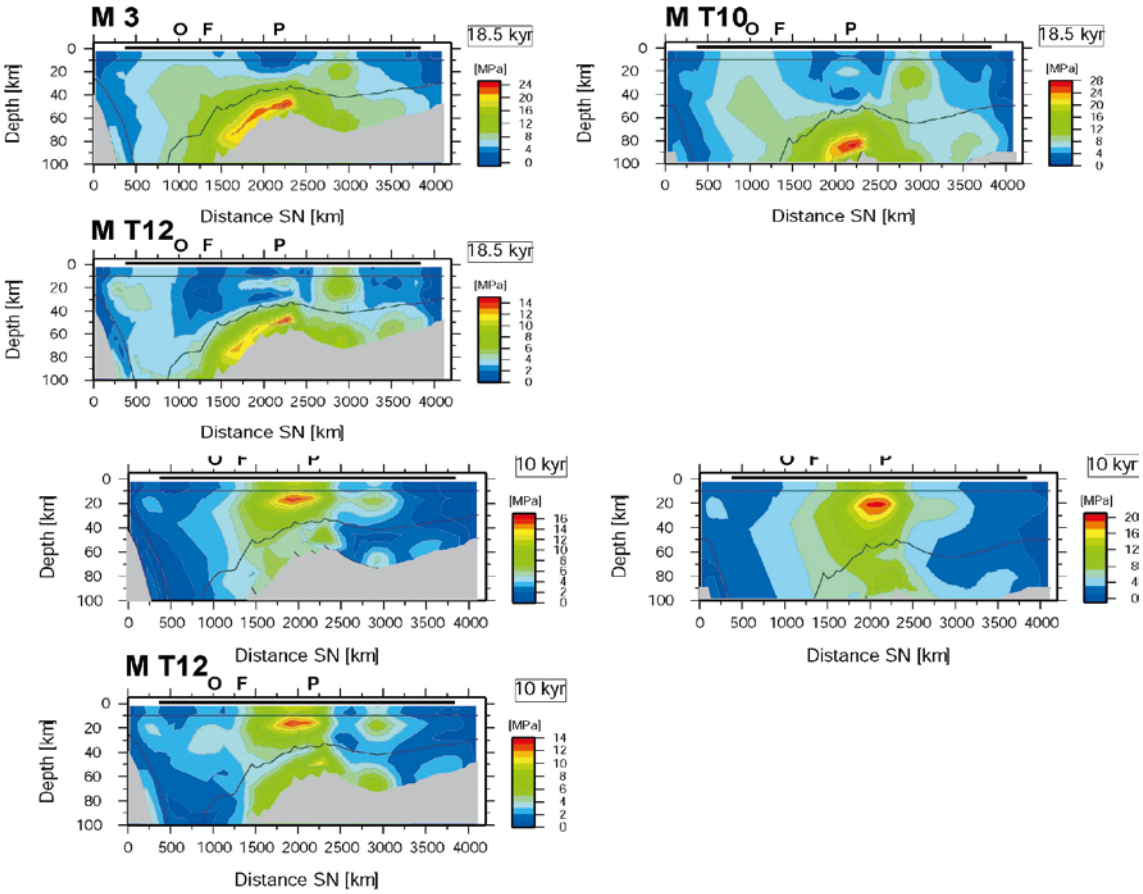

Figure 7-16. *Maximum shear stress along the NNE-SSW profile shown in Figure 4-1, which is the same as the profile in /Lund 2006b/. Upper three rows: 18.5 kyr BP, lower three rows: 10 kyr BP. Models 3, T10, T12 as indicated in the figure. Locations of Oskarshamn (O), Forsmark (F) and the region with endglacial faults (P) are shown on the profiles. Note that the colour scale varies between models. The black lines show material boundaries.*

7.3 Temporal stress variations

Using the sub-models discussed in Section 5 we model the stresses at higher spatial resolution in the subregions of the large scale model shown in Figure 5-2. In this section we present the full temporal stress evolution for Forsmark and Oskarshamn at 500 m depth, and for the central Pärvie fault at 9.5 km depth, which is more appropriate for earthquake nucleation. The Forsmark and Oskarshamn stress time histories here can be directly compared to the 2D simulations in /Lund 2006b/.

Figure 7-17 shows the stress histories for SHmax, Shmin and the vertical stress (Sv) at 500 m depth in Forsmark for all the earth models discussed above. We see that Sv is identical for all models, it is simply reflecting the ice load and the blue curve can be used as a proxy for the thickness of the ice sheet through time. We see very clearly the two stages of ice coverage over Forsmark, separated by almost 25,000 years of ice free conditions. The horizontal stresses follow the build-up of the ice, and we note that Shmin becomes negative before and during the initial phase of glaciation. This is due to the flexure of the lithosphere north and west of Forsmark, where the ice grows earlier and places Forsmark in the peripheral bulge. As expected, models 1 and 2 produce the highest stresses due to their stiff lithospheres. Flat layered model T9 has higher horizontal stresses than T7 and T8, where the flexural stresses only exceed the vertical stress after deglaciation. However, models T7 and T8 have higher differential stress than model T9. We also note how the flexural stresses in the more viscous models T7 and T8 decay slower after deglaciation than those in model T9. The models with laterally varying lithosphere thickness produce maximum stresses that are similar to those in the flat T models, however, in these models Shmin remains negative for large parts of the time between the glaciated periods.

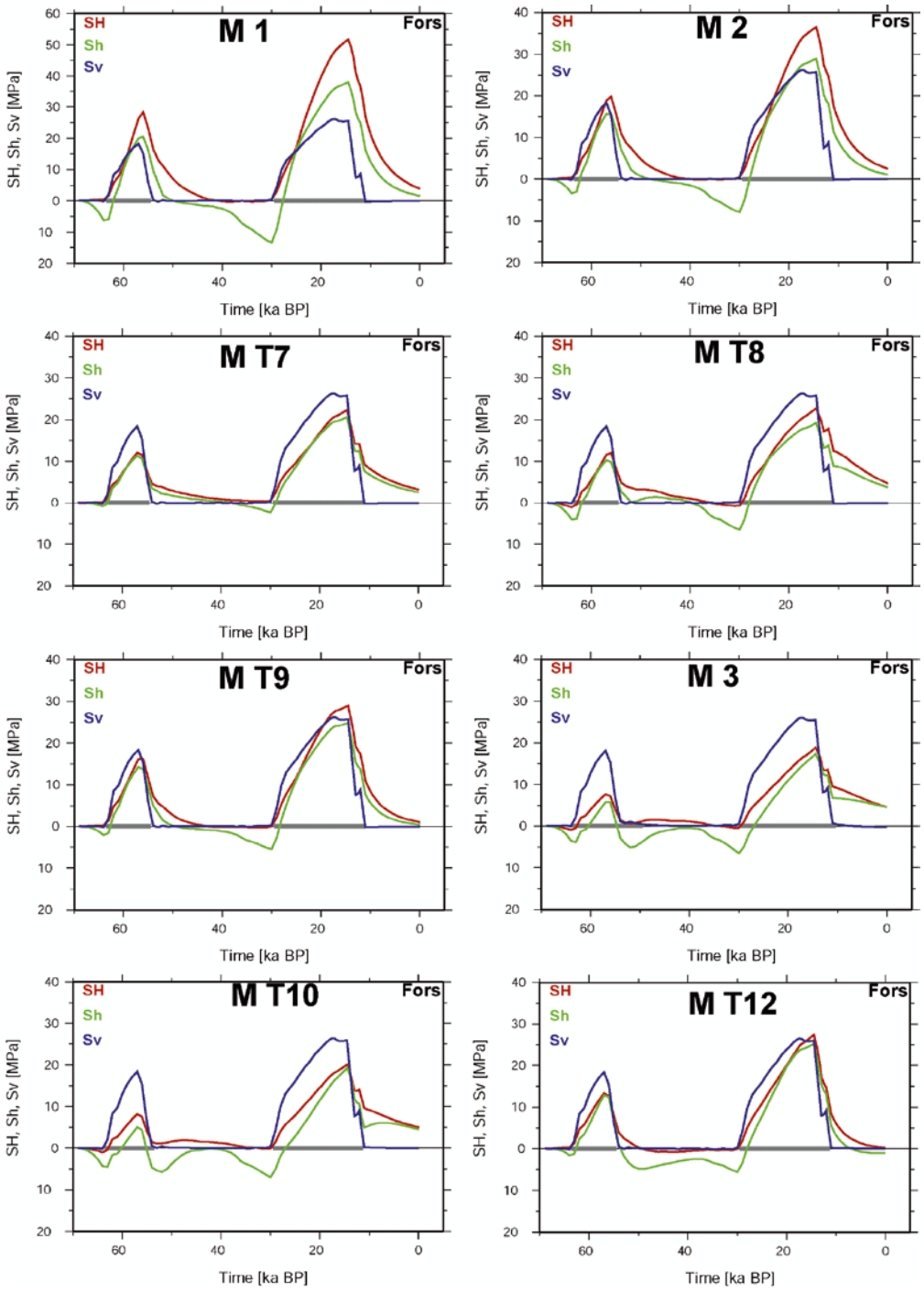

Figure 7-17. *Temporal evolution of the induced maximum horizontal (SH), the minimum horizontal (Sh) and the vertical stress (Sv) at 500 m depth in Forsmark during the glaciation. Horizontally stratified models 1, 2, T7, T8 and T9 and models 3, T10 and T12 with laterally varying lithosphere thickness, as indicated in the figure. Note that the vertical scale for model 1 is different from the other models.*

Figure 7-17 shows that for the softer earth models the induced stress field is a normal stress field (Sv > SHmax > Shmin) during much of the glaciated time. It, however, rapidly turns into a reverse field (SHmax > Shmin > Sv) as the ice melts. In models 1 and 2 the stress field turns reverse before the maximum ice thickness is attained. Models 1 and 2 correspond to models A and K in the 2D simulations of /Lund 2006b/ (note that the colour scheme is different). The results in Figure 7-17 show clearly that the 2D models do not adequately capture the glacially induced stresses along the NNE-SSW profile in Figure 4-1. For model 1 the 2D modelling underestimates the maximum stress by almost 20 MPa, whereas for model 2 the 2D results are approximately 10 MPa below the maximum in the 3D model.

In Figure 7-18 the glacially induced stress history of Oskarshamn, at 500 m depth, is displayed. Oskarshamn is situated south of Forsmark and we see that the periods of ice cover are shorter and that the ice thickness is smaller than in Forsmark. In accordance, the induced horizontal stresses are also smaller. Again, models 1 and 2 show the largest induced stresses, although in Oskarshamn the stresses induced in earth models T9 and T12 are almost as large as the model 2 results. We note that all of the models show significant time periods of tensional Shmin, again due to advancing or retreating ice which places Oskarshamn in the peripheral bulge. The stress states in the models evolve similarly as in Forsmark, being mostly normal during ice build-up and reverse after deglaciation. For Oskarshamn, the 2D predictions in /Lund 2006b/ are more similar to the 3D results than in Forsmark, in model 1 SHmax only differ by approximately 5 MPa and in model 2 there is very little difference. The 3D results for Shmin, however, show larger deviations from the 2D results in /Lund 2006b/.

Turning north to investigate the stress evolution in the region of the large endglacial faults in northern Fennoscandia, we centre our study on the central Pärvie fault. We will evaluate the stress field at 9.5 km depth, both since that is a depth which is appropriate for earthquake nucleation in northern Sweden but also since we have a lithological boundary at 10 km and we want to avoid large model effects, as the stress concentration shown in the depth profiles above. Figure 7-19 shows the Pärvie stress, and we see how different the glaciation history is at Pärvie. The area is ice covered for most of the studied period, but the thickness of the ice is not very large at any time during the glaciation. At Pärvie the vertical stress never reaches 15 MPa, whereas for example in Forsmark we see that the ice grows to approximately 25 MPa. The induced horizontal stresses grow past the magnitude of the vertical stress in 10–15 kyr and then stay relatively level during the course of the glaciation. In some earth models the horizontal stresses decay below the vertical stress before the end of glaciation, models T8, 3 and T10, whereas in others they stay high until glaciation commences. Models 1 and 2 show horizontal stresses above the vertical stress for almost the entire time period. We saw in the depth profiles above, as expected, that the horizontal stress magnitude generally decreases as we go down into the earth in the uppermost structural layer. This is an additional reason that the horizontal stresses are lower at 9.5 km at Pärvie than at 500 m depth in Forsmark or Oskarshamn. The induced vertical stress, however, does not decay very rapidly with depth and should approximate the ice load reasonably well. The stress histories in Figure 7-19, with a rapid increase in stress levels from the beginning, suggest that we may be treating the early stage of the glaciation in a less than ideal way, as we increase the ice thickness to its 68 kyr BP value over 1,000 years. However, in the /Näslund 2006/ model there is no ice in the Pärvie region at 68 kyr BP. We note that assuming our ice history is reasonably correct, none of the earth models predict very large induced stresses at Pärvie, nor do they predict maximum shear stresses which are higher than those predicted for Forsmark or Oskarshamn. Nevertheless, a magnitude 8 earthquake did occur on the Pärvie fault. In Section 9 we will explore how the glacially induced stresses interact with the pre-existing, tectonic stress field and how the combined stresses affect the stability of faults. And we will find that indeed our models predict unstable conditions in the Pärvie region at the very end of the glaciation.

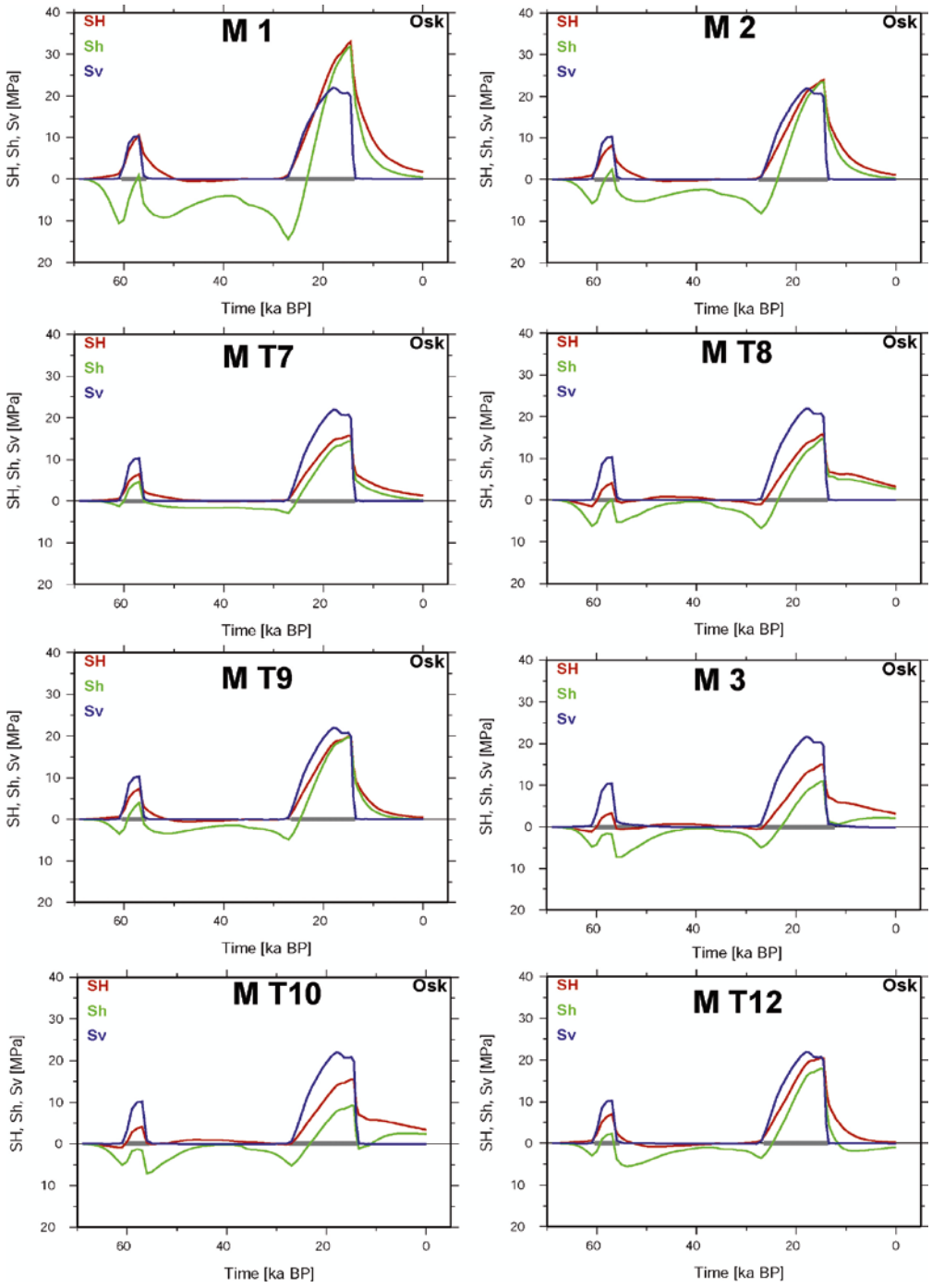

Figure 7-18. *Temporal evolution of the induced maximum horizontal (SH), the minimum horizontal (Sh) and the vertical stress (Sv) at 500 m depth in Oskarshamn during the glaciation. Horizontally stratified models 1, 2, T7, T8 and T9 and models 3, T10 and T12 with laterally varying lithosphere thickness, as indicated in the figure.*

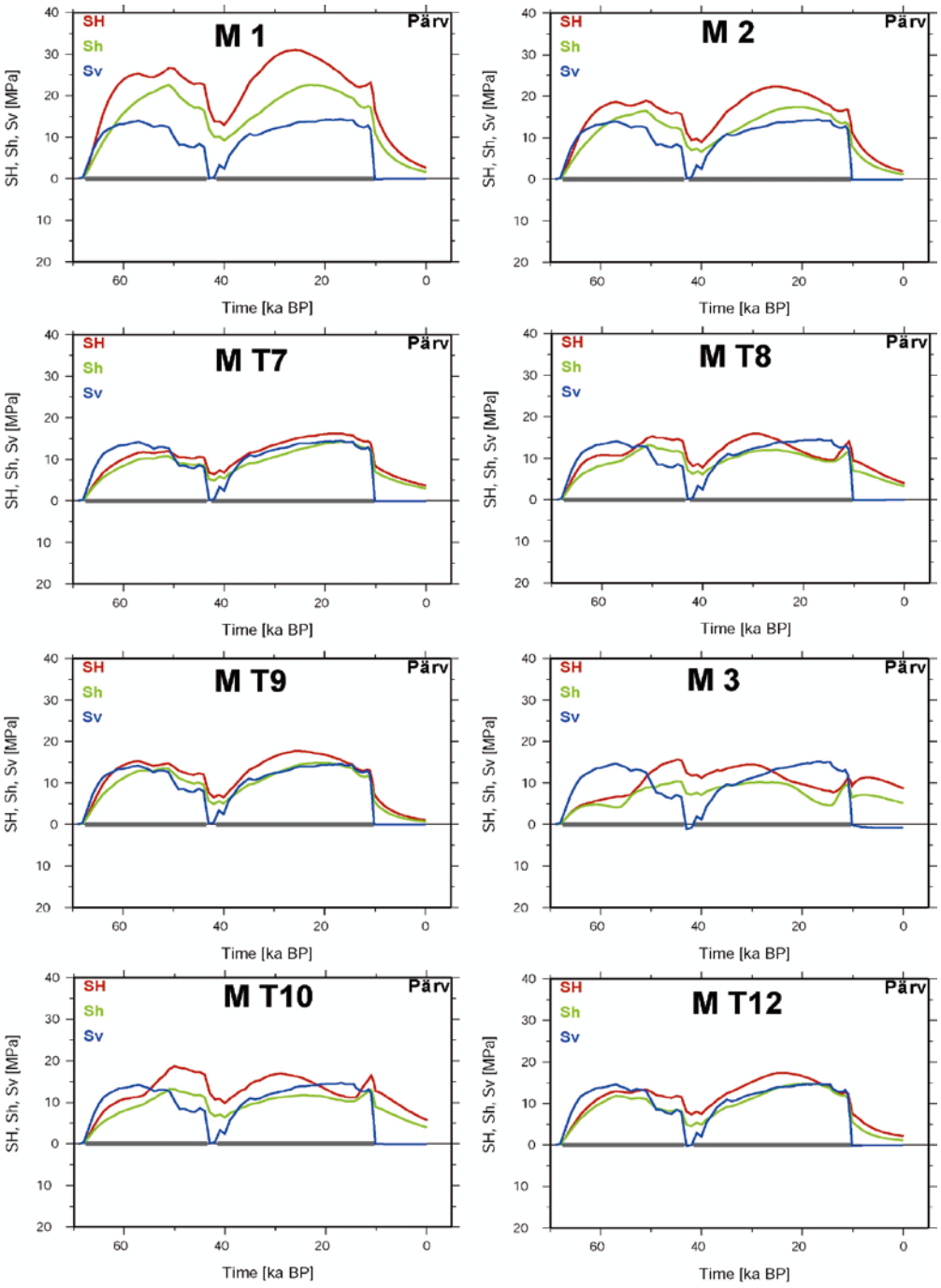

Figure 7-19. *Temporal evolution of the induced maximum horizontal (SH), the minimum horizontal (Sh) and the vertical stress (Sv) at 9.5 km depth on the central Pärvie fault during the glaciation. Horizontally stratified models 1, 2, T7, T8 and T9 and models 3, T10 and T12 with laterally varying lithosphere thickness, as indicated in the figure.*

7.4 Summary and preferred earth models

Summarizing, we first note that the glacially induced stress distributions, in map view, depth profiles or temporal evolutions are rather similar irrespective of the earth model used. This simply reflects the importance of the ice model. The earth models mainly affect the range of stress magnitudes, through the elastic properties of the model, and the rate of change of stress through the viscosity structure.

The main difference in the response of the flat layered earth models and the models with laterally varying lithospheric thickness is a shift of the area of high stress under the ice sheet to the west and a focusing of that area, especially after deglaciation, into a narrower, north-south trending region. This is likely an effect of the rapid thinning of the model from east to west. We note from the depth sections that although the stresses at depth are vastly different in the various models, the uppermost layer generally exhibit very similar stress distributions for earth models, flat or not, with similar elastic properties and rheology. We summarize the temporal stress evolution at Forsmark and Oskarshamn at 500 m depth in Table 7-1. Excluding the overly stiff earth model 1, the GIA response of our earth models to the /Näslund 2006/ ice model indicates that glacially induced horizontal stresses at 500 m depth do not exceed 40 MPa in Forsmark and not 30 MPa in Oskarshamn.

We end this section by choosing to only investigate three of the earth models above further in the forthcoming fault stability analysis. Although model 1 fits the GPS data best of our tested models we consider it unreasonably stiff in the upper lithosphere. The seismology based PREM model /Dziewonski and Anderson 1981/ has an upper crustal Young's modulus of 60–65 GPa and the site investigations in Forsmark and Oskarshamn show Young's moduli with an average of 63 GPa /SKB, 2005, 2006a/. We do, instead, include model 2 below, as an end-member model for a stiff, layered lithosphere. As we have seen, this model predicts relatively large induced stresses. Model T9 is our preferred model in terms of fit to GPS and sea-level data, and the lithospheric elastic structure is in general agreement with the Fennoscandian seismic investigations. T9 also induces stresses that are generally higher than models T7 and T8 so we will include T9. Model T12 will be our choice of model with laterally varying lithosphere as it displays the stress undulations of a very thin model but still has higher stresses than model 3. Model T10 has regions of lithosphere thickness above 300 km, which is probably an over-estimate and we therefore do not include it further. In the fault stability analysis in Section 9 we will therefore use models 2, T9 and T12.

Table 7-1. Features of the temporal stress evolution at 500 m depth in Forsmark and Oskarshamn.

Feature similar for all models	Significant differences
Stresses follow the build up and decay of the ice sheet.	The magnitudes of the induced horizontal stresses depend critically on the value of Young's modulus.
Tensional minimum horizontal stresses are induced as the ice sheet advances toward the sites.	Higher mantle viscosity decreases the horizontal stress magnitudes and increases the relaxation time of the horizontal stresses after deglaciation.
In the early stages of ice accumulation over the sites a normal stress field is induced, i.e. the vertical stress is the maximum principal stress.	The induced stresses are lower in Oskarshamn than in Forsmark, an effect of the ice model.
During the final deglaciation at the sites the induced stress field is reverse, i.e. both horizontal stresses are larger than the vertical stress.	At Oskarshamn the induced minimum horizontal stress is tensional during much of the glaciation whereas in Forsmark it becomes tensional closer in time to ice accumulation at the site. This is an ice model effect.
The magnitudes of the induced horizontal stresses are generally similar to the magnitude of the vertical stress, except in the model with very high Young's modulus at this depth.	
The effect of laterally varying lithosphere thickness is not very large at the sites, nor is there a large effect of increasing the average thickness of the laterally varying lithosphere.	

8 The background stress field

In the analysis of fault stability that follows in Section 9 we need to establish a background stress field, onto which the glacially induced stresses are superposed. In the modelling we will then assume that the background field does not change during the time of the glaciation, a reasonable assumption for the stress field due to plate tectonics which operates on time scales of millions of years. Effects due to recent sediment load, fault motion, shallow hydraulic jacking or other local phenomena will not be considered here. We note that /Påsse 2004/ estimated the amount of bedrock erosion during a glacial cycle to between 0.2 m and 4 m, which is an insignificant load redistribution in comparison to the rise and decline of the ice sheet. As we are modelling a large region in northern Europe we would preferably like to be able to use a well established regional stress field. Unfortunately, the state of stress is not very well know at depths below 1 km in Fennoscandia. Figure 8-1 shows the World Stress Map Project /Heidbach et al. 2008/ data for the region and we see that much of the data off the coast of Norway, in southern Sweden, Denmark and southern Finland show maximum horizontal stress directions in general agreement with ridge push from the Mid-Atlantic ridge. Further north the data is even more scarce and rather inconsistent. Some of the data in Figure 8-1 is from rather shallow depths, making its value for a regional field more doubtful.

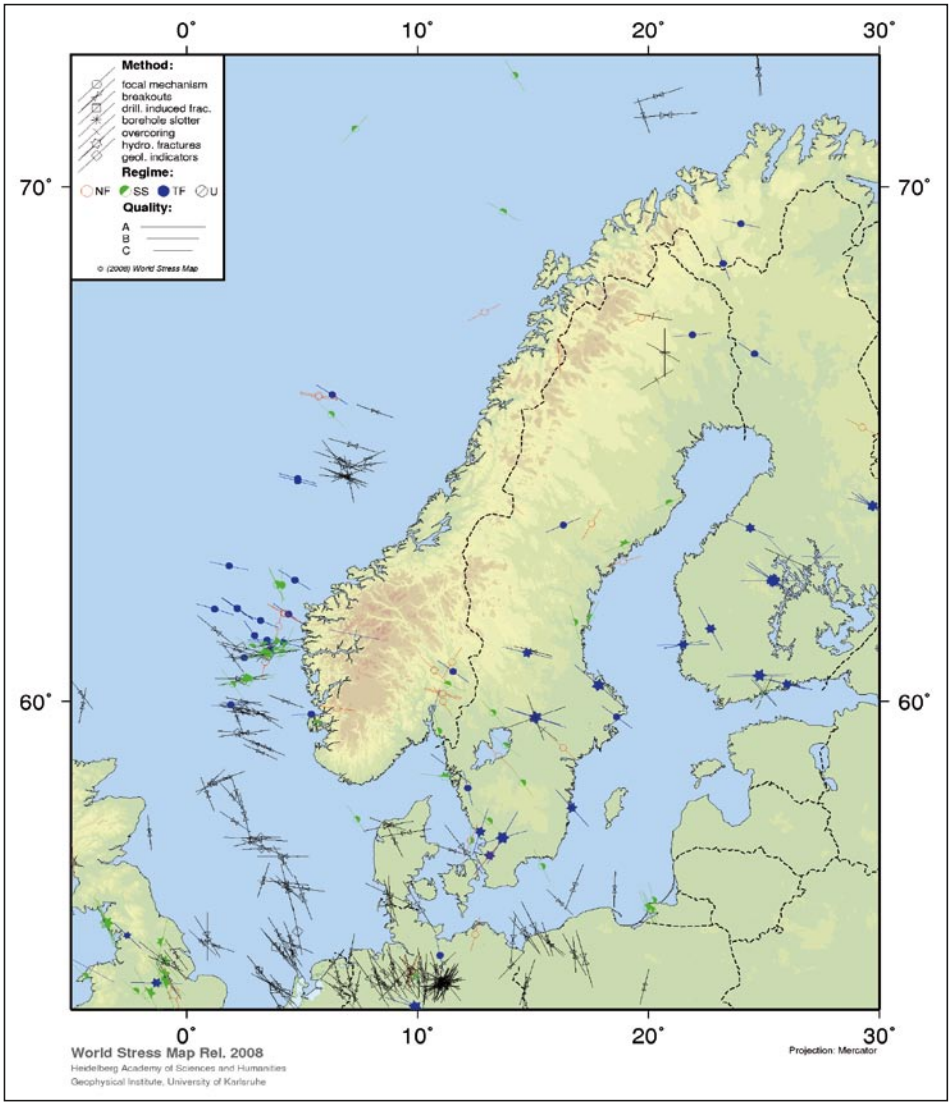

Figure 8-1. *Map of stress indicators in Fennoscandia from the World Stress Map project /Heidbach et al. 2008/. Stress regimes are indicated as normal (NF), strike-slip (SS), thrust (TF) or undetermined (U).*

Additional information comes from /Slunga 1991/, who mapped earthquake P-axis directions and found that in south-central Sweden they agree well with ridge push. In northern Sweden, on the contrary, focal mechanisms showed more diversity. /Lund and Zoback 1999/ analysed the borehole data from the 6.5 km deep Siljan boreholes in central Sweden. They found that at 5 km depth the state of stress is strike-slip, the maximum horizontal stress is directed N60-70E, in agreement with ridge-push, and the measured stress magnitudes are consistent with frictional faulting theory and laboratory derived coefficients of friction.

For our models we will construct two synthetic reference regional stress fields to use as our background fields, one strike-slip and one reverse stress state. This is done in order to assess the influence of two very different background stress states on glacially perturbed fault stability. We will simplify the regional stress field by assuming that it is dominated by ridge push such that SHmax is aligned with the local direction of plate motion. We use the Euler pole for the Eurasian plate to calculate the local direction of plate motion at each grid point in our finite element grid and use that as the direction of SHmax, shown in Figure 8-2.

There are three different lines of evidence indicating that the intraplate, continental upper crust is, in general and at some depth, in a state of frictional failure equilibrium on optimally oriented faults, see summary in /Zoback and Townend 2001/. 1) Seismicity induced by fluid injection or reservoir impoundment; 2) Earthquakes triggering other earthquakes; 3) *In situ* stress measurements in deep boreholes. Additionally, crustal stress measurements consistently agree with predictions of stress based on Coulomb frictional failure theory, using laboratory derived coefficients of friction /e.g. Townend and Zoback 2000, Colmenares and Zoback 2002/. In the light of these observations and the simplicity of the Mohr-Coulomb failure criterion, which only depends on one parameter (the coefficient of friction) that does not vary significantly between rock types /Byerlee 1978/, we will calculate the magnitudes of our synthetic background stress fields using the Mohr-Coulomb failure criterion, assuming frictional equilibrium on pre-existing, optimally oriented zones of weakness /e.g. Jaeger and Cook 1979/:

$$\frac{\sigma_1 - P}{\sigma_3 - P} = \left(\sqrt{\mu^2 + 1} + \mu\right)^2 \qquad (8\text{-}1)$$

Here σ_1 is the maximum principal stress, σ_3 is the minimum principal stress, P the pore pressure and μ the coefficient of friction. We will assume a hydrostatic pore pressure and $\mu = 0.6$. The normal to the two conjugate, optimally oriented fault planes, the two planes most likely to fail, have angles $\theta = \pm (\pi/2 - \text{atan}(\mu))/2$ to σ_1 and are located in the σ_1–σ_3 plane.

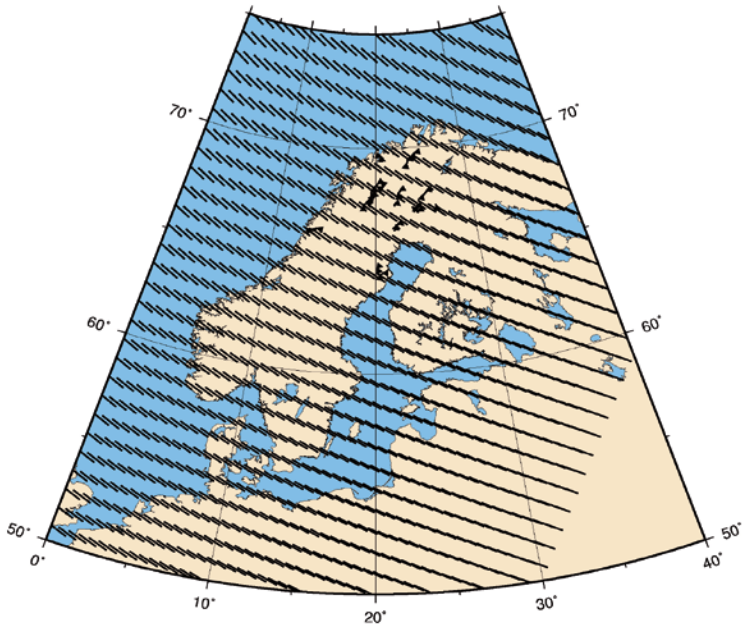

Figure 8-2. *Map of maximum horizontal stress directions used for the construction of a regional background stress field. These are based on the local direction of plate motion and indicated by short black bars.*

In Coulomb faulting theory only the maximum and minimum principal stresses are included and we therefore have to include an additional parameter to constrain the magnitude of the intermediate principal stress. We will use /after Gephart and Forsyth 1984/:

$$R = \frac{\sigma_1 - \sigma_2}{\sigma_1 - \sigma_3} \tag{8-2}$$

Finally, we compute the vertical stress from the weight of the overburden. As we will only show analysis from the uppermost layer in our model, the vertical stress is simply Sv = ρgd, where ρ is the density, g the gravitational acceleration and d the depth. We will further assume that the vertical stress is a principal stress. Using Equations 8-1 and 8-2 and Sv = ρgd, the magnitudes of principal stresses in the strike-slip stress field can be expressed as:

$$\begin{aligned} S_1 &= A(S_3 - P) + P \\ S_2 &= S_v \\ S_3 &= \frac{S_2 - P(1-A)(1-R)}{A(1-R) + R} \end{aligned} \tag{8-3}$$

where $A = (\sqrt{\mu^2 + 1} + \mu)^2$ The reverse stress field is similarly:

$$\begin{aligned} S_1 &= A(S_3 - P) + P \\ S_2 &= S_1(1-R) + S_3 R \\ S_3 &= S_v \end{aligned} \tag{8-4}$$

Using this technique to construct a regional stress field we will have SHmax oriented N123ºE in Forsmark and N121ºE in Oskarshamn. Assuming an upper crustal density of 2,750 kg/m3, as in models T9 and T12 (we use 2,730 kg/m3 in model 2), a coefficient of friction of 0.6, R = 0.5 and hydrostatic pore pressure, we calculate the magnitudes of the synthetic stress fields down to 10 km depth, see Figure 8-3. As the regional stress field is added to the glacially induced stresses after the GIA modelling, we only need snapshots of the stress fields at the depths where we will evaluate fault stability in Section 9. We will use background stresses at a relevant repository depth, 500 m, and at seismogenic depths (7.5 km, 9.5 km or 10 km depth depending on the model and application). As the upper 10 km of the crust is brittle, the strength of the crustal material is best described by a brittle failure mechanism, such as the Mohr-Coulomb criterion, and we do not invoke ductile flow mechanisms, in accordance with /e.g. Brace and Kohlstedt 1980/. In the fault stability analysis in Section 9 we will investigate how the results depend on changes in the direction of the stress field, on variations in an additional pore pressure head from an overlying ice sheet, and on changes in the relative size of the intermediate principal stress, R. Even though σ_2 is not used in the Coulomb formulation, it is conceivable that the size of the intermediate stress of the background field may influence the results when the induced field is added to it. A large induced stress in a similar direction to σ_2 may for example turn σ_2 into σ_1.

Shallow stress measurements indicate that the state of stress at repository depth (approximately 500 m) can vary considerably even over relatively short distances and may not be in failure equilibrium. As in /Lund 2006b/ we will therefore also consider background stress fields for Forsmark and Oskarshamn based on the stress measurements in the site investigation program. They will be used in Section 9 only to investigate which fault directions will potentially become unstable, Section 9.4. Table 8-1 outlines which background stress states are used for what purpose in the stability analysis in Section 9. In using the site data for a background stress model, we assume that the remanent stresses from the last glaciation are negligible, although this may not be the case, see Section 7.3. We use the stress magnitudes and directions at 500 m depth from the site characterization stress models /Hakami et al. 2008, Glamheden et al. 2007/ and establish stress fields in frictional equilibrium. For Forsmark (model valid between 400 m and 600 m depth) we have a reverse field with SHmax directed N145ºE and magnitude 41.0 MPa, Shmin 23.2 MPa, Sv 13.3 MPa. We see that the SHmax direction differs approximately 20 degrees to the south from our synthetic reverse (RF) background field. The synthetic RF field has SHmax 31.7 MPa, Shmin 22.6 MPa and Sv 13.5 MPa at 500 m depth, so the magnitude of the maximum horizontal stress is significantly smaller than indicated by the site data.

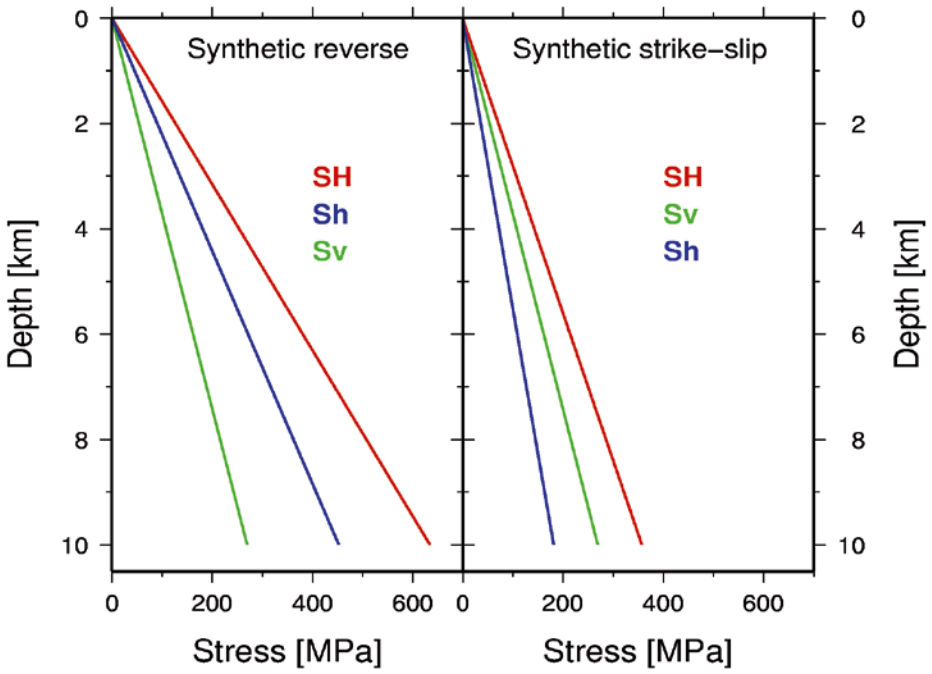

Figure 8-3. *Magnitude of the stresses in the two synthetic stress fields used for the calculation of fault stability in Section 9. Reverse stress state to the left, strike-slip stress state to the right. SH is the maximum horizontal stress, equal to the maximum principal stress (S1) here. Sh is the minimum horizontal stress, equal to S2 in the reverse field and S3 in the strike-slip field, and Sv is the vertical stress, equal to S3 in the reverse field and S2 in the strike-slip state.*

For Oskarshamn (Laxemar model valid between 400 m and 700 m depth) the observations indicate SHmax at N135ºE and 22.5 MPa, Shmin 12.0 MPa, and Sv 13.5 MPa. The synthetic direction of SHmax deviate 14 degrees from the site model and has magnitudes SHmax 17.9 MPa, Sv 13.5 MPa and Shmin 9.1 MPa, i.e. the synthetic model again has smaller magnitudes than the site model. If we assume that the two site stress states are in frictional equilibrium, and that we have a hydrostatic pore pressure at 500 m depth, the Forsmark data implies a coefficient of friction $\mu = 0.796$ and the Oskarshamn data $\mu = 0.470$, the latter a relatively low value of the coefficient of friction. In the stability analysis in Section 9, and in Table 8-1, we refer to the site specific stress states as “Local”.

Table 8-1. Usage of the various background stress models in the stability analysis in Section 9.

Stress state	CFS map	CFS time evolution	Optimal fault directions, 9.5 km depth	Optimal fault directions, 500 m depth	Stability stereonet, 9.5 km depth	Stability stereonet, 500 m depth
Synthetic reverse	X	X	X	X	X	X
Synthetic strike-slip	X	X	X	X	X	X
Forsmark local				X		X
Oskarshamn local				X		X

9 Fault stability during glaciation

In this section we will examine how the stability of faults in the crust varies as the stresses induced by the ice sheet evolve during glaciation. We will follow the methodology outlined in /Lund 2005a, 2006b, Lund and Zoback 2007/ and apply the Coulomb failure criterion to the combination of the glacially induced stress field and the background stress field. The background stress field is not included in our finite element models but added to the modelled glacial stress during postprocessing. This simplification is made possible by the fact that we do not include plastic yield in the FE model, so we do not need the full stresses there. The Coulomb criterion relates the shear stress τ on a fault plane to the normal stress σ_n via the coefficient of friction μ.

$$\tau = \mu(\sigma_n - P_f) + S_0 \tag{9-1}$$

where P_f is the pore fluid pressure and S_0 the cohesion. In /Lund 2005a, 2006b/ the term instability /Lund and Slunga 1999/ was used to describe the difference between the shear stress and the right hand side of the equation above. Here we will utilize the term CFS, Coulomb Failure Stress, as this is commonly used, especially in seismological literature, to describe stress changes, e.g. /Harris 1998/. CFS is defined as:

$$CFS = \tau - \mu(\sigma_n - P_f) - S_0 \tag{9-2}$$

and we see that if CFS is positive, the shear stress is larger than the frictional force and the fault will fail in frictional sliding, possibly as an earthquake. CFS = 0 implies frictional equilibrium on the fault, and, as discussed in Section 8, this is how we construct our background stress field. During the cause of the glaciation we will add the glacially induced stresses to the background stress field and recalculate the CFS, using faults that are optimally oriented in the current stress field. Negative CFS will then imply more stable faults, whereas positive CFS indicates more unstable, failing faults. In our modelling we will not release the stresses by letting faults slip, such as e.g. /Kenner and Segall 2000, Hetzel and Hampel 2005/, as our finite element model does not include plastic behaviour.

It is common to use the difference in CFS, ΔCFS, when addressing changes in the stress field, e.g. after large earthquakes, in order to avoid having to know the background stress field in detail. If we study the change in fault stability between time 1 and time 2, then $\Delta CFS = CFS2 - CFS1 = \Delta\tau - \mu(\Delta\sigma - \Delta P)$ implies that we only need to know the stress perturbation. Such a decomposition, however, implies that we study faults of the same orientation both in CFS1 and CFS2. That is not the case here, as we are interested in the least stable, optimally oriented faults. Once a stress perturbation has been added to the background field, in our case by the ice sheet, the fault that was optimally oriented before the onset of glaciation may no longer be optimally oriented. As we will see below, at 500 m depth in Forsmark or Oskarshamn, the optimally oriented fault will vary considerably during the glaciation. When we study the Pärvie fault, at 9.5 km depth, the large ambient stress field will not be affected by the glacially induced stresses enough that the orientation of the optimally oriented fault changes significantly. Our ΔCFS is therefore the difference in CFS between a specific time during the glacial cycle, and the background field. As the background field has CFS = 0, our ΔCFS is equal to CFS at the studied time.

When considering faults at depth in the crust, the cohesion term is insignificant and usually ignored /Brace and Kohlstedt 1980, Zoback and Healy 1984/. Here, we evaluate fault stability both at the intended repository depth of 500 m, where the cohesion term could be of significance, and at seismogenic depths were it is not. However, as we currently have no site specific data on cohesion, or rock types, we will ignore cohesion for now. The coefficient of friction is generally independent of rock type and laboratory measurements indicate a value of approximately 0.5–0.9 /Byerlee 1978/. We will use $\mu = 0.6$.

Pore pressure is an important parameter in the assessment of fault stability as the fluid pressure acts to decrease the effective normal stress on the faults. /Lund 2005a, 2006b/ ignored pore pressure, here however we will model the crust with a hydrostatic pore pressure field. As it turns out, if the background stress field is modelled with hydrostatic pore fluid pressure, and a hydrostatic pore pressure is included in the CFS calculation, the net effect is equivalent to not incorporate pore fluids at all. In that sense, the previous studies did not come to erroneous conclusions. If we, however, include an additional pore pressure field induced by the ice sheet, the CFS calculation will be affected.

We note that if the orientation of the optimally oriented fault does not change and glacially induced pore pressure is not taken into account, the CFS analysis used here yields essentially the same results as the Fault Stability Margin (FSM) analysis of /Wu and Hasegawa 1996a, b/.

The fluid pressure exerted by the water in and below the ice sheet on the underlying rock mass is very difficult to model in any detail, as it depends on factors such as the hydrological properties of the ice sheet, the time of year, the topography and hydrology of the near surface below the ice sheet /e.g. Kamb 1987, Boulton et al. 2001, SKB 2006a, Jansson et al. 2006/ and the local geothermal heat flux /Näslund et al. 2003/. Very few studies exist on the subglacial hydrology of ice sheets /Jansson et al. 2006, and references therein/, and for simplicity we here assume that the ice sheet can induce pore pressure heads varying from zero to the full weight of the local ice column. Pore pressure diffusion modelling by /Lönnqvist and Hökmark 2009/ indicates that a pore pressure head of approximately 50% below 2–3 km depth is not unreasonable. In the stability analysis below our reference model will have a pore pressure head equivalent to 50% of the local weight of the ice column. In addition, we will investigate 90% and 100% pore pressure head scenarios. We note that 100% pore pressure head effectively removes the entire effective load of the ice from the fault stability calculation, thereby counteracting most of the induced fault normal stress, so will promote fault failure. In this study we do not model pore pressure diffusion, all pressures are instantaneous static pressures which only exist when there is ice, so we will not be able to include e.g. dissipating high pore pressures after deglaciation. At 500 m repository depth in Forsmark and Oskarshamn hydraulic conductivities are large enough that this simplification does not significantly influence the results /Lönnqvist and Hökmark 2009/. However, for stability calculations at 9.5 km, the hydraulic properties are likely such that pore pressure diffusion takes significant time.

Here we will present maps of the modelled stability field in Fennoscandia at 18.5 kyr BP and 10 kyr BP. We use the horizontally stratified earth models 2 and T9, and the laterally varying T12. For models 2 and T9 we show the results at 10 km depth and for model T12 at 7.5 km depth, dictated by the mesh of the finite element models. We will also show depth profiles through the three earth models along the NNE-SSW line in Figure 4-1 at these times. The temporal evolution of the stability field at Forsmark, Oskarshamn and the central Pärvie fault will be traced, as well as the orientation of the least stable, the optimally oriented, fault. As the stability calculation depends critically on the background stress field, we will investigate how variations in the three least well known parameters of the background stress calculation affect the resulting stability field. These parameters are the glacially induced pore pressure, the relative magnitude of the intermediate principal stress through the parameter R and the direction of SHmax in the regional stress field. Obviously, our assumption of a crust in frictional equilibrium using a coefficient of friction of 0.6 may not be valid everywhere. To that respect we show examples using the locally measured stress fields in Forsmark and Oskarshamn. We will end this section by showing stereonets of the stability field at select times through the glacial cycle to illustrate which faults, aside from the optimally oriented, are affected by instability.

9.1 Fault stability maps at 18.5 kyr and 10 kyr BP

In Figures 9-1 and 9-2 we show the Fennoscandian stability field at seismogenic depth (10 km for models 2 and T9, 7.5 km for model T12) at 18.5 kyr BP and 10 kyr BP, corresponding to the last glacial maximum and the end of glaciation, respectively. The background stress fields used in these figures are the two synthetic fields constructed as described in Section 8, with the direction of SHmax equivalent to the local direction of plate motion, and with R = 0.5 and glacially induced pore pressure heads at 50% of the ice weight. The glacial pressure heads only affect stabilities at 18.5 kyr BP since at 10 kyr BP the ice, and hence the excess pressure, has disappeared.

Inspecting Figure 9-1 we see, as expected, that at full glacial load faulting is demoted (negative CFS, blue colour) below the ice sheet irrespective of the background stress field and irrespective of the earth model. In the reverse background field (right column) the entire region shows less likelihood of faulting, and the lighter areas along the Scandinavian mountain range, especially in model 2, correspond to areas where the ice sheet is thinner, thus the vertical load is smaller but the induced flexural stresses from further east are still large. The laterally varying T12 model shows very similar response as the two flat models.

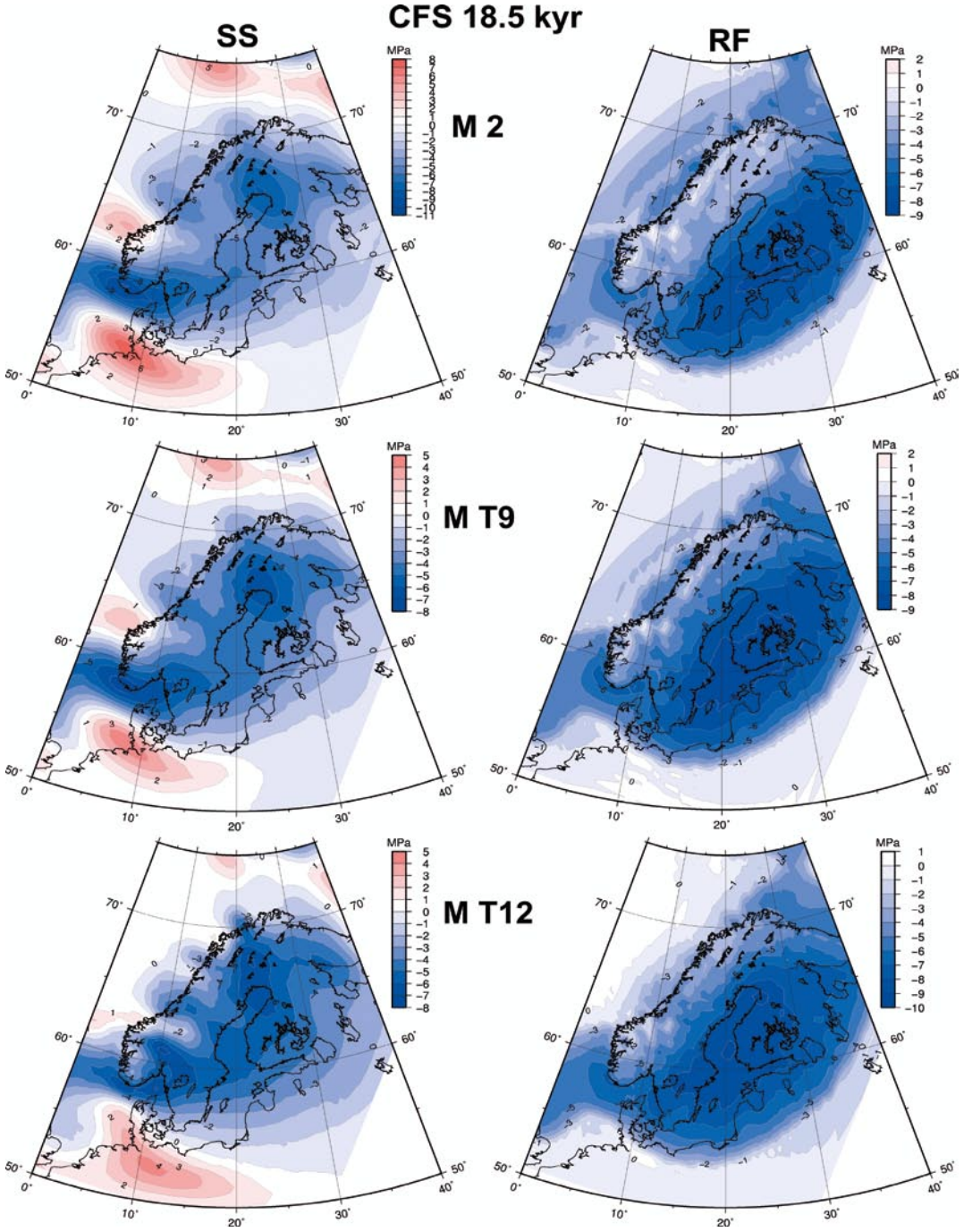

Figure 9-1. *Maps of fault stability (negative, blue colours are stable) at 10 km (Models 2 and T9) and 7.5 km (T12) depth and 18.5 kyr BP. Strike-slip background stress field (SS) in left column, reverse background field (RF) in the right column.*

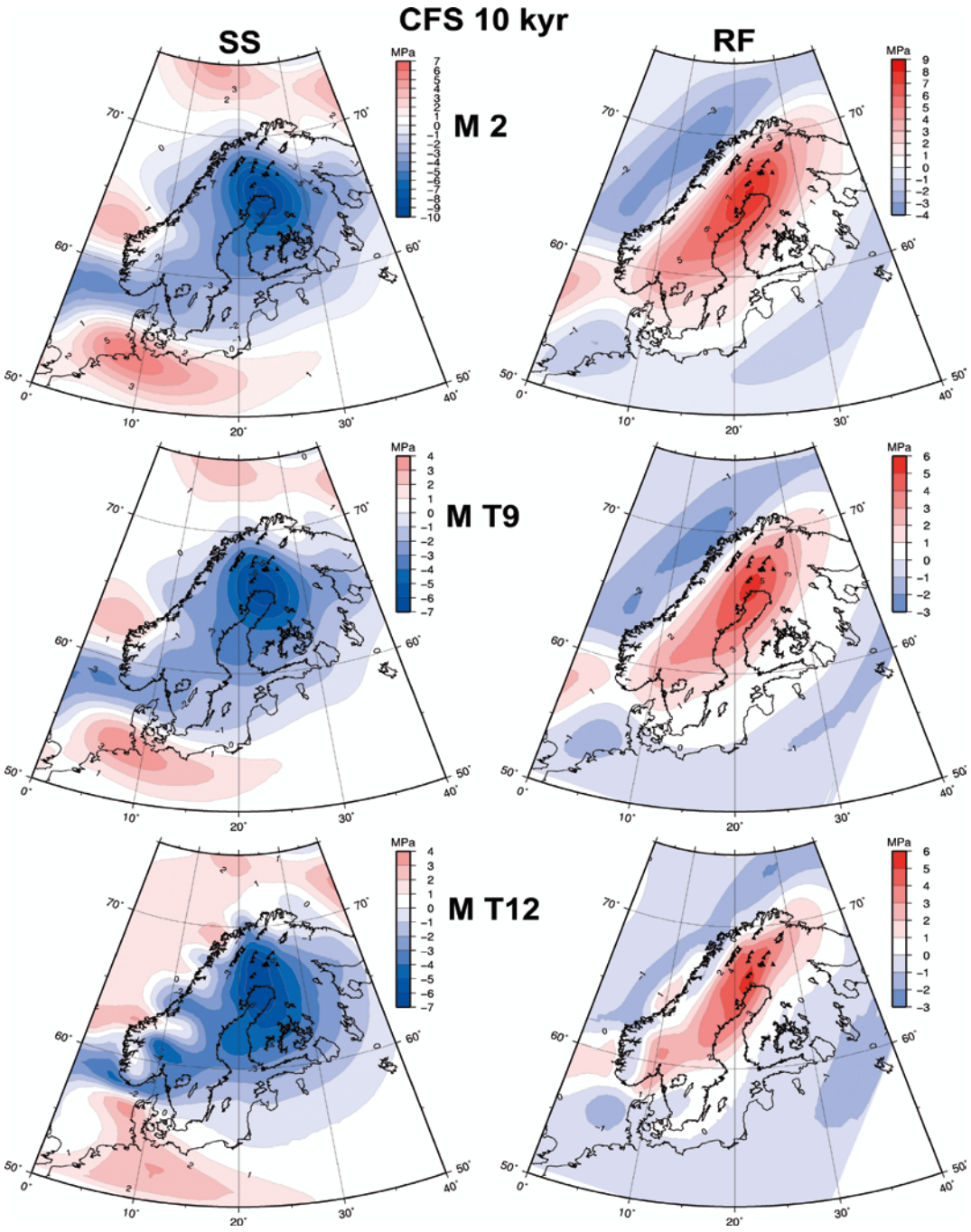

Figure 9-2. *Maps of fault stability (negative, blue colours are stable) at 10 km (Models 2 and T9) and 7.5 km (T12) depth and 10 kyr BP. Strike-slip background stress field (SS) in left column, reverse background field (RF) in the right column.*

With a strike-slip background field (left column) we see that we have three distinct regions of promoted fault failure, in southern Denmark and northern Germany, in southwestern Norway and north of Norway. These areas correspond to areas where the glacially induced SHmax and Shmin are both negative, Figures 7-1, 7-2, 7-11 and 7-12.

Once deglaciation is complete, we expect from earlier studies that the stability field changes significantly for the reverse background stress state, and this is also shown in Figure 9-2. All earth models now predict wide spread fault instability in large parts of Sweden, Norway and Finland, with the highest failure potential centred in northern Sweden in the area of the large endglacial faults. Model 2 shows the highest, most widely spread failure potential, as expected due to the higher stresses. Models T9 and T12 have lower magnitude and more concentrated faulting potential. We also note that the thinning of the lithosphere to the west in model T12 seems to increase fault stability. Interestingly, all three earth models in this particular stress field indicate that the Pärvie fault, largest of all known endglacial faults, is located at the edge of the area of increased faulting potential. We will explore this further in Section 9.4.

Using a strike-slip background stress Figure 9-2 shows, in agreement with previous 2D studies /Lund 2005a, Lund and Zoback 2007/, that fault failure is still demoted under the central parts of the formerly glaciated region. The main locus of increased fault stability is in northern Sweden, in the region of the endglacial faults, but we see that except for southernmost tip, all of southern Sweden has increased fault stability. As previously, model 2 has the highest magnitudes of faulting potential, whereas model T12 shows larger variability and increasing faulting potential as the lithosphere thins to the west.

The results in Figure 9-2 suggests that in order to have models which agree with the field observations, we may have to use a background stress field which is a combination of a strike-slip field in the south and a reverse field in the north. In the south there is much data suggesting a strike-slip state of stress in the crust at depth, while in the north, although the stress data to date are inconclusive, the endglacial faults are unequivocally there suggesting a reverse background field. Exactly how such a combined stress field would look like, where the transition from strike-slip to reverse occurs and which effect it would have on the stability field is a subject for further investigation. Some hints may be given in the parameter tests below.

9.1.1 Parameter sensitivity

In Figures 9-3 and 9-4 we illustrate how the stability field for earth model T9 changes as we adjust the parameters describing the background stress field. We rotate the direction of SHmax ±45 degrees, clock-wise positive, from the plate motion direction, we model 0% and 90% induced pore pressure heads and we change R to 0.1 and 0.9, for both the strike-slip, Figure 9-3, and the reverse, Figure 9-4, stress fields. We use earth model T9 as illustration here, but the differences in the response is earth model independent.

The upper row of Figures 9-3 and 9-4 shows that the orientation of SHmax in the background field has a large impact on the resulting stability field, which we could conclude already from Figures 9-1 and 9-2 where we added different glacially induced fields to the same background field. We see, however, from Figures 9-3 and 9-4 that the overall effect is mostly a rotation of the features present in Figure 9-1 and 9-2. The reverse field still indicates fault instability in central Scandinavia and the strike-slip field still produces more stable faults.

The magnitude of the stress ratio R determines how close σ_2 is to σ_1 and σ_3, relatively. In a strike-slip stress state, R = 0.1 indicates that σ_2 (the vertical stress) is close to σ_1 and the stress state therefore obliquely normal. R = 0.9, on the contrary, indicates that σ_3 is similar to σ_2 and the stress state obliquely reverse. For a reverse stress field, R = 0.1 means strongly reverse whereas R = 0.9 indicates close to strike-slip. In Figures 9-3 and 9-4, therefore, the maps with R = 0.9 (middle, right column) show the stability field when the background field moves from strike-slip toward reverse, and vice versa. Figures 9-3 and 9-4 show that at 10 km depth the glacial stresses are generally too small to change the stress state and the effect of the size of the intermediate principal stress is almost irrelevant to the stability analysis when the CFS-criterion is used.

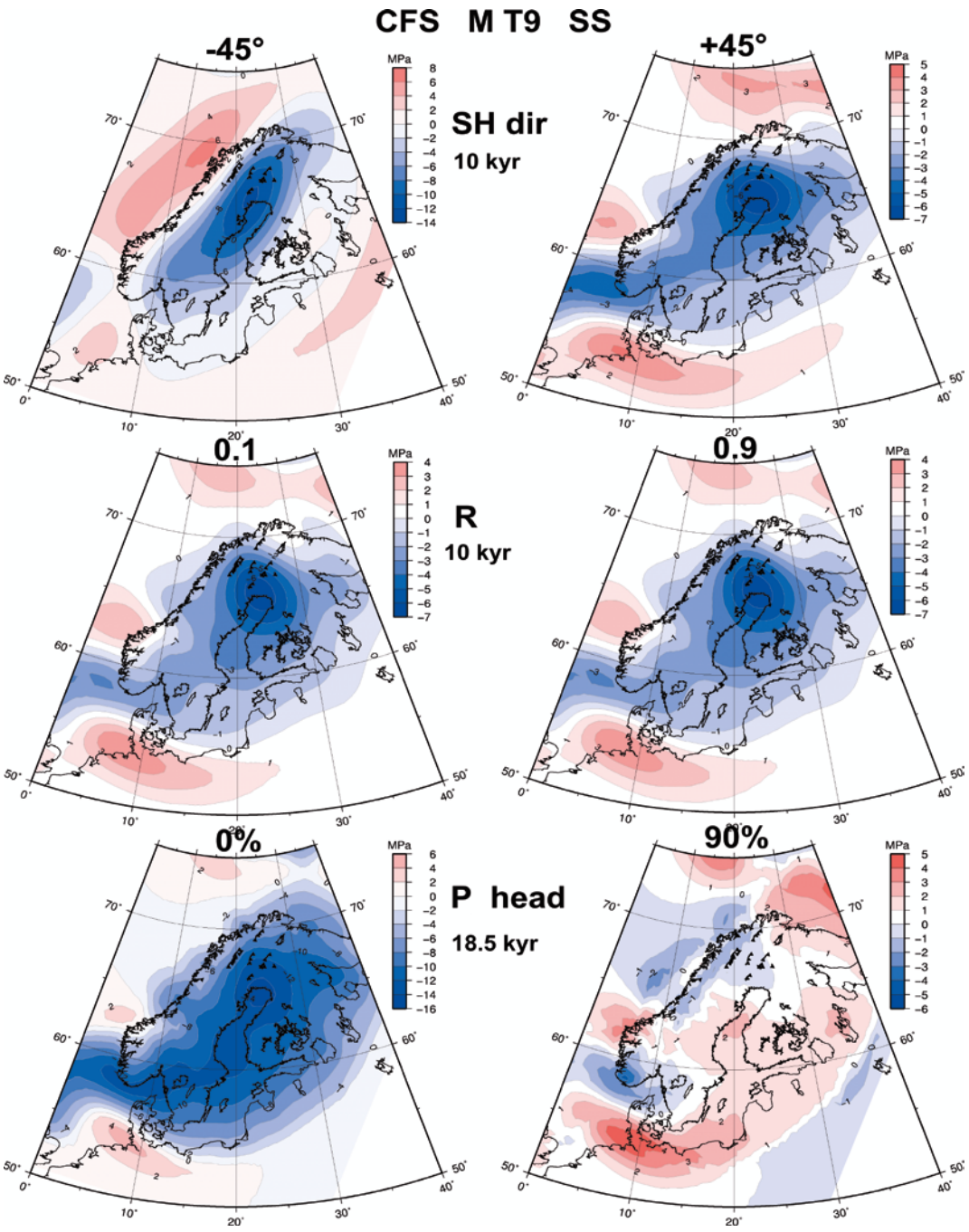

Figure 9-3. *Maps of fault stability (negative, blue colours are stable) at 10 km depth for model T9 and a strike-slip background stress field. Upper two rows at 10 kyr BP. Upper row: Direction of SHmax 45 degrees less, more northerly, than the reference (left), 45 degree more, southerly, than the reference (right). Middle row: R = 0.1 (left), R = 0.9 (right). Bottom row: Glacially induced pore pressure at 18.5 kyr BP, 0% of ice weight (left), 90% of ice weight (right).*

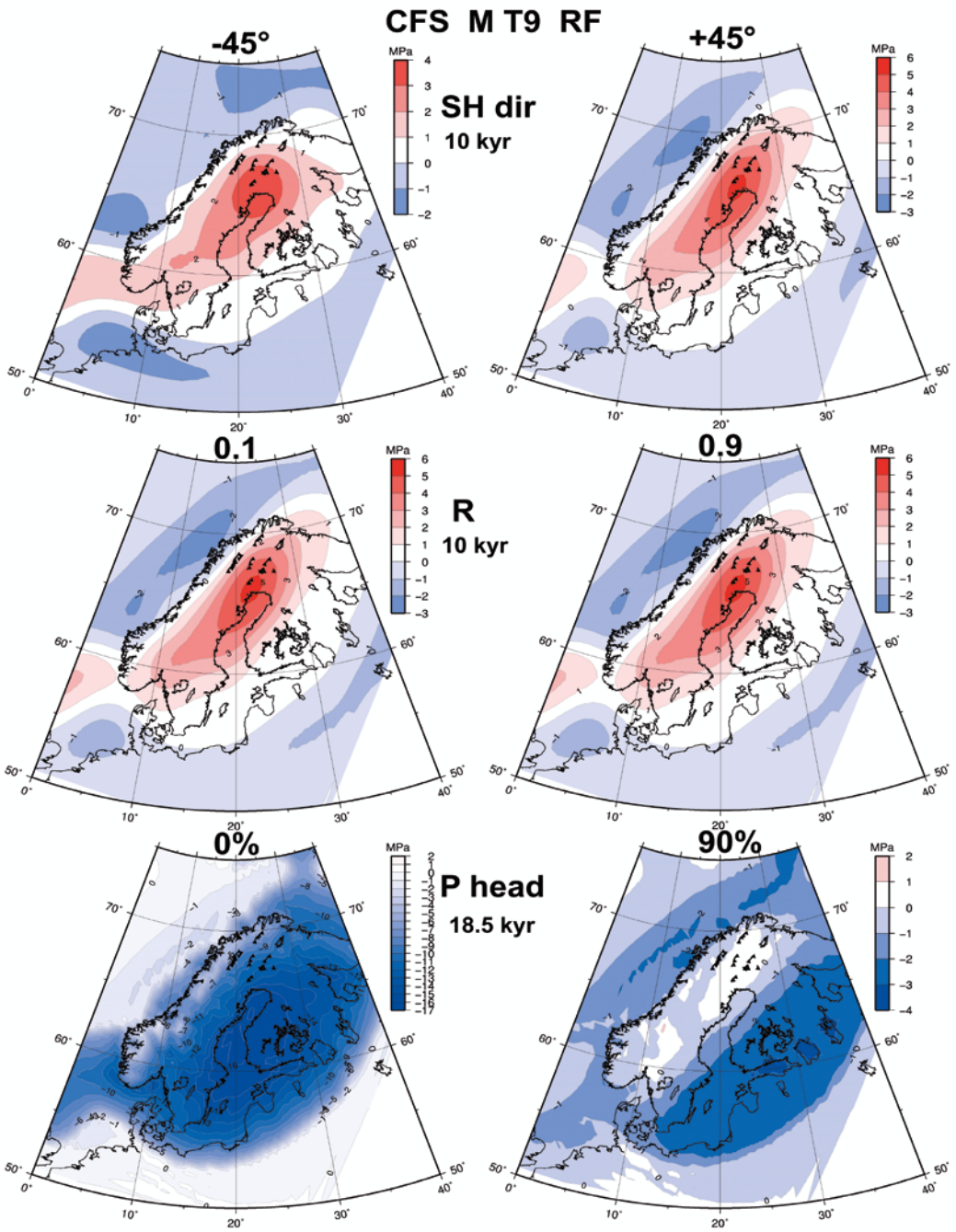

Figure 9-4. *Maps of fault stability (negative, blue colours are stable) at 10 km depth for model T9 and a reverse background stress field. Upper two rows at 10 kyr BP. Upper row: Direction of SHmax 45 degrees less, more northerly, than the reference (left), 45 degree more, southerly, than the reference (right). Middle row: R = 0.1 (left), R = 0.9 (right). Bottom row: Glacially induced pore pressure at 18.5 kyr BP, 0% of ice weight (left), 90% of ice weight (right).*

The lower row in Figures 9-3 and 9-4 shows that pore pressure heads that are as high as 90% of the ice load are likely to induce fault instability even at the height of glaciation, both for reverse and strike-slip stress states. As discussed above, it is the effective normal stress that acts in the Coulomb criterion and when the pore pressure is almost as high as the induced vertical stress there is not enough normal stress to stabilize the faults.

9.2 Depth profiles

Figures 9-5 and 9-6 show how the stability field varies with depth along the NNE-SSW profile in Figure 4-1. These depth profiles correspond to the maps shown in Figures 9-1 and 9-2, they have SHmax directions along the local plate motion directions, R = 0.5 and a glacial pore pressure head of 50%.

Figure 9-5 shows the stability field at 18.5 kyr BP and we see that for a reverse background field all of the elastic lithosphere is essentially stable. Model T12 shows some tendencies to increased fault potential at the north and south parts of the profile, but these are mostly in the lithospheric mantle. A strike-slip background field, on the contrary, shows that the areas of decreased stability seen in Figures 9-1 and 9-2 extend to depth in the models and that the central stable region extends all through the elastic lithosphere.

At the end of deglaciation, 10 kyr BP, the depth profiles again reflect the shallow features in Figures 9-1 and 9-2. For the reverse background stress field, a large high magnitude region of decreased fault stability develops in the centre of the model, under the former centre of the ice load. The response is very similar in all three earth models and continues down to the boundary between layer two and three in the lithosphere. We also note that for the softer models T9 and T12, high faulting potential concentrates at the top of layer two. The strike-slip background stress models show more variability, with unstable areas outside the edge of the former ice sheet and stable areas in the formerly glaciated region, extending to depth. The models also show that the stability pattern reverses deep down in the lithosphere, when we have come below the flexural neutral surface.

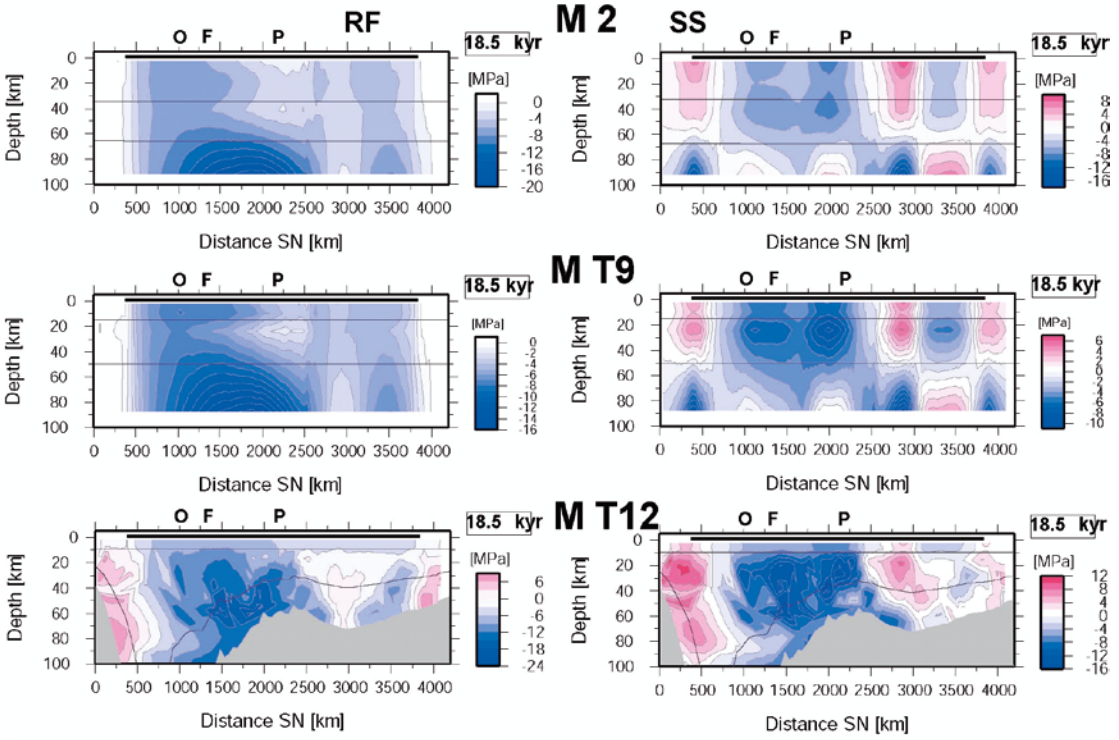

Figure 9-5. *Depth profiles of fault stability at 18.5 kyr BP along the line shown in Figure 4-1. Left column: reverse background state of stress. Right column: strike-slip background state of stress. Earth models 2, T9 and T12 from top to bottom, respectively. The stress state has the reference plate motion direction, R = 0.5 and pore pressure head 50%. The maximum extent of the ice sheet is indicated by the black line on the upper surface. Material boundaries are shown with grey lines. The locations of Oskarshamn (O), Forsmark (F) and endglacial faults (P) are marked.*

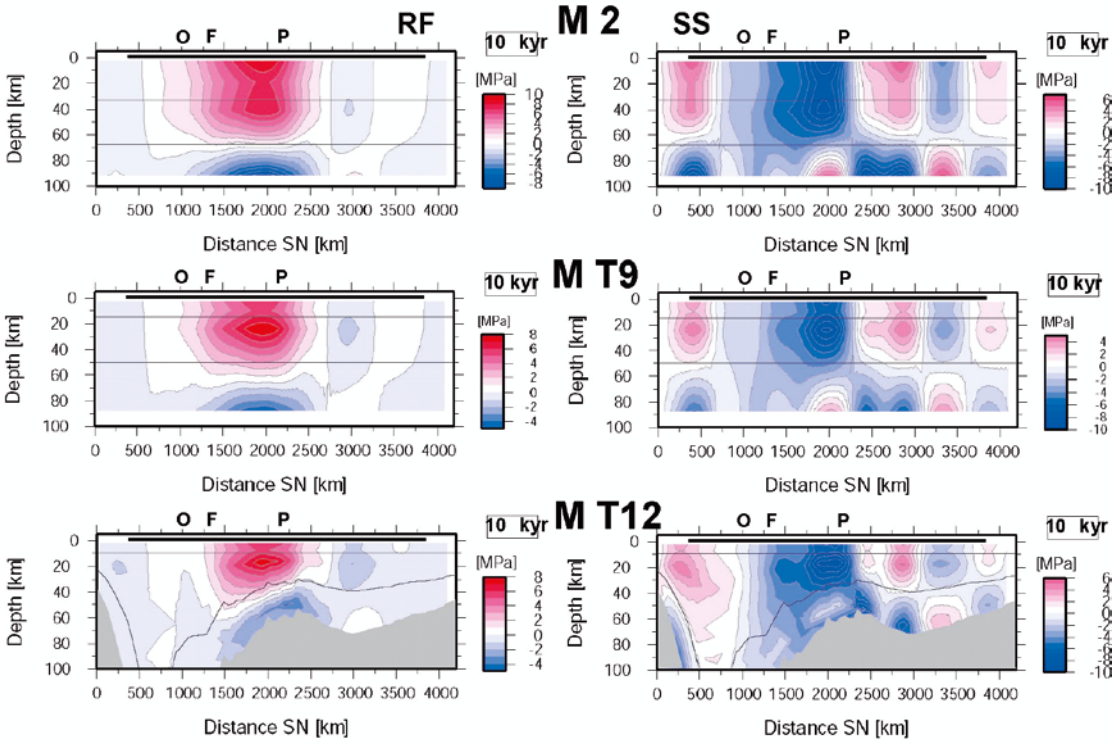

Figure 9-6. *Depth profiles of fault stability at 10 kyr BP along the line shown in Figure 4-1. Left column: reverse background state of stress. Right column: strike-slip background state of stress. Earth models 2, T9 and T12 from top to bottom, respectively. The stress state has the reference plate motion direction, R = 0.5 and pore pressure head 50%. The maximum extent of the ice sheet is indicated by the black line on the upper surface. Material boundaries are shown with grey lines. The locations of Oskarshamn (O), Forsmark (F) and endglacial faults (P) are marked.*

9.3 Temporal evolution of the stability field in Forsmark and Oskarshamn

We now turn to the temporal evolution of the stability field at the two sites investigated as possible locations for a Swedish nuclear waste repository, Forsmark and Oskarshamn, see locations in Figure 4-1. We show the stability field at 9.5 km depth which is in the depth interval where many of the Swedish earthquakes nucleate /Slunga 1991, Bödvarsson et al. 2006/. Using the simplicity of the temporal evolution figures we investigate how variations in the parameters used to estimate the background stress field influences the results. We will use the two synthetic background stress models from Section 8, one strike-slip and one reverse, where SHmax is aligned with the local direction of plate motion. Here we set R = 0.5 and an ice induced pore pressure head of 50% of the ice weight. All three earth models used above, models 2, T9 and T10, are investigated below using the induced stress results from the sub-models, Section 7.3.

Figures 9-7 and 9-8 show how variations in the direction of SHmax affect the evolution of fault stability. We add (blue curves) or subtract (red curves) 45 degrees to the direction of plate motion (green curves) at Forsmark and Oskarshamn, making them N168ºE and N78ºE in Forsmark, and N166ºE and N76ºE in Oskarshamn. Figure 9-7 shows the response of a reverse background stress field and we see that variations in the SHmax direction has very little effect on the stability fields. Figure 9-7 shows, for all earth models, how fault stability is enhanced during the periods of ice cover, and how the stability decreases rapidly at deglaciation. The stiffer model 2 predicts higher levels of fault instability, as expected, and all models predict onset of faulting at the end of the glaciation, both in Forsmark and in Oskarshamn. In Forsmark there is also a tendency toward poor stability at the end of the stadial at 60 kyr BP. We see that model 2 predicts an onset of fault instability significantly before the end of glaciation in Forsmark.

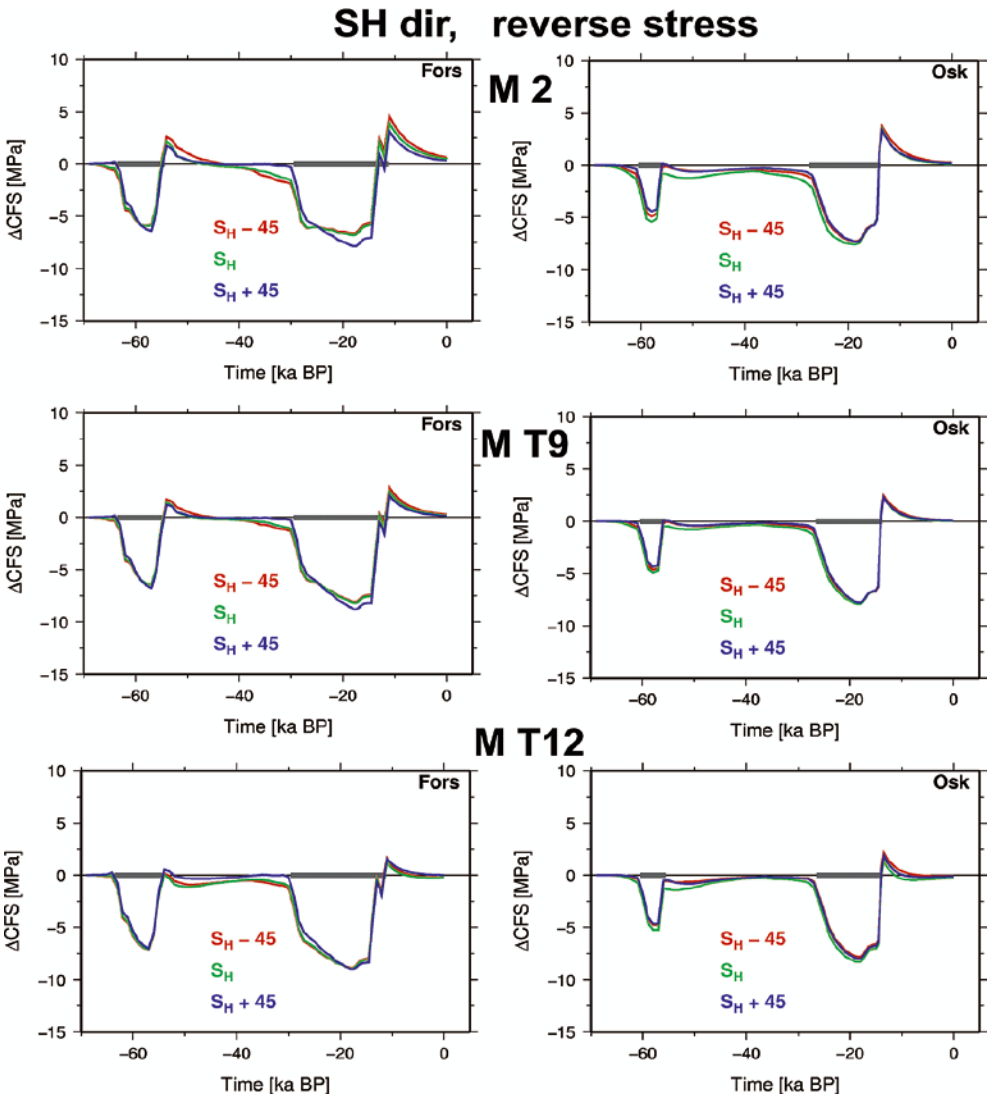

Figure 9-7. *Temporal evolution of the stability field at 9.5 km depth in Forsmark, left, and Oskarshamn, right. Reverse background stress field with SHmax in the direction of plate motion (green lines). Variations in the direction of SHmax with +45 degrees (blue lines) and –45 degrees (red lines). The stress state has R = 0.5 and pore pressure head 50%. Earth models 2, T9 and T12, from top to bottom, respectively. The grey lines at zero indicate the temporal duration of the ice sheet.*

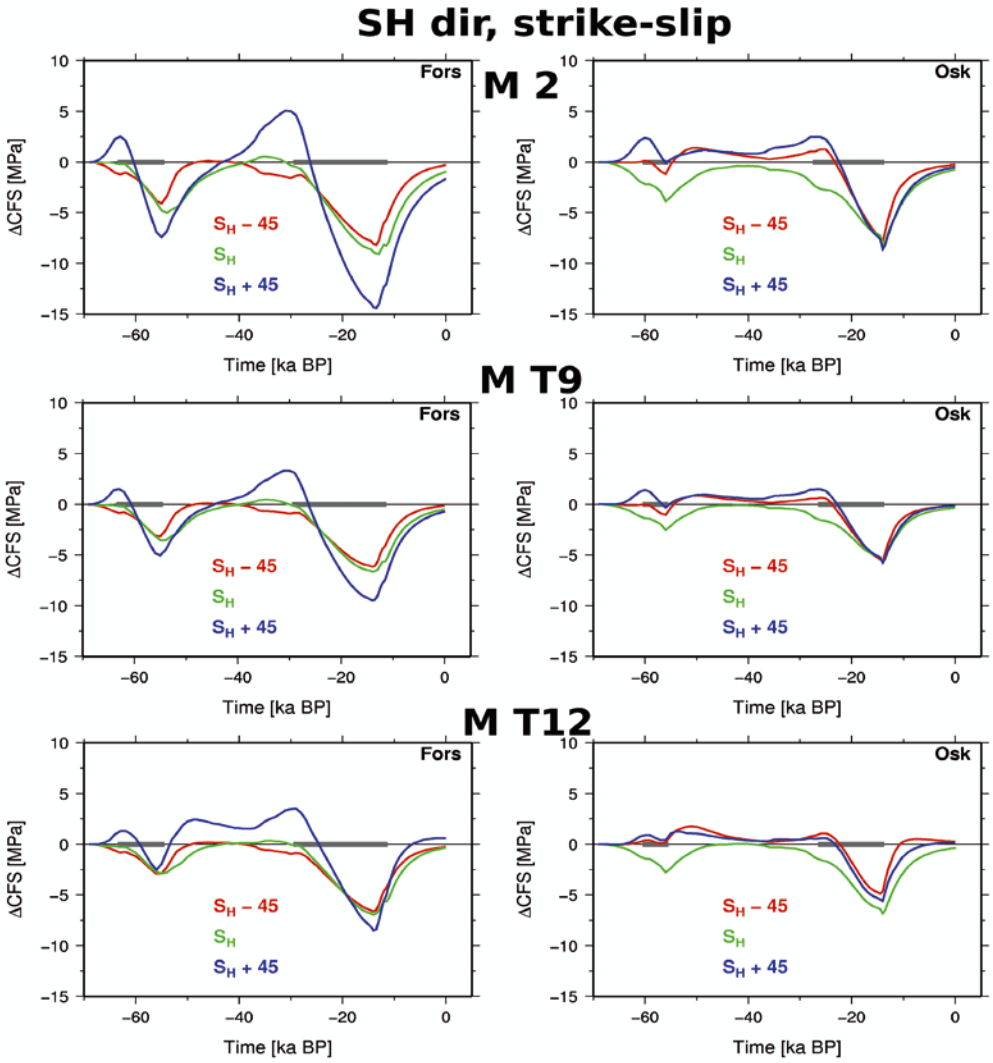

Figure 9-8. *Temporal evolution of the stability field at 9.5 km depth in Forsmark, left, and Oskarshamn, right. Strike-slip background stress field with SHmax in the direction of plate motion (green lines). Variations in the direction of SHmax with +45 (blue lines) and –45 degrees (red lines). The stress state has R = 0.5 and pore pressure head 50%. Earth models 2, T9 and T12, from top to bottom, respectively. The grey lines at zero indicate the temporal duration of the ice sheet.*

If the background stress field is strike-slip, the pattern of stability is much different, see Figure 9-8, and depends critically on the direction of SHmax. Interestingly, we see that the reference model with SHmax along the plate motion direction, produces a stress field which remains virtually stable all through the glaciation at Oskarshamn and only has a short period of instability around 32 kyr BP at Forsmark. Adding or subtracting 45 degrees, however, produces stress fields that show significant instabilities at Oskarshamn while at Forsmark the addition of 45 degrees to SHmax produces large instability but the subtraction of 45 degrees generally does not. The strike-slip background field predicts major instabilities at other points in time as compared to the reverse field. We see in Figure 9-8 that both Forsmark and Oskarshamn experience periods of less stable faults before and at the onset of the last stadial, instead of at the end of it. Comparing to Figures 7-17 and 7-18 we see that the unstable periods in the strike-slip background field seem to occur when the induced minimum horizontal stress is negative.

The large differences in the response of the strike-slip and the reverse background fields to variations in SHmax direction depend on the sensitivity of the corresponding optimally oriented faults to the stress perturbations produced by the ice sheet at 9.5 km depth. Generally, the vertical faults that are optimal in the strike-slip stress field react strongly to the time when there is a large stress difference in the horizontal stresses (cf Figures 7-17 and 7-18) while the gently dipping optimal faults in the reverse stress field react to largest differences between the induced vertical and maximal horizontal stresses.

Due to its dependence on the vertical stress, fault stability in the reverse stress state is therefore less sensitive to horizontal rotations of the field. We have not explicitly examined glacially induced stress directions over time in Forsmark and Oskarshamn, which is necessary for a complete understanding of the influence of relative rotations between the background stresses and the glacial stresses. The effects are however clearly shown in Figures 9-7 and 9-8.

We have seen that the stability field can be rather sensitive to variations in the background stress field. Does that also hold for variations in the relative size of the intermediate principal background stress? As indicated in Figures 9-3 and 9-4, it does not. This is due to the depth at which we investigate the stability field here, 9.5 km, where the ambient stresses are much higher than the glacially induced stresses. The vertical stress at 9.5 km depth is 256 MPa, a factor ten higher than the glacial stresses. Plotting the temporal variation of fault stability with different values of R produces results that are similar to the thickness of the plotted line. We will therefore not show results of the R variation here. However, at 500 m depth there is a noticeable effect of fault stability due to variations in R, which we will see when studying the orientation of the optimally oriented planes at 500 m depth over time, in Section 9.4.

High pore fluid heads induced by the ice sheet have a severe effect on the stability of faults, as we noted above. In Figure 9-9 and 9-10 we study the effect of raising the pore pressure head from 50% (red) to 90% (green) and 100% (blue) of the ice weight over Forsmark and Oskarshamn. Figure 9-9 shows the reverse stress state and we note that our static approach to incorporating the pressure head is clearly visible, as all three lines coincide outside of the glacial periods. We also see that increased pore pressure tends to decrease the magnitude of the stability of faults during the stadials while it does not affect the magnitude of decreased stability very much. Interestingly, although 100% pore pressure head implies that no effective vertical stress is added to the system, faults remain stable for significant periods of time. This is because the high pore pressure decreases the horizontal stresses by the same amount. All three earth models show similar response, but we note that in model 2 stability decreases earlier during the stadials.

In a strike-slip background stress field, very high induced pore pressures are difficult to stabilize, as we see in Figure 9-10. All three earth models show decreased fault stability during large parts of the stadials. We note, however, that as the ice sheet builds up, horizontal stress is induced in the lithosphere which partially counteracts the effect of high pore pressures on stability.

In this section we have studied the fault stability evolution at 9.5 km depth. We do not show the corresponding figures of fault stability at 500 m depth, but note that they are very similar to the 9.5 km results. This is due to our construction of the synthetic background field in frictional equilibrium, which makes the stability field sensitive to perturbations and not the absolute magnitude of the induced stresses. We will see in the next section, however, how the range of unstable faults vary significantly with depth.

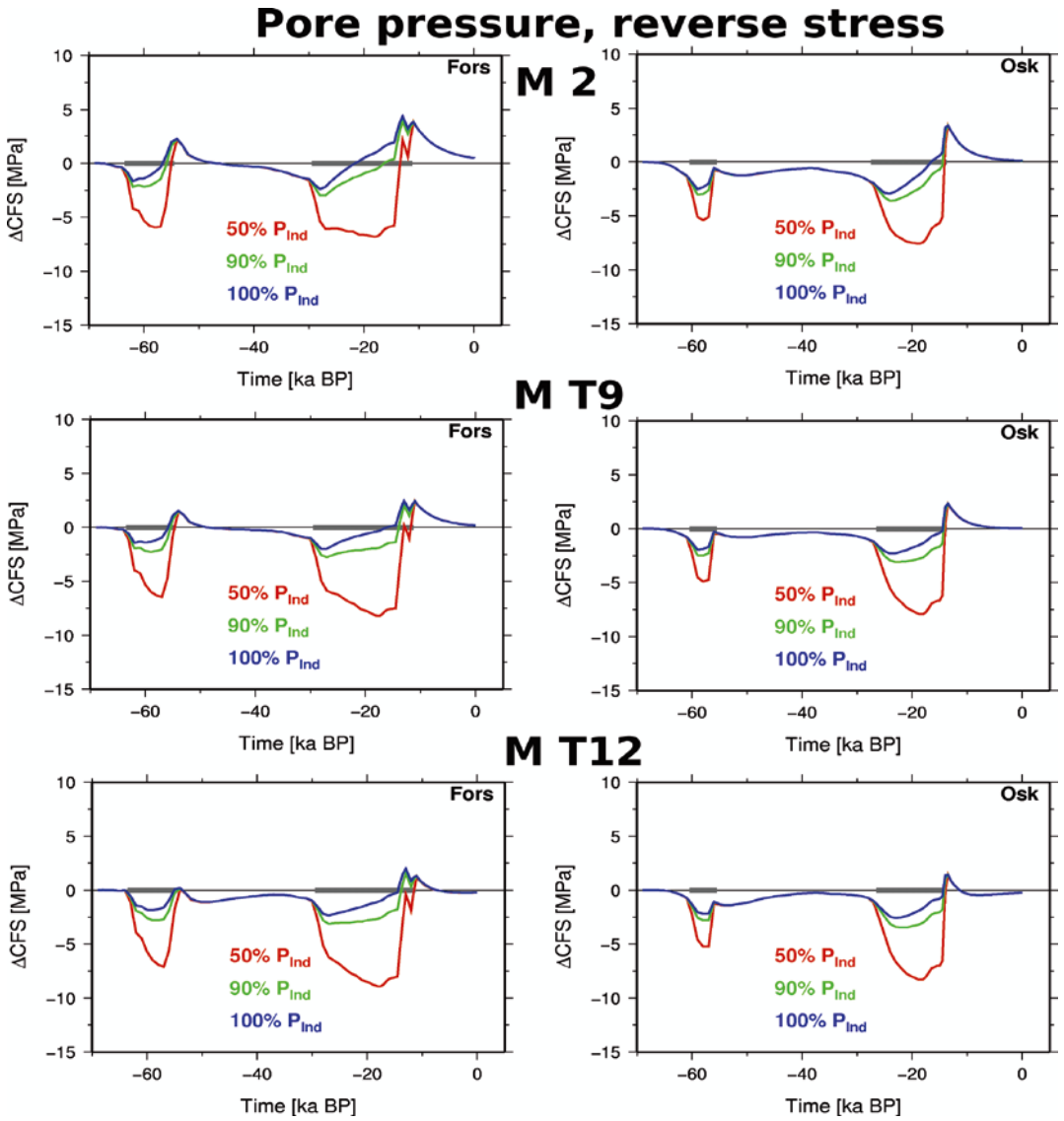

Figure 9-9. *Temporal evolution of the stability field at 9.5 km depth in Forsmark, left, and Oskarshamn, right. Reverse background stress field with glacially induced pore pressure head, Pind, of 50% (red lines). Variations in Pind with Pind = 90% (green lines) and Pind = 100% (blue lines). The stress state has SHmax in the direction of plate motion and R = 0.5. Earth models 2, T9 and T12, from top to bottom, respectively. The grey lines at zero indicate the temporal duration of the ice sheet.*

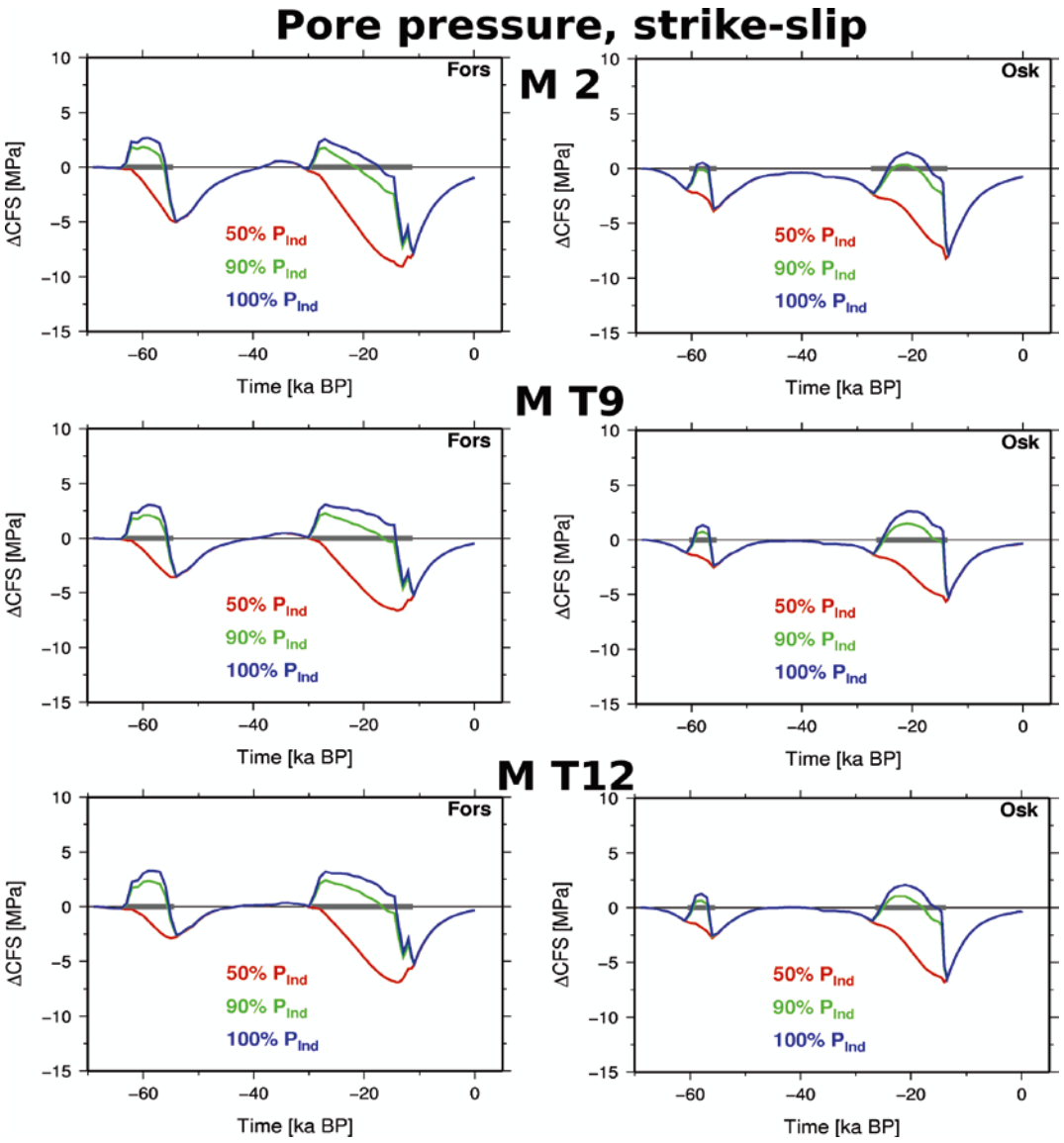

Figure 9-10. *Temporal evolution of the stability field at 9.5 km depth in Forsmark, left, and Oskarshamn, right. Strike-slip background stress field with glacially induced pore pressure head, Pind, of 50% (red lines). Variations in Pind with Pind = 90% (green lines) and Pind = 100% (blue lines). The stress state has SHmax in the direction of plate motion and R = 0.5. Earth models 2, T9 and T12, from top to bottom, respectively. The grey lines at zero indicate the temporal duration of the ice sheet.*

9.4 Temporal evolution of the orientation of the optimally oriented faults

In this section we investigate which faults would be activated by the stress field at different times by calculating the strike and dip of the optimally oriented faults during the evolution of the stress field. In order to investigate which faults in addition to the optimally oriented faults will experience decreased stability we plot stereonets showing the entire stability field at a few critical time periods during the glaciation. For the calculations we use the coefficients of friction defined in Section 8 (0.6 for the synthetic fields, determined from the data for the local fields) and at each time step we use the relationship for the direction of the optimally oriented fault in the principal stress coordinate system shown in Section 8 to calculate strike and dip of the fault in the geographical coordinate system. Here we only use earth model T9 for illustration.

In Figure 9-11 we show the strike directions (red and green) and the dip angles (blue and black) of the two conjugate faults, for Forsmark and Oskarshamn, using the two reference synthetic stress fields (with R = 0.5 and 50% pore pressure head). We see that the blue and black lines always plot on top of each other and are either 30º or 90º, indicating that one principal stress is always close to vertical and that the stress states are consistently reverse or strike-slip, respectively. The uniformity in strike and dip directions shows that the optimally oriented faults are determined by the background stress fields. This is further corroborated by the actual strike values, approximately 152º and 277º for the strike-slip fields (approximately 30º away from the SHmax directions in the SHmax (S1), Shmin (S3) plane as predicted by the value of the coefficient of friction) and 32º and 212º for the reverse fields (90º away from the SHmax directions, dipping 30º in the SHmax (S1), Sv (S3) plane). At this depth we see that the glacially induced stresses mainly act to stabilise or destabilise the faults, they cannot change the direction of the optimally oriented fault significantly, in agreement with /Wu et al. 1999/.

At a repository depth of approximately 500 m the background field stress magnitudes are of the same order of magnitude as the glacially induced stresses and we would expect a larger influence on the directions of the optimally oriented faults. Shown in Figure 9-12 is a plot similar to 9-11, but evaluated at 500 m depth and with the addition of the site specific background stress fields.

For the synthetic strike-slip background field, upper row in Figure 9-12, we see frequent changes in the orientation of the optimally oriented planes. The dip of the faults indicates that we have mostly pure Andersonian strike-slip, normal and reverse faulting regimes and it is interesting to see that although the strike directions show some variability, they seem to be mostly influenced by the background stress field. Concentrating on the time periods when we have less stable faults in Forsmark, the dark red lines just above zero in Figure 9-12, we see that at the beginning of the stadials we have 60º dipping faults striking ESE-WNW, indicating normal faulting. At the end of the stadials, on the contrary, we predict reverse faulting, 30º dipping faults, striking approximately NNE-SSW. This is similar in both Forsmark and Oskarshamn.

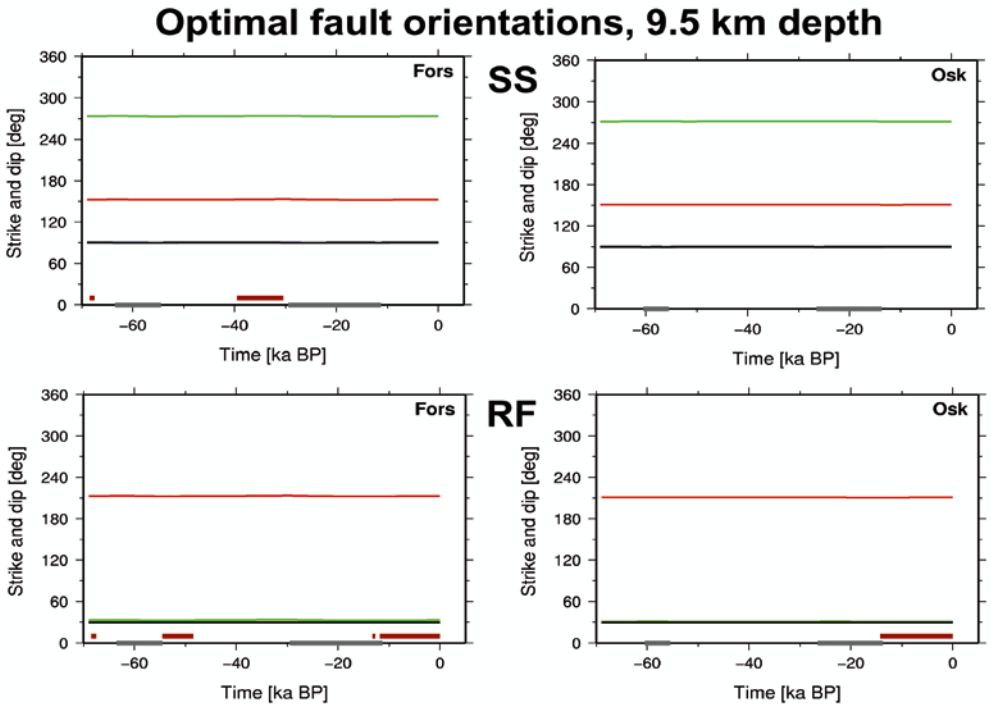

Figure 9-11. *Temporal evolution of the orientation of faults optimally oriented for failure in the stress field at 9.5 km depth in Forsmark, left, and Oskarshamn, right, using the T9 model. Top: synthetic strike-slip background stress field. Bottom: synthetic reverse background stress field. Red and green lines show the strike of the two conjugate faults, blue and black lines (which plot on top of each other) show the dip. The dark red lines just above zero indicate the times when the faults are unstable. The grey lines at zero indicate the temporal duration of the ice sheet.*

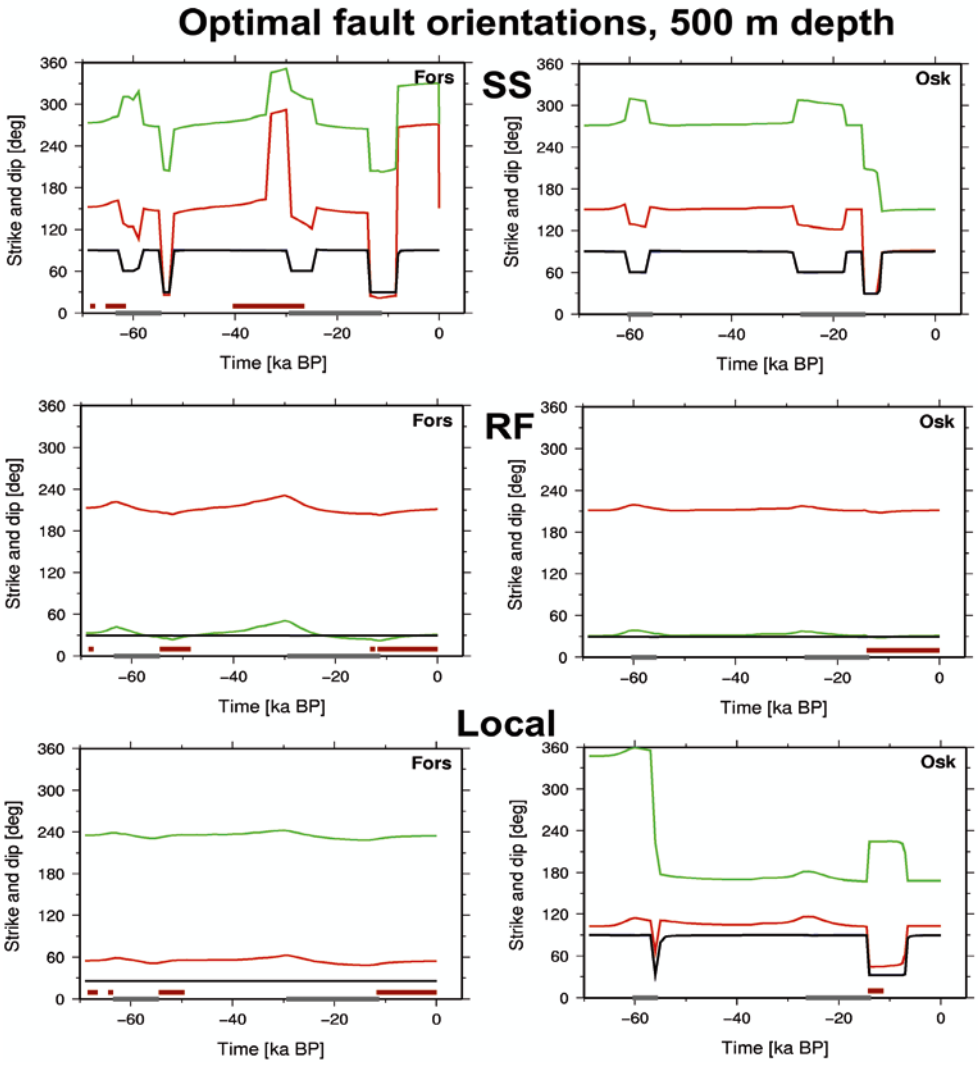

Figure 9-12. *Temporal evolution of the orientation of faults optimally oriented for failure in the stress field at 500 m depth in Forsmark, left, and Oskarshamn, right, using the T9 model. Top: synthetic strike-slip background stress field. Middle: Synthetic reverse background stress field. Bottom: site specific background stress field, reverse in Forsmark and strike-slip in Oskarshamn. Red and green lines show the strike of the two conjugate faults, blue and black lines (which plot on top of each other) show the dip. The dark red lines just above zero indicate the times when the faults are unstable. The grey lines at zero indicate the temporal duration of the ice sheet.*

If the background stress field is our synthetic reverse field, middle row in Figure, 9-12, we see that the inferred fault orientations are consistently reverse faulting, albeit with some variation in the general NNE-SSW strike direction. The lesser variability in fault orientations in the reverse background field probably depends on the relatively larger stress magnitudes of this field. Again, the orientations are in general agreement with the expected optimally oriented fault direction for the synthetic reverse background field.

The last row in Figure 9-12 shows the expected failure planes for the local stress fields in Forsmark and Oskarshamn. In Forsmark we have stable reverse faulting on 30º dipping, NE-SW striking planes. The red stability lines in Figure 9-12 indicate that the most unstable periods are at the end of the stadials, indicating that if shallow faults slip in the Forsmark area they should be NE-SW striking reverse faults. In Oskarshamn, the local strike-slip stress field predicts mostly stable conditions except at the end of the last stadial. Interestingly, Figure 9-12 shows that during the end of glaciation reverse faults are activated also in Oskarshamn, striking NNE-SSW. The 180º rotation of the “green” fault strike direction at approximately 55 kyr BP is due to a small change in the dip direction of the vertical fault, pushing the dip past 90º. This can also be observed in the Forsmark plot in the upper row at approximately 35 kyr BP.

Figures 9-11 and 9-12 show the orientations of the two conjugate optimally oriented faults. But how are faults with slightly different orientations affected? Will the combined stress fields cause instability on a large number of fault orientations? In order to investigate that we plot the stability of faults of all orientations at the most critical time periods for each background stress field and site. We show the stability fields at 9.5 km depth for the two synthetic background stress fields with R = 0.5 and 50% pore pressure head, using earth model T9, in Figure 9-13. The time period is specified in the figure for each stress state and site and is selected as the most unstable time in the temporal evolutions in Figures 9-7 to 9-10. We have added the orientations of a selection of observed fault zones from Forsmark and Oskarshamn (Munier, personal communication, 2009) /Stephens et al. 2008, Wahlgren et al. 2008/ to the figure so that the effects at the sites can be evaluated.

Figure 9-13 shows, as expected, that the regions of instability are rather small at 9.5 km depth and agree with the directions of optimally oriented faults in the background stress fields. Recall that the background fields were constructed in frictional equilibrium on pre-existing faults, i.e. without the additional glacial stresses, the plots in Figure 9-13 would show small white dots at the location of the optimally oriented faults and then just blue. We note that in Forsmark one of the regions of instability in the reverse stress state coincides with a family of observed fracture zones, but remember that the stability is evaluated at 9.5 km depth and the fractures are mapped near the surface.

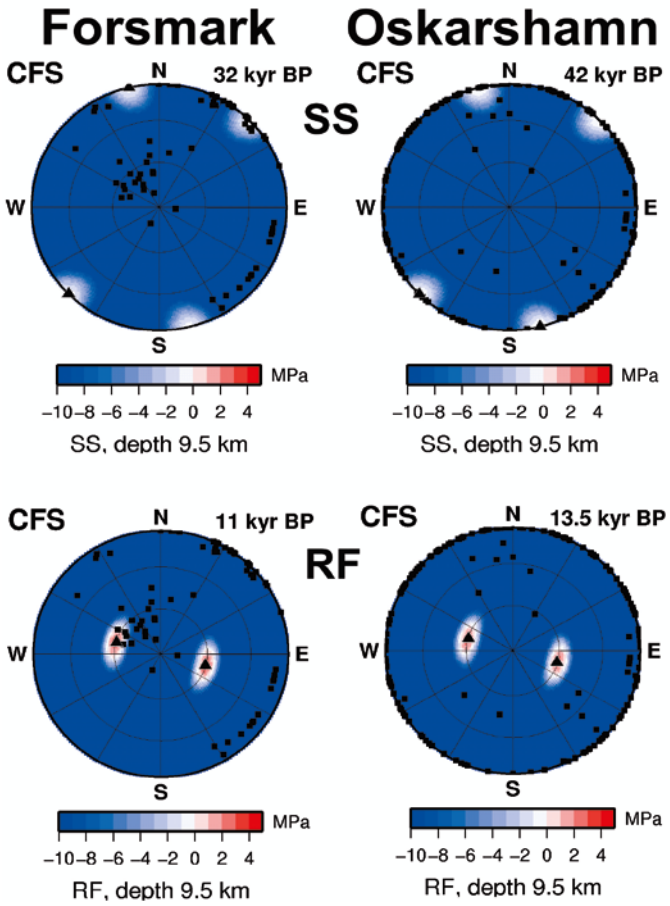

Figure 9-13. *Stereonets showing the stability of faults of all orientations at 9.5 km depth and at four different times corresponding to the times of maximum instability. Blue is stable, red unstable. Left column: Forsmark, right: Oskarshamn. Upper: synthetic strike-slip background stress field. Lower: synthetic reverse background stress field. Black triangles show the optimally oriented faults. Black squares are select fracture zones from the two sites (see references in the text).*

In Figure 9-14 we show similar plots, now at 500 m depth and with the addition of the local background stress fields. We see that at 500 m depth the glacially induced stresses are much more significant and produce relatively large regions of fault instability. In the synthetic strike-slip background field Forsmark at 32 kyr BP is subject to instability on a large range of strike direction for near-vertical faults, encompassing a number of mapped fracture zones. In Oskarshamn the strike-slip field does not produce any instability, as we noted above. In the reverse background field both Forsmark and Oskarshamn have large regions of unstable conditions centred on the optimally oriented faults.

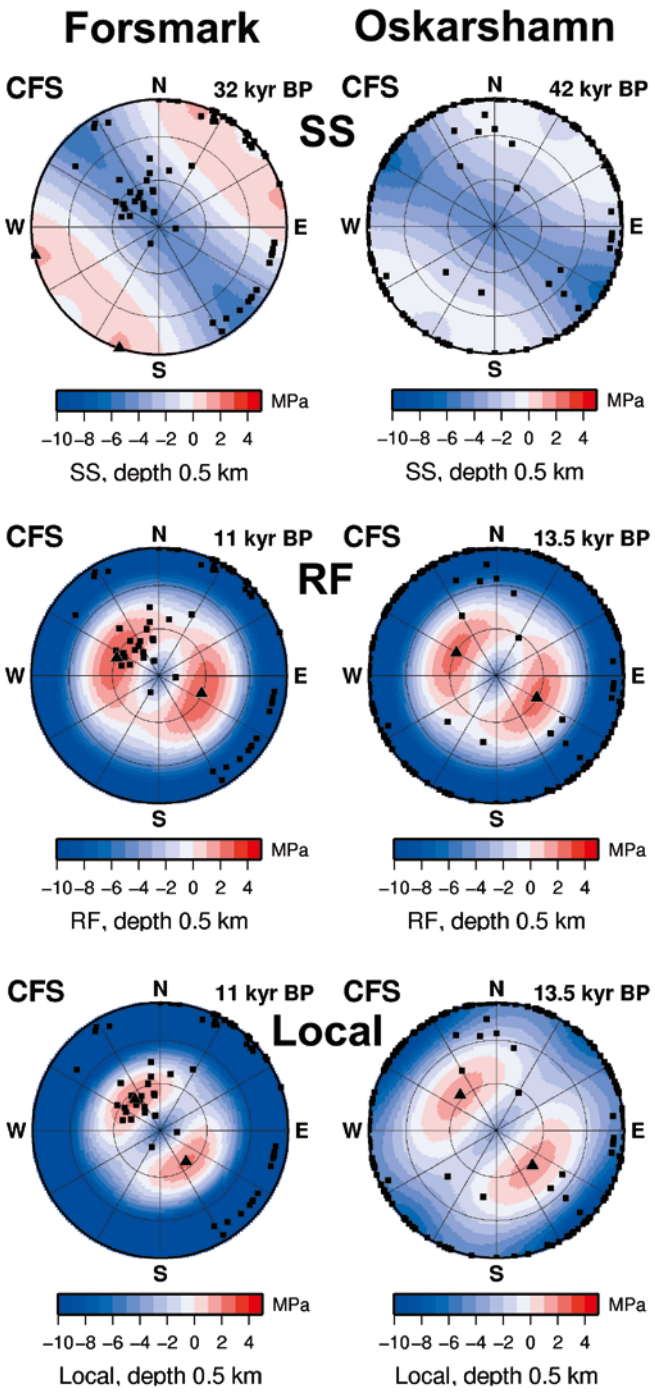

Figure 9-14. *Stereonets showing the stability of faults of all orientations at 500 m depth and at four different times corresponding to the times of maximum instability. Blue is stable, red unstable. Left column: Forsmark, right: Oskarshamn. Upper: synthetic strike-slip background stress field. Middle: synthetic reverse background stress field. Lower: Site specific background stress field. Black triangles show the optimally oriented faults. Black squares are select fracture zones from the two sites (see references in the text).*

Again, in Forsmark one of these regions agrees with a cluster of mapped fractures. In Oskarshamn this is not the case. Note that the two plots are at different times during the late deglaciation. The last row in Figure 9-14 shows the instability effects in the site specific stress fields. In Forsmark we see that the region of instability now agrees very well with the mapped gently dipping fractures, which may indicate that these have formed in the current background stress field, although not necessarily in conjunction with the last glaciation. In Oskarshamn we see clearly, as we noted above, that the local background field has been so affected by the glacial stresses that the stress state at 13.5 kyr BP has changed from strike-slip to reverse. Recall from Section 8 that the local Oskarshamn field has Sv and Shmin that only differ by 1.5 MPa. The stability plot looks similar to the Forsmark plot, although the strike of the optimally oriented faults is 10º different, reflecting the background stresses. In Oskarshamn instability is wide spread over fault orientations at this time, but as most of the mapped fractures are subvertical the effect is less severe than in Forsmark.

When we discuss instability at 500 m depth we do not imply that these potentially unstable fault conditions will cause earthquakes. Earthquakes generally nucleate below 2 km depth (there are notable exceptions, see /Bödvarsson et al. 2006/) so it is unlikely that unstable faults at 500 m depth would evolve into earthquakes. The instability analysis is nevertheless valuable as it shows which fault orientations at 500 m may be more vulnerable to slip, given other external factors such as high pore pressures during a glaciation or secondary motion due to nearby earthquakes.

9.5 Temporal evolution of the stability field on the central Pärvie fault

We now turn to examine the evolution of the fault stability field in a location where we know that a large endglacial earthquake did in fact occur, at the Pärvie fault. We noted in Section 7.3 that the induced glacial stresses at Pärvie are lower in magnitude than those at e.g. Forsmark. How will this affect the stability analysis? We studied all three earth models, but just as above they produce very similar results, so for brevity we only include the results of for the T9 model.

In Figure 9-15 we show how the stability field evolves in model T9 for our reverse (left) and strike-slip (right) synthetic background fields and variations of them. We see that for a reverse background stress field we predict onset of faulting as the ice sheet melts, both at approximately 42 kyr BP and at the end of the glaciation, the latter in agreement with the rupture of the Pärvie fault. Although not shown here, models 2 and T12 also predict the onset of instability at Pärvie right at the end of glaciation in the reverse background field. As we noted above, changes in the direction of the reverse stress field does not influence the result very much, whereas increased pressure heads do produce more unstable conditions. We see that the magnitude of CFS is slightly lower for Pärvie than it is for Forsmark, but not considerably so. The strike-slip background field does not produce instability at all in the reference state. Figure 9-15 shows that the stability varies with variations in the direction of SHmax, but does not produce unstable conditions. Not even an increased pore pressure head creates instability at Pärvie, except in the very beginning of the first stadial. Much of this is most likely an artefact due to our choice of starting point in the modelling time and may be different if prior ice history is included. As mentioned above, additional pore pressure head is an important parameter. At 9.5 km depth however, our model of static, immediate full pressure increase on the faults is probably incorrect as it takes considerable time for the pressure pulse to diffuse down to that depth. In addition, we may have remnant high pore pressures at depth if a wet based ice sheet full of water melts more rapidly than the pore pressure can diffuse out of the rock. Such a scenario would considerably decrease fault stability during deglaciation.

Comparing the temporal stability evolution at Pärvie with that at Forsmark and Oskarshamn we see that there are no fundamental differences in the results. For similar background stress fields and pore pressures the analysis predicts similar results, i.e. instability at the end of the glaciation if the background field is in a reverse state. The fact that large endglacial faulting is not observed at Forsmark and Oskarshamn indicates that either the background stress is different there compared to Pärvie, or that our models do not capture some important aspect of the stress evolution.

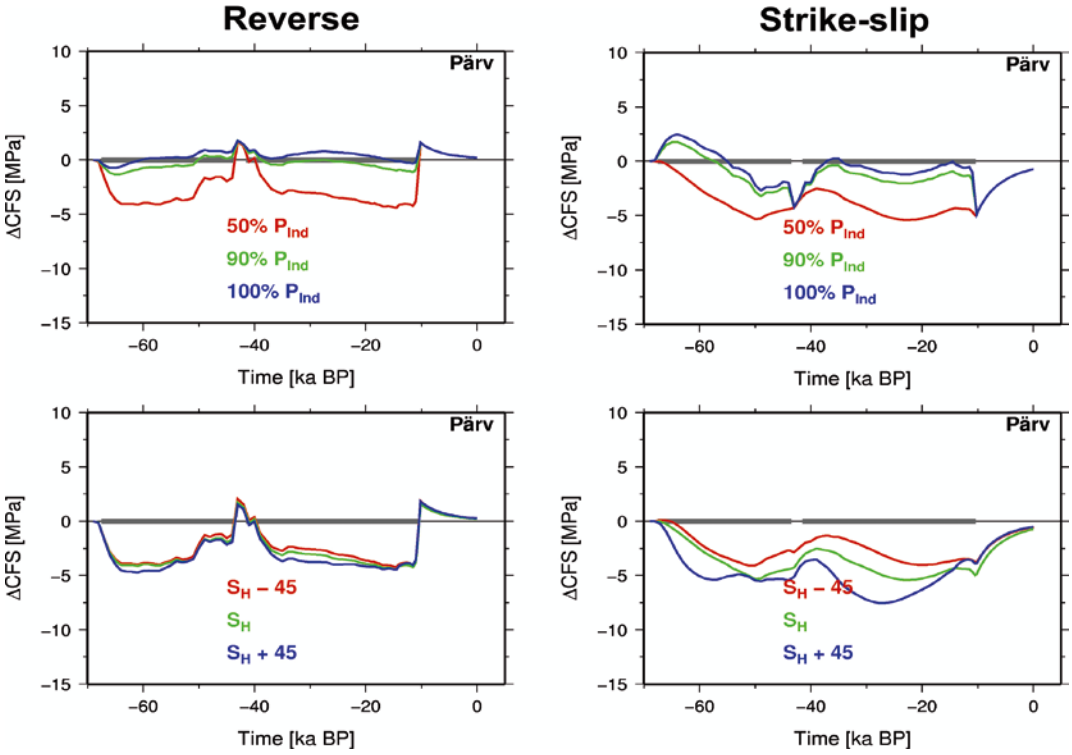

Figure 9-15. *Temporal evolution of the stability field at 9.5 km depth on the central Pärvie fault using earth model T9. Reverse (left) and strike-slip (right) background stress fields. Top: Variation in glacially induced pore pressure head of 50% (red lines), 90% (green lines) and 100% (blue lines). Bottom: Variation in the orientation in the direction of SHmax, ±45 degrees from the plate direction of motion. The grey lines at zero indicate the temporal duration of the ice sheet.*

In Figure 9-16 we show the predicted fault orientations for the stress fields at Pärvie and we see that they are very close to constant in reverse and strike-slip, as expected. We see that the optimal reverse faults are inferred to strike approximately N40°E and N220°E, the former in agreement with the strike of the Pärvie fault. We do not show stability plots such as 9-13 for the Pärvie fault as they are very similar to the 9-13 plots, albeit with a five degree rotation toward south as the plate motion direction at the central Pärvie fault is N128E.

9.6 Summary

We summarize the findings of this section briefly in two tables below, one focusing on effects at Forsmark, Oskarshamn and Pärvie and one showing common results and significant differences in stability for different features that we have used in the modelling in this section.

Finally, we note that no major endglacial faults have been found in the Forsmark or Oskarshamn areas /Lagerbäck et al. 2005, 2006/. Our synthetic strike-slip stress field is consistent with stress observations in south-central Sweden and we note that for glacially induced pore pressures on the order of 50% of the weight of the ice sheet, our GIA models and the synthetic strike-slip field does not predict glacially induced faulting in Oskarshamn and only a period of very low magnitude CFS in Forsmark prior to the latest stadial. At Pärvie our models similarly do not predict unstable faults using the synthetic strike-slip field, but with the reverse field we find fault instability at the end of the stadials. The background stress field could be the key to understanding why the large endglacial faults only occurred in northern Fennoscandia.

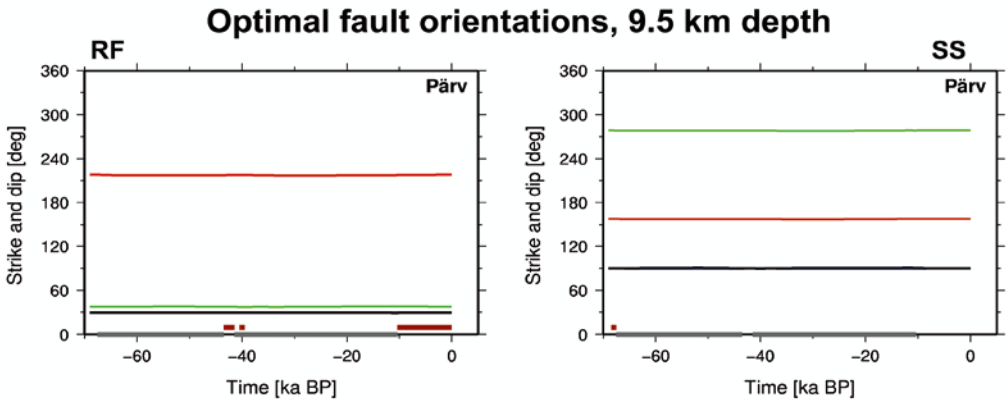

Figure 9-16. *Temporal evolution of the orientation of faults optimally oriented for failure in the stress field at 9.5 km depth on the central Pärvie fault, using the T9 model. Left: reverse background stress field. Right: Strike-slip background stress field. Red and green lines show the strike of the two conjugate optimally oriented faults, blue and black lines show the dip (they plot on top of each other). The grey lines at zero indicate the temporal duration of the ice sheet.*

Table 9-1. Summary of site specific results. SS is a strike-slip stress state, RF is a reverse stress state.

Feature	Common result	Forsmark	Oskarshamn	Pärvie
Synthetic strike-slip background stress (SS)	High stability at the end of stadials.	Produces some instability before the onset of the last stadial, at ~32 kyr BP	No instability unless the induced pore pressures are very high.	No instability even with high induced pore pressures.
Synthetic reverse background stress (RF)	Instability at the end of stadials.	Instability at the end of both stadials, ~55 kyr BP and 11 kyr BP.	Instability at the end of the glaciation, ~ 13 kyr BP.	Instability at the end of the stadials, ~43 kyr BP and ~10 kyr BP.
Site specific stress fields at 500 m depth	Stability evolution very similar to the corresponding synthetic fields at 500 m.	Similar stability evolution as the RF field. Fault orientations vary.	Similar stability evolution as the SS field. Fault orientations vary.	N/A
Effect on locally mapped fractures at 500 m depth.	Only the RF and local fields produce significant instability.	Both with the RF and local background fields there is a group of fractures in the locus of instability.	Very few mapped fractures in the main instability regions of the RF and local fields.	N/A

Table 9-2. Summary of modelling features. SS is a strike-slip stress state, RF is a reverse stress state.

Feature	Common result	Significant difference
Earth model.	Very similar effects on CFS above 10 km depth.	The CFS magnitudes are larger for model 2 than for T9 and T12.
Glacially induced pore pressure (Pind).	Decreases stability.	In SS high Pind causes instability during much of the stadials, in RF the high Pind has much less effect and causes very little additional instability.
Direction of the background stress field.	Affects the stability evolution but not in a general direction.	In SS the effect of varying the SHmax direction is much larger than in RF. In RF ±45º shifts in SHmax is almost negligible.
Unstable fault orientations.	At 9.5 km depth the optimal fault orientations follow those of the background field and are not significantly affected by the glacial stresses. A very small range of additional fault orientations are destabilized.	At 500 m depth the optimal fault orientations in RF are similar to those for the background field, but in SS the orientations vary significantly with time due to the glacial stresses. Large ranges of additional faults are destabilized.

10 Discussion

The purpose of this study has been twofold, both to investigate the stress field induced by glaciation and how it varies with assumptions on the earth and ice models, and how the stability of faults is affected throughout a glacial cycle. Here we will discuss the results obtained above and compared them to results of other studies.

We have seen in our models that the stress field varies significantly in magnitude depending on the earth model used, and that the models with laterally varying lithosphere thickness also produce a slightly different response pattern. However, the general, large scale pattern of stress distribution is very similar in the areal snapshots, and so are the temporal evolution of the stress fields in the different earth models. We note in Figures 7-17 and 7-18, at 500 m depth, that the relative magnitudes of the individual, induced stresses vary with the Earth model, such that e.g. model T9, with viscosity 10^{21} Pa s, has higher induced horizontal stresses but model T8, with a two layered viscosity structure of 8×10^{20} Pa s and 1×0^{22} Pa s, respectively, has higher induced maximum shear stress. The differences in stress response from models with flat or laterally varying lithosphere thickness is surprisingly small. Model T9, for example, is similar to model T12 in Figures 7-17 and 7-18. The observation that the the pattern of induced stress is relatively similar for all earth models considered agrees with numerous observations (see review in /Whitehouse 2009/) of deformation and rebound velocities indicating that the rebound pattern is determined by the properties of the ice sheet while the magnitude of the response depends on the earth model.

For this reason it is unfortunate that we have not been able to investigate an alternative ice history. The /Lambeck et al. 1998/ ice model is significantly thinner than the /Näslund 2006/ model and it only concerns the deglaciation phase of the Fennoscandian glaciation. /Wu et al. 1999/ plot the stress evolution from 20 kyr BP until present at six locations in Scandinavia using a spherical earth model with PREM elastic parameters, the sea-level equation and the ice sheet of /Lambeck et al. 1998/. From their Figure 8, without tectonic stress, we infer glacially induced maximum stress magnitudes of approximately 30 MPa, slightly higher than those from our PREM-like models. /Lambeck 2005/ presented stresses using an updated ice model /Lambeck and Purcell 2003/ which contains generally more ice than the /Lambeck et al. 1998/ model but which only includes an approximate Middle Weichselian ice history, not taking the Jären or Ålesund interstadials into account. He used a PREM-based global earth model, including the far-field ice sheets, with 80 km elastic lithosphere and an upper mantle of viscosity $4\cdot10^{20}$ MPa. His Figure 7 shows that induced stress magnitudes at Forsmark may reach 40 MPa and remain in place for more than 30 kyr before the onset of deglaciation. In addition, shear stress magnitudes reach 20 MPa. These stresses are higher than our PREM-based model stresses, which is likely to be due to a combination of thinner lithosphere, lower upper mantle viscosity and the longer residence time of the ice sheet.

/Lund 2005b/ used the /Lambeck 2005/ ice model to analyse the stability at Forsmark and Oskarshamn, using two different reverse background stress states and two strike-slip states. He concluded that for a reverse state of stress, Forsmark would experience less stable fault conditions approximately at the time of deglaciation whereas Oskarshamn would have a pulse of instability as early as 20 kyr BP. Using the strike-slip field, Forsmark had increased fault stability all through the glacial cycle, whereas Oskarshamn experienced a large pulse of instability around 50 kyr BP. /Lund 2005b/ interpreted this as due to the forebulge, but could not confirm that since he did not have access to the full ice model. Compared to the analysis in this study, the results for the strike-slip background stress field is significantly different using the /Lambeck 2005/ ice model, confirming that the ice model has a large influence on the results of the analysis. As Lambeck's ice sheet has thickened and when more interstadials are included, it will become more similar to the Näslund ice model. In addition, there are indications that the Näslund ice model may contain too much ice (J-O Näslund, private communication). These two models seem thus to be converging, which is promising for the future and adds further confidence in our usage of the Näslund model.

The /Näslund 2006/ ice sheet simulates the Weichselian glaciation, which was an averaged size Quaternary ice sheet. How would a much larger ice sheet, such as the Saalian, influence our analysis? That question is difficult to answer without actual modelling. A larger ice sheet is not just thicker but has larger areal extent and most likely a longer time span from start to maximum size. We cannot simply scale our load function in the analysis by a factor 1.5 or similar. /Johnston et al. 1998/ showed that there is an optimal size for the ice sheet relative to the thickness of the elastic lithosphere where maximum horizontal stress is induced in the earth model. Large ice sheets, as the Laurentide, therefore induces less horizontal stress than the Weichselian ice sheet. The total vertical stress would of course be larger, but it is not evident how these combined effects would affect the stability field, or how the stability would evolve with time. We note also that no endglacial faults of the magnitude of the Fennoscandian faults have been observed in North America.

We have shown that the pattern of decreased fault stability in terms of onset time and magnitude, does indeed depend on the rheology of the earth model, but not very strongly. Instead factors such as the ice sheet induced pore pressure and the state and direction of background stress field are critical to fault stability. This is in general agreement with /Wu et al. 1999/ who found that lithospheric thickness, mantle rheology and compressibility do not influence the stability field significantly, especially not inside the ice margin. Instead they found that the tectonic stress direction and magnitude, and most importantly the ice load, have large effects on fault stability. Similarly /Kaufmann and Wu 2002, Wang et al. 2008/ found that lateral heterogeneity does not affect onset time or the mode of failure within the former ice sheet region but that it has an effect outside the margin.

Our analysis shows that it is important to consider the full background stress field in the fault stability calculation as the regions and times affected by fault instability change dramatically depending on the background stresses. The orientation of the fault plane optimally oriented for failure is also critically dependent on the background stress field. We saw that at shallow depths in a strike-slip background stress field, the orientation of the optimal fault changed significantly during the glaciation. At larger depths in the earth, where the background stress field is significantly larger than the glacially induced field, the orientation of optimally oriented faults is determined solely by the background stress.

The stability field calculated here indicates whether or not fault stability is increased or decreased, but the actual change of sign of ΔCFS should not be taken as proof of fault failure as it depends on a number of assumptions. As discussed above, frictional equilibrium is frequently observed in the crust, but coefficients of friction and other properties vary. /Wu et al. 1999/ proposed a threshold value of 2 MPa of FSM to infer current day seismicity. Aftershock studies indicate that ΔCFS as low as 0.1 MPa is sufficient to trigger earthquakes /Harris 1998/. We note that our results of the stability analysis on the Pärvie fault indicate that the induced stresses, and stress differences, are not very high and the decrease in stability, although clear, was not of large magnitude. In the shallow analysis at Forsmark and Oskarshamn, conditions at 500 m depth may significantly depart from the assumed failure equilibrium as shallow parts of the subsurface can be significantly heterogeneous. In addition, it is not unlikely that the bulk stiffness at 500 m depth is lower than the 64 GPa we have used for Young's modulus due to significant fracture zone and fracture porosity. A lower Young's modulus will lower the stresses induced in the layer.

The large impact of the glacially induced pore pressure on fault stability is not surprising, but nevertheless not in agreement with observations. Our pore pressure model is very simple, and a more realistic approach of including pore pressure diffusion, preferably in a poroelastic medium, would further our understanding for the temporal evolution of the induced pore pressure distribution. As observations in deep boreholes suggest that the crust has hydrostatic pore pressure conditions down to at least depths of 9 km /Townend and Zoback 2000/, it is probable that high glacial pore pressures would be transmitted down to seismogenic depths during the time of a glaciation. Modelling pore pressure diffusion would also allow the study of poroelastic adjustment after deglaciation. Observations of seismic quiescence below the ice sheets of Greenland and Antarctica triggered early investigations of glacially induced fault stability e.g. /Johnston 1987/. The lack of earthquakes below the ice sheets implies either that subglacial pore pressures rarely reach large fractions of the weight of the ice column, or that high pore pressures prevail under the ice sheets and lubricate the crust so that strain accumulation is released virtually aseismically. This second hypothesis is however not in agreement with the occurrence of the large endglacial earthquakes. Further studies of ice sheet hydrology and subglacial pore pressures are necessary to address this problem and to assess to what extent the subglacial drainage system (such as tunnel formation with associated pressure draw down) can maintain low pressure heads on the bedrock.

In this study we have not included tectonic strain accumulation /Johnston 1987/. Recently /Adams 2005/ concluded that additional stress from lithospheric flexure is, in fact, not necessary to cause a pulse of seismicity at the final stage of a deglaciation. If the ice sheet suppresses strain release in earthquakes, the strain accumulation due to the plate motion will suffice to cause very large earthquakes. This line of reasoning should be further pursued, both in its own right and for an analysis of the likelihood of repeat earthquakes. Our models with a reverse background field indicate that we have fault instability at the end of both stadials. As the glacial stresses act mostly as triggers in this analysis, i.e. the earthquake rupture is driven by the tectonic stresses, then once an earthquake has occurred the tectonic stress accumulation determines the recurrence time of that earthquake. If the stress accumulation is slow, as in cratonic Fennoscandia, it may therefore be impossible to generate a second earthquake at the end of the second stadial. Depending on the rate of stress accumulation, large earthquakes recurrence times may even be on the order of entire glacial cycles.

This study cannot conclusively determine whether or not endglacial faulting will occur (or rather, should have occurred) in Forsmark or Oskarshamn. We have investigated a number of factors related to endglacial faulting and conclude that: if the background stress field in Forsmark and Oskarshamn is strike-slip at seismogenic depth /Slunga 1991, Lund and Zoback 1999/, if we have estimated the direction of background SHmax correctly and if the subglacial pore pressure heads are 50% or lower, then glacially induced faulting is unlikely. However, further study is needed to reach more solid conclusions. Such studies include a better understanding of the existing faults, determining their orientation at depth, the prevailing stress field in the area and the influence of pre-existing structures of weakness. In addition, information on the stress field at seismogenic depth is lacking in Forsmark and Oskarshamn, subglacial pore pressures need to be better constrained and perhaps additional mechanisms of failure need be considered.

11 Conclusions

In this study we have examined how a glacial cycle affects the state of stress in the Earth, and how those changes in stress influence the stability of faults. We modelled the glacially induced stress field using a three-dimensional, flat regional finite element model loaded by the ice sheet from the dynamic reconstruction of /Näslund 2006/. A range of earth models were used in the study in order to determine the influence of Earth structure on the results. The response of the models in terms of relative sea-levels were compared to sea-level data from the Baltic /Whitehouse 2007/ and current day vertical and horizontal velocities were compared to GPS data from the Bifrost project /Lidberg et al. 2007/. We find that:

- The response of our earth models can be tuned to fit the GPS data well. The results are sensitive to variations in mantle viscosity, in agreement with previous studies. Features common for all earth models in the difference between data and model prediction are interpreted as resulting from the ice model. The flat layered models tend to fit the data better than the models with laterally varying lithosphere thickness, especially in the horizontal velocities. We also find a fairly good fit to the sea-level data from three sites in the Baltic, in spite of the fact that we do not incorporate the sea-level equation in our modelling.
- The regional pattern of glacially induced stress distribution and horizontal stress directions at 2.5 km depth are remarkably similar for all earth models. The magnitude of the induced stresses vary significantly with the assumed stiffness of the uppermost layer of the models, less with mantle viscosity or lithospheric thickness variation. Stress depth profiles show that the stress distribution at depth is very model dependent and that material boundaries are important as stress tends to concentrate there. The similarity of first order stress patterns show that these depend on the ice history.
- The temporal patterns of glacially induced stress at 500 m depth in Forsmark and Oskarshamn are determined to first order by the ice history whereas the magnitude of the induced stress depend on the earth models. The stiffness of the upper layer affects the magnitudes significantly, but the viscosity of the mantle is also significant when comparing stress magnitudes at a particular time in the stress evolution. Higher stiffness produces higher stress magnitudes while higher viscosity tends to produce lower stress magnitudes. Our models with realistic stiffness distribution which best fit the GPS and sea-level observations have horizontal stress magnitudes similar to the vertical stress. These simulations indicate that induced compressive horizontal stresses at Forsmark do not exceed 40 MPa while the horizontal stresses at Oskarshamn do not exceed 30 MPa. Tensional stresses of up to 5 MPa are expected at both sites as the ice front is advancing or retreating from/to the north.
- The background stress field is of utmost importance when assessing the effect of the the glacially induced stresses on the stability of faults. The background stress state determines which faults are most affected by stability changes and how that effect is manifest in terms of increased or decreased stability. The orientation of the background stress field is important for the strike of the affected faults but also for the stability, especially in a strike-slip background stress field.
- In a reverse background stress field fault stability is promoted under and outside the ice sheet. After deglaciation, faults in the central areas under the former ice sheet show increased instability. In a strike-slip background field, stability is promoted under the ice sheet but unstable areas develop outside the ice edge. After deglaciation, the area under the former ice sheet remains generally stable, while areas of instability exist at the former ice edge. These results hold at 9.5 km depth for all tested earth models, although the magnitude of instability is higher for a model with high upper layer stiffness.
- At 9.5 km depth, the models show fault instability in both Forsmark and Oskarshamn at the end of deglaciation in a reverse background stress field, irrespective of the exact direction of the horizontal stresses. In strike-slip the result varies more with the direction of the background field, but in our reference field both Forsmark and Oskarshamn are mostly stable during the entire glacial cycle. There is a period of low magnitude instability at Forsmark before the onset of the last stadial, at approximately 32 kyr BP.

- At 500 m depth the temporal evolution of the stability fields are similar to the 9.5 km results. Generally, at 9.5 km depth the direction of the faults optimally oriented for failure follow those determined by the background stress field, with a rather small range, but at 500 m depth the range increases significantly.
- The excess pore pressure produced by the ice sheet has a significant effect on fault stability. In this study we have assumed a static pressure head which develops instantaneously at the investigated depths. The results described above have included a pressure head of 50% of the local weight of the ice sheet. Increasing this to 90% or 100% causes instability at earlier times in a reverse background field and in a strike-slip field instability will develop during much of the stadials. The pore pressure effect needs further study with time dependent modelling and preferably more field data.
- Modelling at 9.5 km depth at the Pärvie endglacial fault shows that glacially induced stresses are lower there than at Forsmark or Oskarshamn. The stability analysis shows that unstable conditions are predicted at the end of stadials in a reverse background stress field but that in a strike-slip field the area remains stable. The direction of the optimally oriented fault at instability in the reverse background field agrees with the observed direction of the Pärvie fault.

References

ABAQUS, 2007. ABAQUS manuals, version 6.7, ABAQUS, Inc. [Online]. Available at: http://www.simulia.com.

Adams J, 2005. On the probable rate of magnitude ≥6 earthquakes close to a Swedish site during a glacial cycle. In: Hora S, Jensen M (eds). Expert panel elicitation of seismicity following glaciation in Sweden. SSI rapport 2005:20, Statens strålskyddsinstitut, pp 33–59.

Amelung F, Wolf D, 1994. Viscoelastic perturbations of the Earth: significance of the incremental gravitational force in models of glacial isostacy. Geophysical Journal International, 117, pp 864–879.

Árnadóttir, T, Lund B, Jiang W, Geirsson H, Björnsson H, Einarsson P, Sigurdsson T, 2009. Glacial rebound and plate spreading: results from the first countrywide GPS observations in Iceland. Geophysical Journal International, 177, pp 691–716.

Artemieva I M, Thybo H, 2008. Deep Norden: highlights of the lithospheric structure of Northern Europe, Iceland, and Greenland. Episodes, 31, pp 98–106.

Bard E, Hamelin B, Fairbanks R G, Zindler A, 2000. Calibration of the ^{14}C timescale over the past 30,000 years using mass spectrometric U–Th ages from Barbados corals. Nature, 345, pp 405–410.

Boulton G S, Zatsepin S, Maillot B, 2001. Analysis of groundwater flow beneath ice sheets. SKB TR-01-06, Svensk Kärnbränslehantering AB.

Brace W F, Kohlstedt D L, 1980. Limits on lithospheric stress imposed by laboratory experiments. Journal of Geophysical Research, 85, pp 6248–6252.

Byerlee J D, 1978. Friction of rocks. Pure and Applied Geophysics, 116, pp 615–626.

Bängtsson E, Lund B, 2008. A comparison between two solution techniques to solve the equations of glacially induced deformation of an elastic Earth. International Journal for Numerical Methods in Engineering, 75, pp 479–502.

Böðvarsson R, Lund B, Roberts R, Slunga R, 2006. Earthquake activity in Sweden. Study in connection with a proposed nuclear waste repository in Forsmark or Oskarshamn. SKB R-06-67, Svensk Kärnbränslehantering AB.

Colmenares LB, Zoback M D, 2002. A statistical evaluation of intact rock failure criteria constrained by polyaxial test data for five different rocks. International Journal of Rock Mechanics and Mining Sciences, 39, pp 695–729.

Dziewonski A M, Anderson D L, 1981. Preliminary reference Earth model. Physics of the Earth and Planetary Interiors, 25, pp 297–356.

Ekman M, 1991. Gravity change, geoid change and remaining postglacial uplift of Fennoscandia. Terra Nova, 3, pp 390–392.

Fairbanks R G, 1989. A 17,000-year glacio-eustatic sea level record: influence of glacial melting rates on the Younger Dryas event and deep-ocean circulation. Nature, 342, pp 637–642.

Gephart J W, Forsyth D W, 1984. An improved method for determining the regional stress tensor using earthquake focal mechanism data: application to the San Fernando earthquake sequence. Journal of Geophysical Research, 89, pp 9305–9320.

Glamheden R, Fredriksson A, Röshoff K, Karlsson J, Hakami H, Christiansson R, 2007. Rock mechanics Forsmark. Site descriptive modelling Forsmark stage 2.2. SKB R-07-31, Svensk Kärnbränslehantering AB.

Hakami E, Fredriksson A, Lanaro F, Wrafter J, 2008. Rock mechanics Laxemar. Site descriptive modelling SDM-Site Laxemar. SKB R-08-57, Svensk Kärnbränslehantering AB.

Han D, Wahr J, 1995. The viscoelastic relaxation of a realistically stratified Earth, and a further analysis of postglacial rebound. Geophysical Journal International, 120, pp 287–311.

Harris R A, 1998. Introduction to special section: Stress triggers, stress shadows, and implications for seismic hazard. Journal of Geophysical Research, 103, pp 24347–24358.

Heidbach O, Tingay M, Barth A, Reinecker J, Kurfeß D, Müller B, 2008. The World Stress Map database release 2008. [Online]. Available at: http:// www.world-stress-map.org.

Hetzel R, Hampel A, 2005. Slip rate variations on normal faults during glacial-interglacial changes in surface loads. Nature, 435, pp 81–84.

Ivins E R, James T S, Klemann V, 2003. Glacial isostatic stress shadowing by the Antarctic ice sheet. Journal of Geophysical Research, 108, p 2560.

Jaeger J C, Cook N W G, 1979. Fundamentals of rock mechanics. 3rd ed. London: Chapman and Hall.

James T S, Bent A L, 1994. A comparison of eastern North American seismic strain rates to glacial rebound strain-rates. Geophysical Research Letters, 21, pp 2127–2130.

Jansson P, Näslund J O, Rodhe L, 2006. Ice sheet hydrology – a review. SKB TR-06-34, Svensk Kärnbränslehantering AB.

Johnston A C, 1987. Suppression of earthquakes by large continental ice sheets. Nature, 330, pp 467–469.

Johnston A C, 1989. The effect of large ice sheets on earthquake genesis. In: Gregersen S, Basham P (eds). Earthquakes at North Atlantic passive margins: neotectonics and postglacial rebound. Boston: Kluwer Academic Publishers, pp. 581–599.

Johnston P, 1993. The effect of spatially non-uniform water loads on prediction of sea-level change. Geophysical Journal International, 114, pp 615–634.

Johnston P, Wu P, Lambeck K, 1998. Dependence of horizontal stress magnitude on load dimension in glacial rebound models. Geophysical Journal International, 132, pp 41–60.

Kamb B, 1987. Glacier surge mechanism based on linked cavity configuration of the basal water conduit system. Journal of Geophysical Research, 92, pp 9083–9100.

Kaufmann G, Wu P, 1998. Lateral asthenospheric viscosity variations and postglacial rebound: a case study for the Barents Sea. Geophysical Research Letters, 25, pp 1963–1966.

Kaufmann G, Wu P, 2002. Glacial isostatic adjustment on a three-dimensional laterally heterogeneous Earth: examples from Fennoscandia and the Barents Sea. In: Mitrovica J X, Vermeersen B L A (eds). Ice sheets, sea level and the dynamic earth. Washington: American Geophysical Union. (AGU Geodynamics Series 29), pp 293–309.

Kaufmann G, Wu P, Li G, 2000. Glacial isostatic adjustment in Fennoscandia for a laterally heterogeneous earth. Geophysical Journal International, 143, pp 262–273.

Kaufmann G, Wu P, Ivins E R, 2005. Lateral viscosity variations beneath Antarctica and their implications on regional rebound motions and seismotectonics. Journal of Geodynamics, 39, pp 165–181.

Kenner S J, Seagall P, 2000. A mechanical model for intraplate earthquakes: application to the new Madrid seismic zone. Science, 289, pp 2329–2332.

Kleman J, Stroeven A P, 1997. Preglacial surface remnants and Quaternary glacial regimes in northwestern Sweden. Geomorphology, 19, pp 35–54.

Klemann V, Martinec Z, Ivins E R, 2008. Glacial isostasy and plate motion. Journal of Geodynamics, 46, pp 95–103.

Klemann V, Wolf D, 1998. Modelling of stresses in the Fennoscandian lithosphere induced by Pleistocene glaciations. Tectonophysics, 294, pp 291–303.

Klemann V, Wolf D, 1999. Implications of a ductile crustal layer for the deformation caused by the Fennoscandian ice sheet. Geophysical Journal International, 139, pp 216–226.

Klemann V, Wu P, Wolf D, 2003. Compressible viscoelasticity: stability of solutions for homogeneous plane earth models. Geophysical Journal International, 153, pp 569–585.

Lagerbäck R, 1979. Neotectonic structures in northern Sweden. Geologiska Föreningens i Stockholm Förhandlingar, 100, pp 263–269.

Lagerbäck R, Sund M, Svantesson S-I, 2006. Searching for late- and postglacial faulting in the Oskarshamn region. Results from 2005. Oskarshamn site investigation. SKB P-06-160, Svensk Kärnbränslehantering AB.

Lagerbäck R, Sund M, Svedlund J-O, Johansson H, 2005. Searching for late- and postglacial faulting in the Forsmark region. Results from 2002–2004. Forsmark site investigation. SKB P-05-51, Svensk Kärnbränslehantering AB.

Lambeck K, 2005. Glacial load stresses: can existing faults or other zones of crustal weakness be reactivated during glacial cycles? In: Hora S, Jensen M (eds). Expert panel elicitation of seismicity following glaciation in Sweden. SSI rapport 2005:20, Statens strålskyddsinstitut, pp 85–106.

Lambeck K, Purcell A, 2003. Glacial rebound and glacial stress in Finland. Posiva 2003-10, Posiva Oy.

Lambeck K, Smither C, Johnston P, 1998. Sea-level change, glacial rebound and mantle viscosity for northern Europe. Geophysical Journal International, 134, pp 102–144.

Latychev L, Mitrovica J X, Tromp J, Tamisiea M E, Komatitsch D, Christara C C, 2005. Glacial isostatic adjustment on 3-D Earth models: a finite volume formulation. Geophysical Journal International, 161, pp 421–444.

Lidberg M, Johansson J M, Scherneck H-G, Davis J L, 2007. An improved and extended GPS-derived 3D velocity field of the glacial isostatic adjustment (GIA) in Fennoscandia. Journal of Geodesy, 81, pp 213–230.

Lokrantz H, Sohlenius G, 2006. Ice marginal fluctuations during the Weichselian glaciation in Fennoscandia, a literature review. SKB TR-06-36, Svensk Kärnbränslehantering AB.

Lund B, 2005a. Effects of deglaciation on the crustal stress field and implications for endglacial faulting: a parametric study of simple Earth and ice models. SKB TR-05-04, Svensk Kärnbränslehantering AB.

Lund B, 2005b. Large earthquakes during a glacial cycle. In: Hora S, Jensen M (eds). Expert panel elicitation of seismicity following glaciation in Sweden. SSI rapport 2005:20, Statens strålskyddsinstitut, pp 107–119.

Lund B, 2006a. Glacially induced faulting. In: Climate and climate-related issues for the safety assessment SR-Can. SKB TR-06-23, Svensk Kärnbränslehantering AB, pp 117–125.

Lund B, 2006b. Stress variations during a glacial cycle at 500 m depth in Forsmark and Oskarshamn: Earth model effects. SKB R-06-95, Svensk Kärnbränslehantering AB.

Lund B, Näslund J-O, 2009. Glacial isostatic adjustment: Implications for glacially induced faulting and nuclear waste repositories. In: Connor C B, Chapman N A, Connor L J (eds). Volcanic and tectonic hazard assessment for nuclear facilities. Cambridge: Cambridge University Press, pp 142–155.

Lund B, Slunga R, 1999. Stress tensor inversion using detailed microearthquake information and stability constraints: application to Ölfus in southwest Iceland. Journal of Geophysical Research, 104, pp 14947–14964.

Lund B, Townend J, 2007. Calculating horizontal stress orientations with full or partial knowledge of the tectonic stress tensor. Geophysical Journal International, 170, pp 1328–1335.

Lund B, Zoback M D, 1999. Orientation and magnitude of in situ stress to 6.5 km depth in the Baltic Shield. International Journal of Rock Mechanics and Mining Sciences and Geomechanics Abstracts, 36, pp 169–190.

Lund B, Zoback M D, 2007. Great intraplate earthquakes and glaciation: effects of rheology and the tectonic state of stress on glacially induced faulting in Scandinavia. Eos Transactions AGU, 88(52), Fall Meeting Supplement, T54C-06.

Lönnqvist M, Hökmark H, 2009. Assessment of potential for glacially induced hydraulic jacking at different depths. SKB R-09-35, Svensk Kärnbränslehantering AB.

Martinec Z, 2000. Spectral-finite element approach to three-dimensional viscoelastic relaxation in a spherical earth. Geophysical Journal International, 142, pp 117–141.

Martinec Z, Wolf D, 2005. Inverting the Fennoscandian relaxation-time spectrum in terms of an axisymmetric viscosity distribution with a lithospheric root. Journal of Geodynamics, 39, pp 143–163.

Milne G A, Mitrovica J X, 1998. Postglacial sea-level change on a rotating Earth. Geophysical Journal International, 133, pp 1–19.

Milne G A, Mitrovica J X, Scherneck H-G, Davis J L, Johansson J M, Koivula H, Vermeer M, 2004. Continuous GPS measurements of postglacial adjustment in Fennoscandia: 2. Modeling results. Journal of Geophysical Research, 109, pp B02412.1–B02412.18.

Mitrovica J X , Davis J L, Shapiro I I, 1994. A spectral formalism for computing three dimensional deformations due to surface loads 2. Present-day glacial isostatic adjustment. Journal of Geophysical Research, 99, pp 7075– 7101.

Mitrovica J X, Milne G A, Davis J L, 2001. Glacial isostatic adjustment on a rotating Earth. Geophysical Journal International, 147, pp 562–578.

Näslund J-O, 2006. Ice sheet dynamics, in Climate and climate related issues for the safety assessment SR-Can. SKB TR-06-23, Svensk Kärnbränslehantering AB.

Näslund J-O, Rodhe L, Fastook J, Holmlund P, 2003. New ways of studying ice sheet flow directions and glacial erosion by computer modelling – examples from Fennoscandia. Quarternary Science Reviews, 22, pp 245–258.

Näslund J O (ed), Wohlfarth B (ed), Alexanderson H, Helmens K, Hättestrand M, Jansson P, Kleman J, Lundqvist J, Brandefelt J, Houmark-Nielsen M, Kjellström E, Strandberg G, Knudsen K L, Krog Larsen N, Ukkonen P, Mangerud J, 2008. Fennoscandian paleo-environment and ice sheet dynamics during Marine Isotope Stage (MIS) 3. Report of a workshop held September 20–21, 2007 in Stockholm, Sweden. SKB R-08-79, Svensk Kärnbränslehantering AB.

O'Keefe K, Wu P, 2002. Effect of mantle structure on postglacial induced horizontal displacement. In: Mitrovica J X, Vermeersen B L A (eds). Ice sheets, sea level and the dynamic earth. Washington: American Geophysical Union. (AGU Geodynamics Series 29), pp 109–118.

Olsson S, Roberts R G, Böðvarsson R, 2007. Analysis of waves converted from S to P in the upper mantle beneath the Baltic Shield. Earth and Planetary Science Letters, 257, pp 37–46.

Pagli C, Sigmundsson F, Lund B, Sturkell E, Geirsson H, Einarsson P, Árnadóttir T, Hreinsdóttir S, 2007. Glacio-isostatic deformation around the Vatnajökull ice cap, Iceland, induced by recent climate warming: GPS observations and finite element modeling. Journal of Geophysical Research, 112, p B08405.

Peltier W R, 1974. The impulse response of a Maxwell Earth. Reviews of Geophysics, 12, pp 649–669.

Peltier W R, 2004. Global glacial isostacy and the surface of the ice-age Earth: The ICE-5G (VM2) Model and GRACE. Annual Review of Earth and Planetary Sciences, 32, pp 111–149.

Peltier W R, Tushingham A M, 1991. Influence of glacial isostatic adjustment on tide gauge measurments of secular sea level change. Journal of Geophysical Research, 96, pp 6779–6796.

Pérez-Gussinyé M, Watts A B, 2005. The long-term strength of Europe and its implications for plate-forming processes. Nature, 436, pp 381–384.

Pérez-Gussinyé M, Lowry A R, Watts A B, Velicogna I, 2004, On the recovery of effective elastic thickness using spectral methods: examples from synthetic data and from the Fennoscandian Shield. Journal of Geophysical Research, 109, pp B10409.1–B10409.20.

Porter S C, 1989. Some geological implications of average quaternary glacial conditions. Quaternary Research 32, pp 245– 261.

Priestley K, McKenzie D, 2006. The thermal structure of the lithosphere from shear wave velocities. Earth and Planetary Science Letters, 244, pp 285–301.

Påsse T, 2004. The amount of glacial erosion of the bedrock. SKB TR-04-25, Svensk Kärnbränslehantering AB.

Quinlan G, 1984. Postglacial rebound and the focal mechanisms of eastern Canadian earthquakes. Canadian Journal of Earth Sciences, 21, pp 1018–1023.

SKB, 2005. Preliminary site description, Forsmark area – version 1.2. SKB R-05-18, Svensk Kärnbränslehantering AB.

SKB, 2006a. Preliminary site description, Laxemar sub-area – version 1.2. SKB R-06-10, Svensk Kärnbränslehantering AB.

SKB, 2006b. Climate and climate related issues for the safety assessment SR-Can. SKB TR-06-23, Svensk Kärnbränslehantering AB.

Sauber J, Plafker G, Molnia B F, Bryant A A, 2000. Crustal deformation associated with glacial fluctuations in the eastern Chugach Mountains, Alaska. Journal of Geophysical Research, 105, pp 8055–8077.

Sauber J, Molnia B F, 2004. Glacier ice mass fluctuations and fault instability in tectonically active southern Alaska. Global and Planetary Change, 42, pp 279–293.

Schotman H H A, Wu P, Vermeersen L L A, 2008. Regional perturbations in a global background model of glacial isostasy. Physics of the Earth and Planetary Interiors, 171, pp 323–335.

Shomali Z H, Roberts R G, the TOR working group, 2002. Non-linear body wave teleseismic tomography along the TOR array. Geophysical Journal International, 148, pp 562–574.

Slunga R, 1991. The Baltic Shield earthquakes. Tectonophysics, 189, pp 323–331.

Spada G, Antonioli A, Cianetti S, Giunchi C, 2006. Glacial isostatic adjustment and relative sea-level changes: the role of lithospheric and upper mantle heterogeneities in a 3-D spherical Earth. Geophysical Journal International, 165, pp 692–702.

Stein S, Sleep N H, Geller R J, Wang S-C, Kroeger G C, 1979. Earthquakes along the passive margin of Eastern Canada. Geophysical Research Letters, 6, pp 537–540.

Steffen H, Kaufmann G, Wu P, 2006. Three-dimensional finite-element modeling of the glacial isostatic adjustment in Fennoscandia. Earth and Planetary Science Letters, 250, pp 358–375.

Steffen H, Wu P, Kaufmann G, 2007. Sensitivity of crustal velocities in Fennoscandia to radial and lateral viscosity variations in the mantle. Earth and Planetary Science Letters, 257, pp 474–485.

Stephens M B, Simeonov A, Isaksson H, 2008. Bedrock geology Forsmark. Modelling stage 2.3. Implications for and verification of the deterministic geological models based on complementary data. SKB R-08-64, Svensk Kärnbränslehantering AB.

Svendsen J I, Alexanderson H, Astakhov V I, Demidov I, Dowdeswell J A, Funder S, Gataullin V, Henriksen M, Hjort C, Houmark-Nielsen, M, Hubberten H W, Ingolfsson O, Jakobsson M, Kjær K H, Larsen E, Lokrantz H, Lunkka J P, Lyså A, Mangerud J, Matiouchkov A, Murray A, Möller P, Niessen F, Nikolskaya O, Polyak L, Saarnisto M, Siegert C, Siegert M J, Spielhagen R F, Stein R, 2004. Late Quaternary ice sheet history of northern Eurasia. Quaternary Science Reviews, 23, pp 1229–1271.

Townend J, Zoback MD, 2000. How faulting keeps the crust strong. Geology, 28, pp 399–402.

Turpeinen H, Hampel A, Karow T, Maniatis G, 2008. Effect of ice growth and melting on the slip evolution of thrust faults. Earth and Planetary Science Letters, 269, pp 230–241.

Wahlgren C-H, Curtis P, Hermanson J, Forssberg O, Öhman J, Fox A, La Pointe P, Drake H, Triumf C-A, Mattsson H, Thunehed H, Juhlin C, 2008. Geology Laxemar. Site descriptive modelling SDM-Site Laxemar. SKB R-08-54, Svensk Kärnbränslehantering AB.

Walcott R I, 1970. Isostatic response to loading of the crust in Canada. Canadian Journal of Earth Sciences, 7, pp 716–727.

Wang H, Wu P, 2006. Effects of lateral variations in lithospheric thickness and mantle viscosity on glacially induced surface motion on a spherical, self-gravitating Maxwell Earth. Earth and Planetary Science Letters, 244, pp 576–589.

Wang H, Wu P, van der Wal W, 2008. Using postglacial sea level, crustal velocities and gravity-rate-of-change to constrain the influence of thermal effects on mantle lateral heterogeneities. Journal of Geodynamics, 46, pp 104–117.

Whitehouse P, 2006. Isostatic adjustment and shoreline migration. In: Climate and climate-related issues for the safety assessment SR-Can. SKB TR-06-23, Svensk Kärnbränslehantering AB, pp 68–92.

Whitehouse P, 2007. A relative sea-level data base for Fennoscandia, Unpublished manuscript and database. Svensk Kärnbränslehantering AB.

Whitehouse P, 2009. Glacial isostatic adjustment. State of the art report. SKB TR-09-11, Svensk Kärnbränslehantering AB.

Whitehouse P, Latychev K, Milne G A, Mitrovica J X, Kendall R, 2006. Impact of 3-D Earth structure on Fennoscandian glacial isostatic adjustment: implications for space-geodetic estimates of present-day crustal deformations. Geophysical Research Letters, 33, L13502.

Wohlfarth B, 2009. Ice free conditions in Fennoscandia during Marine Isotope Stage 3? SKB TR-09-12, Svensk Kärnbränslehantering AB.

Wolf D, 1991. Viscoelastodynamics of a stratified, compressible planet: incremental field equations and short- and long-time asymptotes. Geophysical Journal International, 104, pp 401–417.

Wolf D, 1993. The changing role of the lithosphere in models of glacial isostasy: a historical review. Global and Planetary Change, 8, pp 95–106.

Wu P, 1992. Deformation of an incompressible viscoelastic flat earth with power-law creep: a finite element approach. Geophysical Journal International, 108, pp 35–51.

Wu P, 1997. Effect of viscosity structure on fault potential and stress orientations in eastern Canada, Geophys. J. Int. 130, 365–382.

Wu P, 2004. Using commercial finite element packages for the study of earth deformations, sea levels and the state of stress. Geophysical Journal International, 158, pp 401–408.

Wu P, Hasegawa H S, 1996a. Induced stresses and fault potential in eastern Canada due to a disc load: a preliminary analysis. Geophysical Journal International, 125, pp 415–430.

Wu P, Hasegawa H S, 1996b. Induced stresses and fault potential in eastern Canada due to a realistic load: a preliminary analysis. Geophysical Journal International, 127, pp 215–229.

Wu P, Johnston P, 2000. Can deglaciation trigger earthquakes i N. America? Geophysical Research Letters, 27, pp 1323–1326.

Wu P, Johnston P, Lambeck K, 1999. Postglacial rebound and fault instability in Fennoscandia. Geophysical Journal International, 139, pp 657–670.

Wu P, Peltier W R, 1982. Viscous gravitational relaxation. Geophysical Journal of the Royal Astronomical Society, 70, pp 435–485.

Wu P, van der Wal W, 2003. Postglacial sealevels on a spherical, self-gravitating viscoelastic earth: effects of lateral viscosity variations in the upper mantle on the inference of viscosity contrasts in the lower mantle. Earth and Planetary Science Letters, 211, pp 57–68.

Zoback M D, Healy J H, 1984. Friction, faulting and in situ stress. Annals Geophysicae, 2, pp 689–698.

Zoback M D, Townend J, 2001. Implications of hydrostatic pore pressures and high crustal strength for the deformation of intraplate lithosphere. Tectonophysics, 336, pp 19–30.

ISSN 1404-0344
CM Gruppen AB, Bromma, 2009